

THE HORIZONTAL LOOP EM RESPONSE OF A THIN  
VERTICAL CONDUCTOR IN A CONDUCTIVE HALF-SPACE

A THESIS SUBMITTED IN PARTIAL FULFILLMENT  
OF THE REQUIREMENTS FOR THE DEGREE  
OF DOCTOR OF PHILOSOPHY

DEPARTMENT OF EARTH SCIENCES  
UNIVERSITY OF MANITOBA

by



JAMES EDWARD HANNESON

APRIL 1981

THE HORIZONTAL LOOP EM RESPONSE OF A  
THIN VERTICAL CONDUCTOR IN A  
CONDUCTIVE HALF-SPACE

BY

JAMES E. HANNESON

A thesis submitted to the Faculty of Graduate Studies of  
the University of Manitoba in partial fulfillment of the requirements  
of the degree of

DOCTOR OF PHILOSOPHY

©<sup>v</sup> 1981

Permission has been granted to the LIBRARY OF THE UNIVER-  
SITY OF MANITOBA to lend or sell copies of this thesis, to  
the NATIONAL LIBRARY OF CANADA to microfilm this  
thesis and to lend or sell copies of the film, and UNIVERSITY  
MICROFILMS to publish an abstract of this thesis.

The author reserves other publication rights, and neither the  
thesis nor extensive extracts from it may be printed or other-  
wise reproduced without the author's written permission.

## ABSTRACT

The frequency domain electromagnetic response of a thin vertical tabular plate in a conductive two-layer earth can be obtained by solving the electric field integral equation using the method of point collocation with global test functions. When it is assumed that the components of the scatter current perpendicular to the plate edges vanish at the plate edges, and when test functions are chosen which satisfy this condition, EM responses can usually be obtained for plates ranging from the resistive to the inductive limits. For highly resistive host media, numerical failure occurs when the plate conductivity is high enough that magnetic effects predominate. The solution is valid over a sufficiently wide range of parameters as to permit the computation of horizontal loop (Slingram) profiles over a plate in a layered earth. Suites of horizontal loop Argand diagrams are presented which illustrate the peak (in-phase and quadrature) anomaly values for a plate imbedded in a conductive earth. The suites show anomaly enhancement and phase rotation due to the conductive host and can be used to obtain, from field surveys, estimates of conductor depth and conductivity - thickness which are independent of the prospecting frequency.

## ACKNOWLEDGEMENTS

In the many years since this project began I have incurred more debts than I can readily acknowledge. I must, however, thank my supervisor, Prof. D. H. Hall, for his support, encouragement and patience, and for his assistance in times of particular need. Furthermore, I want to thank Dr. C. D. Anderson for his support during the early stages of this project and Drs. A. Wexler and B. H. MacDonald from whom I learned about variational methods. I also wish to remember the assistance and understanding I received from Dr. W. C. Brisbin. Financial support in the form of several University of Manitoba Graduate Fellowships as well as computing grants were received from the Department of Earth Sciences for which I am grateful.

Although the early development work on the computer program was carried out while I was a full time student at the University of Manitoba, many of the refinements were made in later years when studies continued on a part-time basis. To that end I wish to thank my employer, Gulf Minerals Canada Limited, and in particular Mr. Kenneth A. Morgan, through whose influence computing funds were made available at the University of Saskatchewan at Saskatoon, thereby allowing work to continue during my brief posting in that

city. In recent years I have incurred a debt to Prof. Gordon F. West of the Department of Physics, University of Toronto, which I fear I may never be able to repay. In sharing with me, his considerable understanding of the problem, many of the difficulties and shortcomings associated with other attempted solutions were overcome. All of the production runs and many of the developmental runs were made on the DEC VAX/11 in the Department of Physics and paid for through a geosciences research grant to G. F. West from the Ontario Geological Survey.

I also wish to thank my friend, Dr. P. Chagarlamudi, who, while struggling with his own problems, provided sympathy and understanding particularly during those dark days when my efforts were being made more in hope than in expectation. Finally I owe a debt to my dear wife, Donna, for her constant support and encouragement and for her selfless sacrifice of countless mornings, evenings, weekends and holidays.

Credit for the typing, mathematics and all, goes to Mrs. Beryl Logan (who is not sure she would do it again). The figures were professionally drafted by Mr. Al Lombardi.

For Wyrð oft saveth  
earl undoomed if he doughty be!

Beowulf

## TABLE OF CONTENTS

ABSTRACT .....		i
ACKNOWLEDGEMENTS .....		ii
 Chapter		
I	INTRODUCTION	
	1.1 Motivation .....	1
	1.2 Numerical Model and its Usefulness .....	3
	1.3 The Horizontal Loop System .....	5
	1.4 Current Status of Interpretational Aids ..	5
	1.5 Outline and Objectives .....	8
	1.6 Symbols and Notation .....	9
II	FORMULATION AND GENERAL STRATEGY	
	2.1 Introduction .....	12
	2.2 The Integral Equation .....	12
	2.3 Transformation of the Integral Equation into a Matrix Equation .....	14
	2.4 General Remarks Concerning the Green's Tensor .....	19
III	CALCULATION AND INTEGRATION OF THE PRIMARY PART OF THE GREEN'S TENSOR	
	3.1 Introduction .....	22
	3.2 The Green's Tensor: Point Source .....	23
	3.3 The Green's Tensor: Distributed Source ..	25
	3.4 Generalization of the Theory to Include Lossy Media .....	29
	3.5 Typical Tensor Elements .....	30
	3.6 Integration of the Source Point over the Observation Point .....	31
	3.7 Alternate Handling of Zero Order Polynomial .....	35
IV	CALCULATION AND INTEGRATION OF THE SECONDARY PART OF THE GREEN'S TENSOR	
	4.1 Introduction .....	40
	4.2 A Horizontal Electric Dipole in the Lower Layer of a Two-Layer Earth .....	42
	4.3 A Vertical Electric Dipole in the Lower Layer of a Two-Layer Earth .....	50

Chapter

V	CALCULATION OF INCIDENT FIELDS AND SECONDARY FIELDS PERTINENT TO THE HORIZONTAL LOOP SYSTEM	
5.1	Introduction .....	54
5.2	Vertical Magnetic Dipole Above a Two-Layer Earth .....	55
5.3	Secondary Magnetic Field at the Receiver Location due to Eddy Currents on the Plate .....	59
VI	A DESCRIPTION OF THE ALGORITHM	
6.1	Introduction .....	61
6.2	Application of the Point Collocation Method .....	62
6.3	Test Functions .....	64
6.4	Integration of Terms Involving $G^P$ Over Regions Containing a Match Point $\sim$ .....	69
6.5	Integration of Terms Involving $G^P$ Over Remote Regions $\sim$ .....	72
6.6	Hankel Transforms and the Spatial Integration of Terms Involving $G^S$ .....	72
6.7	Construction of the Matrix .....	74
6.8	Calculation of the Secondary Field at the Surface .....	75
VII	NUMERICAL RESULTS	
7.1	Introduction .....	77
7.2	The Effect of Host Conductivity on Peak Anomaly Values .....	81
7.3	The Conductive Overburden Effect .....	
7.4	Finiteness of the Host Resistivity .....	101
7.5	Convergence of the Solution .....	135
7.6	Finiteness of the Plate Size .....	138
7.7	Two Case Histories .....	142
7.8	Comparison with Other Studies .....	146
VIII	CONCLUDING REMARKS	
8.1	Previous Attempts .....	153
8.2	Suggestions for Future Work .....	155
8.3	Summary and Conclusions .....	157
	REFERENCES .....	160
Appendices		
A	Electric Field at the Centre of a Spherical Volume of Constant Current .....	164



B	Hertz Potential for a Horizontal Electric Dipole in a Two-Layer Earth .....	168
C	Hertz Potential for a Vertical Electric Dipole in a Two-Layer Earth .....	176
D	Least Squares Matrix for a Vector Operator Equation .....	179

## LIST OF FIGURES

Figure		
1-1	Thin Tabular Conductor in a Two-Layer Earth ...	6
2-1	The Matrix Equation: Equation 2.10 .....	18
2-2	Diagrammatic Ray Path Interpretation of Energy Propagating from Transmitter to Receiver .....	20
3-1	Cylindrical Region of Current Centred About the Singular Point .....	36
4-1	Horizontal Electric Dipole in a Two-Layer Earth.	43
4-2	Vertical Electric Dipole in a Two-Layer Earth ..	51
5-1	Vertical Magnetic Dipole Above a Two-Layer Earth .....	56
6-1	Match Points and the Subdivision of the Plate into Patches .....	63
6-2	Test Functions	
	a. y-variation of the y-component .....	67
	b. z-variation of the y-component .....	67
	c. y-variation of the z-component .....	67
	d. z-variation of the z-component .....	67
6-3	Subdivision of One Quadrant of a Singular Patch for Integration $G^{PyOzO}$ .....	70
6-4	Subdivision of One Quadrant of a Singular Patch for Integration of $G^{Py^nz^m}$ .....	71
7-1	Transmitter and Receiver Locations for the Reciprocity Test .....	80
7-2	Typical Horizontal Loop Profile Across a Vertical Conductor in a Conductive Host .....	82
7-3	Horizontal Loop Profile for a Thin Plate in a Conductive Half Space .....	83
7-4	Plate Current for Peak Anomaly Value .....	85
7-5	Horizontal Loop Response of a Homogeneous Half-Space .....	87
7-6	Horizontal Loop Response of a Large Vertical Plate in a Non-Conducting Host $\alpha_H=0$ .....	88

Figure

7-7	Horizontal Loop Response of a Large Vertical Plate in a Homogeneous Half-Space	
	a. $\alpha_H=0.125$ .....	89
	b. $\alpha_H=0.25$ .....	90
	c. $\alpha_H=0.5$ .....	91
	d. $\alpha_H=1.$ .....	92
	e. $\alpha_H=2.$ .....	93
	f. $\alpha_H=4.$ .....	94
	g. $\alpha_H=8.$ .....	95
	h. $\alpha_H=16.$ .....	96
	i. $\alpha_H=32.$ .....	97
7-8a	The Effect of Increasing Host Conductivity; $D=.2L$ .....	99
7-8b	The Effect of Increasing Overburden Frequency; $D=.2L$ .....	100
7-9	The Effect of Increasing Overburden Conductivity; $D=.2L$ .....	103
7-10	Horizontal Loop Response of a Two-Layer Earth; $\alpha_L/\alpha_H=.16$ .....	104
7-11	Horizontal Loop Response of a Thin Vertical Plate in a Two-Layer Earth; $\alpha_L/\alpha_H=.16$	
	a. $\alpha_H=0.125$ .....	105
	b. $\alpha_H=0.25$ .....	106
	c. $\alpha_H=0.5$ .....	107
	d. $\alpha_H=1.$ .....	108
	e. $\alpha_H=2.$ .....	109
	f. $\alpha_H=4.$ .....	110
7-12	Horizontal Loop Response of a Two-Layer Earth; $\alpha_L/\alpha_H=.5$ .....	112
7-13	Horizontal Loop Response of a Thin Vertical Plate in a Two-Layer Earth; $\alpha_L/\alpha_H=.5$	
	a. $\alpha_H=0.125$ .....	113
	b. $\alpha_H=0.25$ .....	114
	c. $\alpha_H=0.5$ .....	115
	d. $\alpha_H=1.$ .....	116
	e. $\alpha_H=2.$ .....	117
	f. $\alpha_H=4.$ .....	118
7-14	Horizontal Loop Response of a Two-Layer Earth; $\alpha_L/\alpha_H=1.6$ .....	119
7-15	Horizontal Loop Response of a Thin Vertical Plate in a Two-Layer Earth; $\alpha_L/\alpha_H=1.6$	
	a. $\alpha_H=0.125$ .....	120
	b. $\alpha_H=0.25$ .....	121
	c. $\alpha_H=0.5$ .....	122

Figure

	d. $\alpha_H=1.$ .....	123
	e. $\alpha_H=2.$ .....	124
	f. $\alpha_H=4.$ .....	125
7-16	Horizontal Loop Response of a Two-Layer Earth; $\alpha_L/\alpha_H=5.$ .....	126
7-17	Horizontal Loop Response of a Thin Vertical Plate in a Two-Layer Earth $\alpha_L/\alpha_H=5.$	
	a. $\alpha_H=0.125$ .....	127
	b. $\alpha_H=0.25$ .....	128
	c. $\alpha_H=0.5$ .....	129
	d. $\alpha_H=1.$ .....	130
	e. $\alpha_H=2.$ .....	131
7-18	Evidence for Numerical Breakdown at High Conductivity Contrasts .....	134
7-19	Modulus of Peak Anomaly Values for Plates of Different Size .....	141
7-20	Conductive Overburden: A Case History .....	145
7-21	Current Densities on Plates of Varying Conductivity Irradiated by a Vertical Magnetic Dipole	
	a. $\sigma_3=.01$ .....	149
	b. $\sigma_3=.1$ .....	149
	c. $\sigma_3=1.$ .....	150
	d. $\sigma_3=10.$ .....	150
	e. $\sigma_3=100.$ .....	151
	f. $\sigma_3=1000.$ .....	151

## LIST OF TABLES

Table

7-1a	Peak Anomaly Values for the Free Space Host Compared with Conductive Half Space Host .....	133
7-1b	Reciprocity Error Estimates for Corresponding Peak Anomaly Values of Table 1a .....	133
7-2a	Peak Anomaly Values for Increasing Numbers of Test Functions in the Solution: .....	137
7-2b	Reciprocity Error Estimates in Percent for Increasing Numbers of Test Functions in the Solution .....	137
7-3a	Peak Anomaly Values for Plates of Differing Size .....	140
7-3b	Reciprocity Error Estimates for Peak Anomaly Values in Table 7-3a .....	140
7-4	Estimated Background (L=150m) and the Computed Response for Earth Parameters $\sigma_1=.068$ , $\sigma_2=.0096$ L=2m and Layer Thickness=.05L .....	144
7-5	Field Observations Compared with the Calculated Response for $\sigma_3t=62$ and $\sigma t=31$ .....	144
7-6	Maximum Amplitude of the In-Phase or Quadrature Component of the Current Comparing Results with those of Lajoie (1973) .....	152

## CHAPTER I

### INTRODUCTION

#### 1.1 Motivation

There can be little doubt that the use of electromagnetic (EM) phenomena for the detection of metallic ore occurrences beneath the surface of the earth has been an unqualified success. From their inception, electromagnetic methods have been designed to exploit the extreme conductivity contrast which often exists between concentrations of metallic minerals and the host rocks in which they occur. By inducing currents to flow in the conductor and by measuring the effects of these currents at the surface of the earth, the presence of a conductor can be inferred. Parameters governing the conductor's shape, depth, orientation and conductivity can often be diagnosed through comparison of field data with theoretical calculations and/or analogue scale model observations. Much of the early success of EM induction methods was contingent upon choosing operating frequencies low enough to make insignificant the effect of the more poorly conductive host rock on the currents induced in the conductor. However, the simplifications gained through lowering the frequency reach a natural limit when the conductor

itself fails to produce a recognizable response. In contrasting the geophysical and the electrical engineering approach to EM scattering, Annan(1974) points out that in geophysics measurements are usually made over distances much less than a free space wavelength, and that the scattering bodies are conductors with finite conductivity, usually embedded in a conductive host. Electrical engineers are concerned largely with scattering by perfect conductors in free space and methods devised to deal with such problems may not be readily applicable to the more general geophysical problem.

It is well known to field geophysicists and theoreticians alike that the conductivity of the host medium can have a profound effect on the strength of an anomaly and must, whenever possible, be taken into account. Lajoie (1973) reports that Turam anomalies generated by deep plates can sometimes be enhanced five-fold and more, by electric current channelled from the host into the conductor. This is an effect which occurs in addition to the magnetically induced secondary current vortex which, in a non-conducting host, is the sole component of the secondary current. Provided the host effects can be understood, this anomaly enhancement could conceivably be used to improve the depth penetrating capabilities of a given prospecting system, through the use of elevated frequencies. A natural upper limit on frequencies occurs when fields travelling to and from the conductor are seriously attenuated by the lossy host, or when geological 'noise' (anomalies which geophysicists cannot understand) reaches unacceptable levels.

Through continuing exploration, the number of undrilled EM responders decreases, and areas more difficult to interpret, such as the Abitibi clay belt of Ontario or the lateritic soils common in Western Australia, require more attention. In these areas it may not be possible to eliminate the response of the host without eliminating the response of the target conductor itself. If EM methods are to work in such cases, the only alternative may be to study the host and the target as an electromagnetically coupled system.

### 1.2 The Numerical Model and its Usefulness

Many ore bodies occur as thin, vein-like features having one linear dimension which is much less than the other two. Such bodies can have any orientation and can have boundaries so irregular as to tax the imagination of a geologist. Calculating the response of a real orebody is a hopeless task. Nevertheless, considerable progress in interpretation techniques can be made with a model as simple as a rectangular thin plate. In most cases only the upper horizontal edge of the plate bears any resemblance to reality because many ore bodies either outcrop at a more or less horizontal surface or subcrop beneath overburden or beneath unconformable rocks of a younger age.

When attempts are made to drill the conductor it is important to know the depth to the apex and the dip of the planar feature. Such diagnostic parameters for a very large scatterer can be obtained from the study of tabular plates with a decidedly finite size, provided the ends lie outside the region where



the induced eddy currents are significant. The size of the plate required to simulate a half-plane depends upon the nature of the source and measuring system. But this is not to say that the rectangular plate model cannot be used to study end effects generated by a conductor which is terminated, say, by a steeply dipping fault. Also of importance is the use of a rectangular plate to study the effect of limited depth extent.

Notwithstanding the geological usefulness of a rectangular model, powerful incentive for its use in numerical modeling comes in the form of reduced programming difficulties. Considerably more simplification is gained when the plate is kept vertical, although this restriction is accepted grudgingly and only temporarily.

The geology of the host material can be as variable as the conductor itself. Nevertheless, useful results can be obtained by assuming the host rock to have constant conductivity, bounded above by a horizontal plane interface beyond which lies the non-conducting air. The added complication of an intermediate layer of different conductivity is worth the additional programming effort since it allows the simulation of a common geological situation -- conductive overburden.

The problem tackled in this work, therefore, is to compute the EM response of a thin vertical tabular conductor imbedded in the lower layer of a conductive two-layer earth. The conductivities are to cover a range that will include the conductivities of naturally occurring geological material, and the operating frequency is to be compatible, at least through

a scaling transformation (Sinclair, 1948) with frequencies used in the field.

The coordinate system, with physical properties and linear dimensions of the various regions is portrayed in Figure 1-1. The regions are specified only by their conductivities; other electromagnetic parameters (permittivity and permeability) are assigned free space values.

### 1.3 Horizontal Loop System

Also illustrated in Figure 1-1 are the transmitter and receiver coils of the horizontal loop prospecting system. The transmitting coil generates an audio frequency signal, the relative strength and phase of which is measured by the receiver. In the field, operators carry the loops in tandem along the traverse line, taking readings at specified locations. Anomalous values arise when conductivity inhomogeneities intervene to alter the electromagnetic coupling of the loops.

Once a method is devised for obtaining the secondary currents on the plate due to arbitrary excitation, the response can be particularized for any of the several airborne or ground prospecting systems used by industry. For this work the horizontal loop system was chosen, largely because of its popularity and familiarity and because of a generally recognized need for a fuller understanding of how readings in the field are affected by a conductive host.

### 1.4 Current Status of Interpretational Aids

The large amount of horizontal loop surveying done in

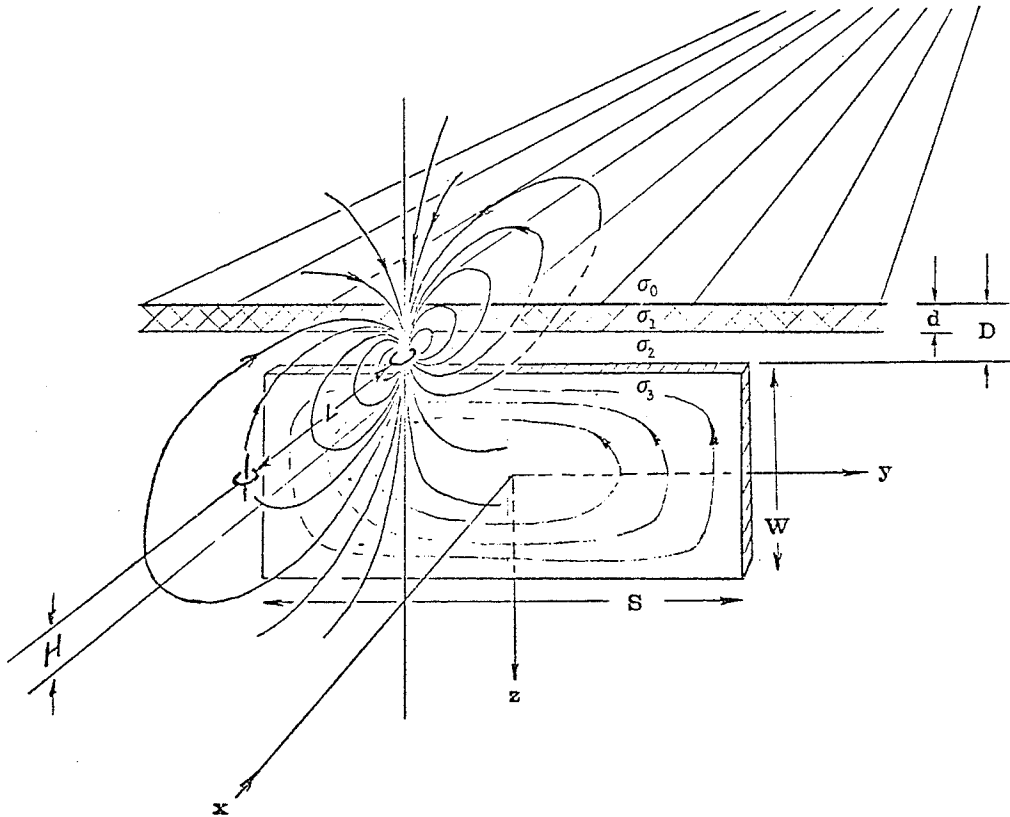


Figure 1-1 Thin Tabular Conductor in a Two-Layer Earth

recent decades has yielded a vast but not always accessible body of case history responses. Private company archives and published field data (Strangway, 1967; Betz, 1974; Ketola, 1968) coupled with analogue model responses of a conductor in free space (West, 1960; Strangway, 1967; Ketola and Puranen, 1967; Nair et al., 1968) has led to considerable understanding of horizontal loop responses. However, estimates of depth, dip and conductivity-thickness are based on responses of a plate in free space and do not include the effect of the conductive host. Accurate numerical models for the EM response of a plate in free space have been constructed by Lamontagne and West (1971) and by Annan (1974) and while considerable understanding of scatter current flow patterns was gained, interpretation procedures could not be greatly improved over those methods already established through analogue scale model studies.

Horizontal loop responses of typical host media (two-layer earth) have been computed by Eadie (1979; ref. Frieschnecht, 1967) while Villegas-Garcia (1979), using analogue scale models, has measured and catalogued responses for valleys and troughs at the bottom of a conductive overburden layer.

While Lajoie and West (1976) have obtained, numerically, the Turam response of a thin vertical conductor in a conductive host (over a complete range of conductivity contrasts) and Hohmann (1975) has computed some EM effects for small scatterers of low conductivity contrast, no systematic study of the horizontal loop response of a plate in a conductive host has yet been made. Although the initial effects of increasing host

conductivity have been demonstrated experimentally by Gupta Sarma and Maru (1971) and C. P. Gupta (1973), the inability to continuously vary the conductivities of the media has permitted only a qualitative understanding of host effects.

### 1.5 Thesis Objectives and Outline

When the interpretation of survey data is based upon numerical or analogue model responses of conductors in a non-conducting host, depth and conductivity-thickness estimates invariably depend upon the operating frequency. Geophysicists have long agreed that one of the causes of this recurring source of annoyance is the inability of free space models to simulate the effect of current flowing from the host rock into the conductor. It is the objective of this thesis to resolve some of these ambiguities, and for cases where the objective is not fully met, it is hoped that some knowledge of the physical processes which give rise to anomalous readings in the field can be gained.

In Chapter II, the problem is formulated in terms of an integral equation, and the numerical method used to solve it is described. The single-minded approach to the problem suffers from not first establishing a broader theoretical foundation for both the formulation and the subsequent numerical work. On the other hand, the heart of the problem and the strategy used in solving it are immediately exposed. Chapter III deals with the primary part of the Green's tensor in the integral equation and the problem of integrating over the singularity, while

Chapter IV deals with the secondary part and the semi-infinite integrals which arise in the presence of planar interfaces. Chapter V discusses the calculation of the incident electric field on the plate radiated by the vertical magnetic dipole transmitter and also describes the calculation of the vertical component of the magnetic field at the receiver location radiated by the secondary eddy currents in the plate. Chapter VI describes the algorithm used to obtain an approximate solution to the integral equation, while Chapter VII presents several sets of results and touches on the question of the accuracy of the results and their applicability to practical exploration problems. The final chapter discusses possible ways to improve the solution and gives suggestions for future work and alternative approaches to the problem.

### 1.6 Symbols and Notation

Vector quantities are denoted by an underlined symbol, such as  $\underline{r}$ , and a unit vector is designated with a circumflex, like  $\hat{i}$ . An effort is made to define all symbols where they first appear in the text, but a list of the most common ones appears below. The rationalized MKS system is used throughout.

- $\underline{r}$  position vector, usually denoting a point where a field quantity is being observed or measured.
- $\underline{r}_s$  position vector designating the location of an EM source and frequently appearing as an integration variable.
- $dV_s$  volume element indicating integration with respect to the  $\underline{r}_s$  variable.

$\hat{i}$   $\hat{j}$   $\hat{k}$  unit vectors in the x,y, and z directions.  
 $\hat{u}$  a unit outward normal.

$\vec{E}(\vec{r})$  electric field intensity at  $\vec{r}$

$\vec{D}(\vec{r})$  electric displacement field

$\vec{B}(\vec{r})$  magnetic flux density

$\vec{H}(\vec{r})$  magnetic field intensity

$\vec{J}(\vec{r})$  electric current density

$E_x$  x-component of a vector  $\vec{E}$ .

$\sigma_n$  conductivity of medium n

$\mu$  permeability of free space

$\epsilon$  permittivity of free space

$\omega$  angular frequency

$\kappa_n$  admittivity of medium n ( $=\sigma_n+i\epsilon\omega$ )

$\gamma_n$  propagation constant for medium n ( $=[i\omega\mu\kappa_n]^{1/2}$ )

$\vec{A}(\vec{r})$  magnetic vector potential

$\phi(\vec{r})$  electric scalar potential

$\pi(\vec{r})$  electric Hertz potential

$\pi^*(\vec{r})$  magnetic Hertz potential

$\vec{G}(\vec{r}|\vec{r}_s)$  Green's tensor for the electric field at  $\vec{r}$  due to an electric dipole of unit strength at  $\vec{r}_s$ .

$\vec{G}_{HJ}(\vec{r}|\vec{r}_s)$  Green's tensor for the magnetic field at  $\vec{r}$  due to an electric dipole of unit strength at  $\vec{r}_s$ .

$G_{xy}(\vec{r}|\vec{r}_s)$  Green's function for the x-component of the electric field due to a y-oriented electric dipole. An element of  $\vec{G}(\vec{r}|\vec{r}_s)$ .

$G_{\approx}^P(\underline{r}|\underline{r}_S)$  primary part of  $G_{\approx}(\underline{r}|\underline{r}_S)$   
 $G_{\approx}^S(\underline{r}|\underline{r}_S)$  secondary part of  $G_{\approx}(\underline{r}|\underline{r}_S)$ .  
 $G^P$  or  $G^S$  an unspecified element of  $G_{\approx}^P(\underline{r}|\underline{r}_S)$  or  $G_{\approx}^S(\underline{r}|\underline{r}_S)$   
 respectively.

S strike length of plate  
 W width (depth extent) of plate  
 t thickness of plate  
 L coil separation for transmitter-receiver array  
 D plate depth below surface  
 d layer thickness  
 H coil height above surface  
  
 $\sigma_p$  plate response parameter ( $=\mu\omega_0 tL$ )  
 $\sigma_L$  layer response parameter ( $=\mu\omega_0 dL$ )  
 $\sigma_H$  host response parameter ( $=\mu\omega_0 L^2$ )



## CHAPTER II

### FORMULATION AND GENERAL STRATEGY

#### 2.1 Introduction

We are concerned with the electric field in a conductive inhomogeneity in a conductive host. Hohmann (1970, pp. 1-10) gives a rigorous development of coupled integral equations which are satisfied by the electric and magnetic fields. In a conductive scatterer having no permittivity or permeability contrast with the host medium, these equations reduce to a single integral equation for the electric field. As the electric field integral equation is not in question, it is justified in this section using a heuristic argument followed by a description of the strategy whereby an approximate solution can be obtained.

#### 2.2 The Integral Equation

To determine the total electric field in a scatterer of conductivity  $\sigma_3$  in a host medium of conductivity  $\sigma_2$  we begin by writing the field as the sum of an incident and a scattered part:

$$\underline{\underline{E}} = \underline{\underline{E}}^i + \underline{\underline{E}}^s \quad \text{Eq.2.1}$$

The known incident field  $\underline{\underline{E}}^i$  is that which would exist if there were no scatterer, and the scatter field  $\underline{\underline{E}}^s$  is that arising from the scatter currents  $\underline{\underline{J}}^s$ . Scatter currents are currents which flow in excess of currents motivated by the incident field passing through the host; that is, they flow in excess of  $\sigma_2 \underline{\underline{E}}^i$ .

The scatter field at  $\underline{\underline{r}}$  is written conveniently in terms of the Green's tensor  $\underline{\underline{G}}(\underline{\underline{r}}|\underline{\underline{r}}_s)$  and the unknown scatter current  $\underline{\underline{J}}^s$  at the source point  $\underline{\underline{r}}_s$ , using

$$\underline{\underline{E}}^s(\underline{\underline{r}}) = \int_V \underline{\underline{G}}(\underline{\underline{r}}|\underline{\underline{r}}_s) \underline{\underline{J}}^s(\underline{\underline{r}}_s) dV_s \quad \text{Eq.2.2}$$

where  $V$  includes all regions where  $\underline{\underline{J}}^s$  is non-zero and integration is over the subscripted variable  $\underline{\underline{r}}_s$ . The tensor can be written more explicitly as a matrix of Green's functions

$$\underline{\underline{G}}(\underline{\underline{r}}|\underline{\underline{r}}_s) = \begin{bmatrix} G_{xx}(\underline{\underline{r}}|\underline{\underline{r}}_s) & G_{xy}(\underline{\underline{r}}|\underline{\underline{r}}_s) & G_{xz}(\underline{\underline{r}}|\underline{\underline{r}}_s) \\ G_{yx}(\underline{\underline{r}}|\underline{\underline{r}}_s) & G_{yy}(\underline{\underline{r}}|\underline{\underline{r}}_s) & G_{yz}(\underline{\underline{r}}|\underline{\underline{r}}_s) \\ G_{zx}(\underline{\underline{r}}|\underline{\underline{r}}_s) & G_{zy}(\underline{\underline{r}}|\underline{\underline{r}}_s) & G_{zz}(\underline{\underline{r}}|\underline{\underline{r}}_s) \end{bmatrix} \quad \text{Eq.2.3}$$

where a typical element  $G_{xy}(\underline{\underline{r}}|\underline{\underline{r}}_s)$  is the x-component of the electric field at  $\underline{\underline{r}}$  due to a y-oriented electric dipole of unit dipole moment at  $\underline{\underline{r}}_s$ . Calculations of the matrix elements will be the subject of later sections.

We have treated  $\underline{\underline{J}}^s$ , for the moment, as an impressed current in developing an expression for  $\underline{\underline{E}}^s(\underline{\underline{r}})$ . Eq.2.1 is now

$$\underline{\underline{E}}(\underline{\underline{r}}) = \underline{\underline{E}}^i(\underline{\underline{r}}) + \int_V \underline{\underline{G}}(\underline{\underline{r}}|\underline{\underline{r}}_s) \underline{\underline{J}}^s(\underline{\underline{r}}_s) dV_s \quad \text{Eq.2.4}$$

But the scatter current, in view of an earlier definition, can be written in terms of the total field through

$$\tilde{J}^S(\tilde{r}_S) = (\sigma_3 - \sigma_2) \tilde{E}(\tilde{r}_S) \quad \text{Eq. 2.5}$$

Equation 2.5 in Equation 2.2 now yields, assuming  $\sigma_3$  is constant,

$$\tilde{E}(\tilde{r}) = \tilde{E}^i(\tilde{r}) + (\sigma_3 - \sigma_2) \int_V \tilde{G}(\tilde{r}|\tilde{r}_S) \tilde{E}(\tilde{r}_S) dV_S \quad \text{Eq. 2.6}$$

which, since  $\tilde{E}(\tilde{r})$  is unknown, is an integral equation for the total field in the scatterer.

### 2.3 Transformation of the Integral Equation into a Matrix Equation (Point Collocation Method)

The general strategy for solving Equation 2.6 involves the use of a linear combination of known functions to approximate each vector component of the solution. The unknown function coefficients are determined by insisting that Equation 2.6 be true at a sufficient number of points in the scatterer as to generate a sufficient number of simultaneous linear equations which can be solved for the coefficients using standard matrix procedures. This method is used extensively in numerical analysis and is referred to as Point Collocation (Harrington, 1968).

Practical limitations on the proposed method occur in that many functions may be required to accurately model the complex current flow in a three-dimensional inhomogeneity. To reduce the problem to manageable proportions, we will restrict our attention to planar bodies sufficiently thin as to permit ignoring any scattered current flowing perpendicular to the large surfaces, and any variation in the intensity of the longitudinal components over the thickness of the sheet. This

reduces the dimensionality of the solution vector field from three to two. If the body is oriented perpendicular to one of the Cartesian axes, say the x-axis, this has the effect of reducing the Green's tensor of Equation 2.3 to a 2x2 matrix decreasing the amount of integration necessary to transform Equation 2.6 into a matrix equation.

To demonstrate this transformation, we begin by writing Equation 2.6 in vector notation subject to these simplifying assumptions.

$$\begin{bmatrix} E_Y(\underline{r}) \\ E_Z(\underline{r}) \end{bmatrix} = \begin{bmatrix} E_Y^i(\underline{r}) \\ E_Z^i(\underline{r}) \end{bmatrix} + (\sigma_3 - \sigma_2) \int \begin{bmatrix} G_{YY}(\underline{r}|\underline{r}_s) & G_{ZY}(\underline{r}|\underline{r}_s) \\ G_{ZY}(\underline{r}|\underline{r}_s) & G_{ZZ}(\underline{r}|\underline{r}_s) \end{bmatrix} \begin{bmatrix} E_Y(\underline{r}_s) \\ E_Z(\underline{r}_s) \end{bmatrix} dV_s$$

Eq.2.7

We now assume that both vector components of the solution can be described by a linear combination of known functions  $f_i(y,z)$  called test functions. The test functions may be members of a mathematical set of functions (such as  $y^n z^m$  where  $n$  and  $m$  have integer values), or they may themselves be linear combinations of a more fundamental set. Choosing the first three members of this set, we write

$$\underline{E}_Y(\underline{r}) = \sum_{i=1}^3 a_i f_i(y,z) \hat{j}$$

$$\underline{E}_Z(\underline{r}) = \sum_{i=1}^3 b_i f_i(y,z) \hat{k}$$

Eqs.2.8

where  $\hat{j}$  and  $\hat{k}$  are the unit vectors in the y- and z- directions, and the  $a_i$  and  $b_i$  ( $i=1,2,3$ ) are the unknown test function coefficients. Substituting Equations 2.8 into Equation 2.7 yields

$$\begin{bmatrix} \sum_{i=1}^3 a_i f_i(\underline{r}) \\ \sum_{i=1}^3 b_i f_i(\underline{r}) \end{bmatrix} = \begin{bmatrix} E_Y^i(\underline{r}) \\ E_Z^i(\underline{r}) \end{bmatrix} +$$

$$(\sigma_3 - \sigma_2) \int \begin{bmatrix} G_{YY}(\underline{r}|\underline{r}_s) & G_{YZ}(\underline{r}|\underline{r}_s) \\ G_{ZY}(\underline{r}|\underline{r}_s) & G_{ZZ}(\underline{r}|\underline{r}_s) \end{bmatrix} \begin{bmatrix} \sum_{i=1}^3 a_i f_i(\underline{r}_s) \\ \sum_{i=1}^3 b_i f_i(\underline{r}_s) \end{bmatrix} dV_s \quad \text{Eq. 2.9}$$

where  $\underline{r} = y \hat{j} + z \hat{k}$

and  $\underline{r}_s = y_s \hat{j} + z_s \hat{k}$

Insisting that Equation 2.9 be true at three different points in the scatterer  $(y_1, z_1)$ ,  $(y_2, z_2)$ ,  $(y_3, z_3)$ , known as match points, yields the required conditions for determining the coefficients of the test functions. At the three points these conditions are

$$\begin{bmatrix} \sum_{i=1}^3 a_i f_i^1 \\ \sum_{i=1}^3 b_i f_i^1 \end{bmatrix} = \begin{bmatrix} E_Y^i(\underline{r}_1) \\ E_Z^i(\underline{r}_1) \end{bmatrix} + \int \begin{bmatrix} G_{YY}^{1S} & G_{YZ}^{1S} \\ G_{ZY}^{1S} & G_{ZZ}^{1S} \end{bmatrix} \begin{bmatrix} \sum_{i=1}^3 a_i f_i^S \\ \sum_{i=1}^3 b_i f_i^S \end{bmatrix} dV_s$$

$$\begin{bmatrix} \sum_{i=1}^3 a_i f_i^2 \\ \sum_{i=1}^3 b_i f_i^2 \end{bmatrix} = \begin{bmatrix} E_Y^i(\underline{r}_2) \\ E_Z^i(\underline{r}_2) \end{bmatrix} + \int \begin{bmatrix} G_{YY}^{2S} & G_{YZ}^{2S} \\ G_{ZY}^{2S} & G_{ZZ}^{2S} \end{bmatrix} \begin{bmatrix} \sum_{i=1}^3 a_i f_i^S \\ \sum_{i=1}^3 b_i f_i^S \end{bmatrix} dV_s$$

and

$$\begin{bmatrix} \sum_{i=1}^3 a_i f_i^3 \\ \sum_{i=1}^3 b_i f_i^3 \end{bmatrix} = \begin{bmatrix} E_Y^i(\underline{r}_3) \\ E_Z^i(\underline{r}_3) \end{bmatrix} + \int \begin{bmatrix} G_{YY}^{3S} & G_{YZ}^{3S} \\ G_{ZY}^{3S} & G_{ZZ}^{3S} \end{bmatrix} \begin{bmatrix} \sum_{i=1}^3 a_i f_i^S \\ \sum_{i=1}^3 b_i f_i^S \end{bmatrix} dV_S$$

where notation  $G_{YY}^{3S} = (\sigma_3 - \sigma_2) G_{YY}(\underline{r}_3 | \underline{r}_S)$ ,

$$f_i^2 = f_i(y_2, z_2) \text{ and } f_i^S = f_i(y_S, z_S)$$

has been employed. Expanding the matrix multiplications and summations, and equating independently the y- and z-components of each of these vector equations yields six equations which can be solved simultaneously for the six unknown test function coefficients. Some rearrangement of terms leads to the matrix equation Equation 2.10, illustrated in Figure 2-1. When the electric field inside the scatterer is obtained, the scatter currents are also known (via Equation 2.5) and Equation 2.4 can then be used to evaluate the total electric field at any point outside the body.

Alternatively we can use a formula similar to Equation 2.6 (Hohmann, 1970):

$$\underline{H}(\underline{r}) = \underline{H}^i(\underline{r}) + \int_V \underline{G}_{HJ}(\underline{r} | \underline{r}_S) \underline{J}^S(\underline{r}_S) dV_S \quad \text{Eq. 2.11}$$

to obtain the secondary magnetic field outside the scatterer where  $\underline{G}_{HJ}(\underline{r} | \underline{r}_S)$  is now the Green's tensor for the magnetic field due to a current element, and  $\underline{H}^i(\underline{r})$  is the incident (or primary) field at the observation point, assumed to be outside the scatterer.

$$\begin{bmatrix}
 [f_1^1 - \int_{Y_1} G_{YY}^1 S^1 dV_S] [f_1^1 - \int_{YY} G_{YY}^1 S^1 dV_S] [f_1^1 - \int_{YY} G_{YY}^1 S^1 dV_S] \\
 [f_1^2 - \int_{YY} G_{YY}^2 S^2 dV_S] [f_1^2 - \int_{YY} G_{YY}^2 S^2 dV_S] [f_1^2 - \int_{YY} G_{YY}^2 S^2 dV_S] \\
 [f_1^3 - \int_{YY} G_{YY}^3 S^3 dV_S] [f_1^3 - \int_{YY} G_{YY}^3 S^3 dV_S] [f_1^3 - \int_{YY} G_{YY}^3 S^3 dV_S] \\
 - \int_{ZY} G_{ZY}^1 S^1 dV_S - \int_{ZY} G_{ZY}^1 S^1 dV_S - \int_{ZY} G_{ZY}^1 S^1 dV_S \\
 - \int_{ZY} G_{ZY}^2 S^2 dV_S - \int_{ZY} G_{ZY}^2 S^2 dV_S - \int_{ZY} G_{ZY}^2 S^2 dV_S \\
 - \int_{ZY} G_{ZY}^3 S^3 dV_S - \int_{ZY} G_{ZY}^3 S^3 dV_S - \int_{ZY} G_{ZY}^3 S^3 dV_S
 \end{bmatrix}
 =
 \begin{bmatrix}
 a_1 \\
 a_2 \\
 a_3 \\
 b_1 \\
 b_2 \\
 b_3
 \end{bmatrix}
 =
 \begin{bmatrix}
 E_Y^1(r_1) \\
 E_Y^1(r_2) \\
 E_Y^1(r_3) \\
 E_Z^1(r_1) \\
 E_Z^1(r_2) \\
 E_Z^1(r_3)
 \end{bmatrix}$$

Figure 2-1 Simplified Matrix Equation: Equation 2.10

#### 2.4 General Remarks Concerning the Green's Tensor

To proceed further with the particular problem of a scatterer in a conductive half-space requires an understanding of how current flowing at a given point in the inhomogeneity affects and is affected by current flowing in other regions. This is tantamount to the mathematical development of the Green's tensor, which means we must solve for the electric field of an arbitrarily oriented dipole of unit dipole moment in the presence of a conductive half-space. For the past several decades this problem has been studied by radio engineers concerned with the radiation patterns of transmitters on the surface of the earth. More recently, studies of dipoles immersed in the half-space have been motivated by the need for communication between submarines beneath the surface of the conductive sea.

Before initiating a mathematical discussion of the half-space Green's tensor we note that the tensor may be divided into a primary part which accounts for waves propagating directly from the source, and a secondary part which accounts for the interface. For a dipole radiator below the surface, Figure 2-2 shows a diagrammatic ray-path interpretation of how energy arrives at the observation point. One ray propagates directly from the source, another is reflected from the interface and a third propagates up to the surface, along the interface in the non-conducting air, during which time energy is being refracted back into the earth. It is worth noting that



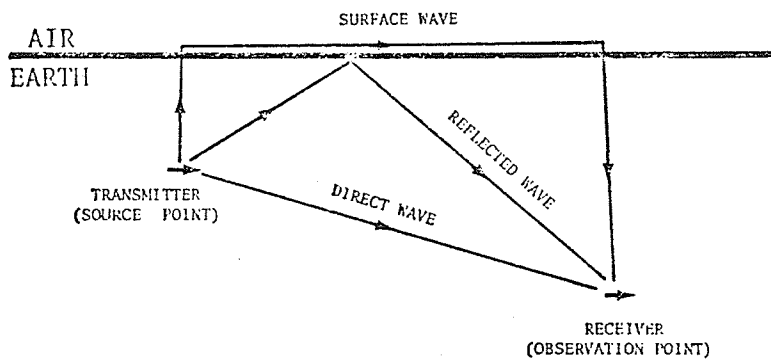


Figure 2-2 Diagrammatic Ray Path Interpretation of Energy Propagating from Transmitter to Receiver

the waves represented by rays in Figure 2-2 are diffusive waves (the square of the propagation constant is pure imaginary) rather than ordinary propagating waves in the usual sense; also that the distances involved are much less than a wavelength. Some salient mathematical characteristics of the Green's tensor are that the primary part is singular when source and observation points coincide, and that the secondary part vanishes when the boundary recedes to infinity, or when there is no conductivity contrast between the two media.

This specific communications problem is inherent in the geophysical problem at hand and is recognized in the interactions between the manifold infinitesimal parts of the current distribution which flows throughout the continuum of the scatterer. For inter-submarine communication where the lateral separation is large (compared to depth) the refracted wave is the only contributor to the energy arriving at the receiver; all other modes being prohibitively attenuated by the lossy medium. However, in the present problem -- the solution of the integral equation -- the transmitter and receiver locations are not only close but at times even coincident and we anticipate that the direct wave described by the primary part will usually be the dominant mode.

## CHAPTER III

### CALCULATION AND INTEGRATION OF THE PRIMARY PART OF THE GREEN'S TENSOR

#### 3.1 Introduction

As the treatment of the primary part of the Green's tensor constitutes a serious difficulty, it is worth concentrating on the canonical problem of finding the electric field in and about a known volume distribution of current in a lossless medium of infinite expanse. Generalization of the theory to include conductive media will be the subject of Section 3.4.

The Green's tensor is a generalized function (matrix) for which the independent variables are the observation point  $\underline{r}$  and the source point  $\underline{r}_s$ , and which operates upon the current density  $\underline{J}$  at  $\underline{r}_s$ . The dependent variable is the electric field  $\underline{E}$ . More explicitly

$$\underline{E}(\underline{r}) = \underline{G}(\underline{r}|\underline{r}_s) \underline{J}(\underline{r}_s) \quad \text{Eq. 3.1}$$

which in Cartesian coordinates is

$$\begin{bmatrix} E_x(\underline{r}) \\ E_y(\underline{r}) \\ E_z(\underline{r}) \end{bmatrix} = \begin{bmatrix} G_{xx}(\underline{r}|\underline{r}_s) & G_{xy}(\underline{r}|\underline{r}_s) & G_{xz}(\underline{r}|\underline{r}_s) \\ G_{yx}(\underline{r}|\underline{r}_s) & G_{yy}(\underline{r}|\underline{r}_s) & G_{yz}(\underline{r}|\underline{r}_s) \\ G_{zx}(\underline{r}|\underline{r}_s) & G_{zy}(\underline{r}|\underline{r}_s) & G_{zz}(\underline{r}|\underline{r}_s) \end{bmatrix} \begin{bmatrix} J_x(\underline{r}_s) \\ J_y(\underline{r}_s) \\ J_z(\underline{r}_s) \end{bmatrix} \quad \text{Eq. 3.2}$$

Columns one, two and three of the matrix are the electric field

vectors produced at  $\underline{r}$  by unit electric dipoles oriented in the x-, y- and z- directions respectively and located at  $\underline{r}_s$ .  $J_x$ ,  $J_y$  and  $J_z$  designate the components of  $\underline{J}$ .

Chapters III and IV are devoted exclusively to the development (and integration) of specific expressions for the Green's functions. In these chapters the source terms,  $\underline{J}$  and its components, are taken to be specific impressed currents, the effects (i.e., the radiated fields) of which are to be calculated. While these impressed currents will not actually be identified with the scatter currents,  $\underline{J}^S$ , of the previous chapter, the expressions for the radiated fields for sources of unit strength will be used for the various Green's functions in Equation 2.3.

### 3.2 The Green's Tensor: Point Source

To obtain the first column of the matrix one must solve for  $\underline{E}(\underline{r})$  due to a point current element  $\underline{J}_x = \hat{i} \delta(\underline{r} - \underline{r}_s)$ . The second and third columns use  $\underline{J}_y = \hat{j} \delta(\underline{r} - \underline{r}_s)$  and  $\underline{J}_z = \hat{k} \delta(\underline{r} - \underline{r}_s)$ . One proceeds with a general treatment using the scalar  $\phi$ , and vector  $\underline{A}$ , Lorentz potentials from which the fields may be derived via

$$\underline{H} = \frac{1}{\mu} \nabla \times \underline{A} \quad \text{Eq. 3.3}$$

$$\underline{E} = -\nabla \phi - i\omega \underline{A} \quad \text{Eq. 3.4}$$

(Harrington, 1961, p. 77) where both  $\phi$  and the components of  $\underline{A}$  satisfy the Helmholtz equations in rectangular coordinates

$$\nabla^2 \underline{A} - \gamma^2 \underline{A} = -\mu \underline{J} \quad \text{Eq. 3.5}$$

$$\nabla^2 \phi - \gamma^2 \phi = -\rho_c / \epsilon \quad \text{Eq. 3.6}$$

for  $e^{+i\omega t}$  time dependence of fields.  $\rho_c$  is the free charge

density and, in free space,  $\gamma^2 = -\mu\epsilon\omega^2$ . The validity of Equation 3.3 rests on the fact that  $\nabla \cdot \underline{\underline{B}} = 0$  and is true for many choices of the potential  $\underline{\underline{A}}$  given some  $\underline{\underline{H}}$ . Equations 3.5 and 3.6 follow if the Lorentz condition

$$\nabla \cdot \underline{\underline{A}} = i\omega\mu\epsilon\phi \quad \text{Eq. 3.7}$$

is operative. This reduces the arbitrariness of  $\underline{\underline{A}}$  and  $\phi$  and ensures that they satisfy the wave equation as do the fields.

The solutions of Equations 3.5 and 3.6 in homogeneous three-dimensional space are respectively

$$\underline{\underline{A}}(\underline{\underline{r}}) = \mu \underline{\underline{J}}(\underline{\underline{r}}_s) \frac{e^{-\gamma|\underline{\underline{r}}-\underline{\underline{r}}_s|}}{4\pi|\underline{\underline{r}}-\underline{\underline{r}}_s|} \quad \text{Eq. 3.8}$$

and

$$\phi(\underline{\underline{r}}) = \frac{\rho_e(\underline{\underline{r}}_s)}{\epsilon} \frac{e^{-\gamma|\underline{\underline{r}}-\underline{\underline{r}}_s|}}{4\pi|\underline{\underline{r}}-\underline{\underline{r}}_s|} \quad \text{Eq. 3.9}$$

as justified by Harrington (1961, p. 77) and Van Bladel (1966, p. 214). Using Equations 3.7 and 3.8, we can rewrite Equation 3.4 to give the electric field in terms of the current source.

That is

$$\underline{\underline{E}}(\underline{\underline{r}}) = \frac{1}{i\omega\epsilon} \nabla \left[ \nabla \cdot \underline{\underline{J}}(\underline{\underline{r}}_s) \frac{e^{-\gamma|\underline{\underline{r}}-\underline{\underline{r}}_s|}}{4\pi|\underline{\underline{r}}-\underline{\underline{r}}_s|} \right] - i\omega\mu \underline{\underline{J}}(\underline{\underline{r}}_s) \frac{e^{-\gamma|\underline{\underline{r}}-\underline{\underline{r}}_s|}}{4\pi|\underline{\underline{r}}-\underline{\underline{r}}_s|}. \quad \text{Eq. 3.10}$$

The contribution to the electric field  $\underline{\underline{E}}(\underline{\underline{r}})$  due to the x-component of the point current source  $\underline{\underline{J}}_x(\underline{\underline{r}}_s)$  is obtained by substituting  $\underline{\underline{J}}_x(\underline{\underline{r}}_s) \hat{i} = \underline{\underline{J}}(\underline{\underline{r}}_s)$  into Equation 3.10 and is given by

$$\underline{\underline{E}}_x(\underline{\underline{r}}) = \left[ \begin{array}{c} \frac{\partial^2}{\partial x^2} - \gamma^2 \\ \frac{\partial^2}{\partial y \partial x} \\ \frac{\partial^2}{\partial z \partial x} \end{array} \right] \frac{e^{-\gamma|\underline{\underline{r}}-\underline{\underline{r}}_s|}}{4\pi i \epsilon \omega |\underline{\underline{r}}-\underline{\underline{r}}_s|} \underline{\underline{J}}_x(\underline{\underline{r}}_s).$$

When similar expressions are developed for contributions to the electric field from the y- and z- components of the current source the results can be summed and expressed in matrix notation as

$$\vec{E}(\vec{r}) = \frac{1}{4\pi i \epsilon \omega} \begin{bmatrix} \frac{\partial^2}{\partial x^2} - \gamma^2 & \frac{\partial^2}{\partial x \partial y} & \frac{\partial^2}{\partial x \partial z} \\ \frac{\partial^2}{\partial y \partial x} & \frac{\partial^2}{\partial y^2} - \gamma^2 & \frac{\partial^2}{\partial y \partial z} \\ \frac{\partial^2}{\partial z \partial x} & \frac{\partial^2}{\partial z \partial y} & \frac{\partial^2}{\partial z^2} - \gamma^2 \end{bmatrix} \frac{e^{-\gamma |\vec{r} - \vec{r}_s|}}{|\vec{r} - \vec{r}_s|} \vec{J}(\vec{r}_s) \quad \text{Eq. 3.11}$$

where the square brackets enclose a matrix operator to be referred to as the Green's Tensor for a point source.

### 3.3 Green's Tensor: Distributed Source

For distributed sources  $\vec{J}$  and  $\rho_c$ , the current and charge in a volume element  $dV_s$  centred at  $\vec{r}_s$  are  $\vec{J} dV_s$  and  $\rho_c dV_s$  respectively. Summing the contributions from all such elements allows one to write the Lorentz potentials for extended sources (in rectangular coordinates) as

$$\phi(\vec{r}) = \frac{1}{4\pi \epsilon} \int_V \rho_c(\vec{r}_s) \frac{e^{-\gamma |\vec{r} - \vec{r}_s|}}{|\vec{r} - \vec{r}_s|} dV_s \quad \text{Eq. 3.12}$$

and

$$\vec{A}(\vec{r}) = \frac{\mu}{4\pi} \int_V \vec{J}(\vec{r}_s) \frac{e^{-\gamma |\vec{r} - \vec{r}_s|}}{|\vec{r} - \vec{r}_s|} dV_s. \quad \text{Eq. 3.13}$$

Henceforth we use the definition

$$\psi = \frac{e^{-\gamma |\vec{r} - \vec{r}_s|}}{|\vec{r} - \vec{r}_s|} \quad \text{Eq. 3.14}$$

Equation 3.12 can be revised with the equations of conservation of charge

$$\rho_c = -\frac{1}{i\omega} \nabla \cdot \underline{\underline{J}}$$

$$\rho_s = \frac{1}{i\omega} \hat{\underline{\underline{u}}} \cdot \underline{\underline{J}}$$

where  $\rho_s$  is the surface charge density and  $\hat{\underline{\underline{u}}}$  is a unit normal vector out of the region. Equation 3.12 is now

$$\phi(\underline{\underline{r}}) = \frac{-1}{4\pi i \epsilon \omega} \int_V [\nabla_{\underline{\underline{s}}} \cdot \underline{\underline{J}}(\underline{\underline{r}}_s)] \psi dV_s + \frac{1}{4\pi i \epsilon \omega} \int_S \psi \underline{\underline{J}}(\underline{\underline{r}}_s) \cdot d\underline{\underline{s}} \quad \text{Eq. 3.15}$$

Equation 3.4 with Equations 3.13 and 3.15 permit calculation of the electric field at  $\underline{\underline{r}}$  by summing the contributions from the scalar and the vector potentials. This gives

$$\underline{\underline{E}}(\underline{\underline{r}}) = \frac{-\nabla}{4\pi i \epsilon \omega} \left\{ - \int_V [\nabla_{\underline{\underline{s}}} \cdot \underline{\underline{J}}(\underline{\underline{r}}_s)] \psi dV_s + \int_S \psi \underline{\underline{J}}(\underline{\underline{r}}_s) \cdot d\underline{\underline{s}} \right\} - \frac{i\omega \mu}{4\pi} \int_V \underline{\underline{J}}(\underline{\underline{r}}_s) \psi dV_s \quad \text{Eq. 3.16}$$

where the first term in braces represents  $\nabla \phi$  and the second term is  $i\omega \underline{\underline{A}}$ . Applying the identity

$$\psi \nabla_{\underline{\underline{s}}} \cdot \underline{\underline{J}} = \nabla_{\underline{\underline{s}}} \cdot \psi \underline{\underline{J}} - \underline{\underline{J}} \cdot \nabla_{\underline{\underline{s}}} \psi$$

to the first integral and using the divergence theorem gives

$$- \int_V [\nabla_{\underline{\underline{s}}} \cdot \underline{\underline{J}}(\underline{\underline{r}}_s)] \psi dV_s = - \int_S \psi \underline{\underline{J}}(\underline{\underline{r}}_s) \cdot d\underline{\underline{s}} + \int_V \underline{\underline{J}} \cdot \nabla_{\underline{\underline{s}}} \psi dV_s$$

which reduces Equation 3.16 to

$$\underline{\underline{E}}(\underline{\underline{r}}) = \frac{1}{4\pi i \epsilon \omega} \left\{ -\nabla \int_V \underline{\underline{J}}(\underline{\underline{r}}_s) \cdot \nabla_{\underline{\underline{s}}} \psi dV_s - \gamma^2 \int_V \underline{\underline{J}}(\underline{\underline{r}}_s) \psi dV_s \right\}. \quad \text{Eq. 3.17}$$

Carrying the  $\nabla$  operator inside the integral (not valid when  $\underline{\underline{J}}(\underline{\underline{r}}_s) \cdot \nabla_{\underline{\underline{s}}} \psi$  is ill-behaved, according to Van Bladel (1964, p299) and rearranging the terms, we have

$$\underline{\underline{E}}(\underline{\underline{r}}) = \frac{1}{4\pi i \epsilon \omega} \left\{ - \int_V \nabla [\underline{\underline{J}}(\underline{\underline{r}}_s) \cdot \nabla_{\underline{\underline{s}}} \psi] dV_s - \gamma^2 \int_V \underline{\underline{J}}(\underline{\underline{r}}_s) \psi dV_s \right\}. \quad \text{Eq. 3.18}$$

Alternatively we can substitute Equation 3.13 and Equation 3.7 directly into Equation 3.4 to obtain (in rectangular coordinates)

$$\tilde{E}(\tilde{r}) = \frac{1}{4\pi i \epsilon \omega} \left\{ \tilde{\nabla} \tilde{\nabla} \cdot \int_V \tilde{J}(\tilde{r}_s) \psi dV_s - \gamma^2 \int_V \tilde{J}(\tilde{r}_s) \psi dV_s \right\} . \quad \text{Eq. 3.19}$$

Evidently Equations 3.16 to 3.19 are alternate expressions for the same quantity (with due regard for the restrictions on Equation 3.18). When  $\tilde{J}(\tilde{r}_s)$  is regarded as the scatter current one can calculate the scatter field  $\tilde{E}^S(\tilde{r})$ , and any of these four equations can be used in conjunction with Equation 2.6 to provide a valid embarkation point for the subsequent numerical computation. Which of Equations 3.16 to 3.19 is chosen is largely a matter of convenience, and is dictated by such factors as the coordinate system, the shape of the region of integration, whether we will attempt numerical or analytical handling of the differential operators, and whether the test functions are localized gate functions or global functions defined over the entire scatterer.

In the calculations to be described, extensive use is made of Equation 3.18. We therefore expand the vector and differential operators of Equation 3.18 to establish a more direct link with Equation 2.10. If

$$\tilde{E}(\tilde{r}) = \begin{bmatrix} E_x \\ E_y \\ E_z \end{bmatrix} \quad \text{and} \quad \tilde{J}(\tilde{r}_s) = \begin{bmatrix} J_x \\ J_y \\ J_z \end{bmatrix}$$

then Equation 3.18 becomes



$$\begin{bmatrix} E_x \\ E_y \\ E_z \end{bmatrix} = \frac{1}{4\pi i \epsilon \omega} \int \begin{bmatrix} -\frac{\partial}{\partial x} \\ -\frac{\partial}{\partial y} \\ -\frac{\partial}{\partial z} \end{bmatrix} \left[ J_x \frac{\partial \psi}{\partial x_s} + J_y \frac{\partial \psi}{\partial y_s} + J_z \frac{\partial \psi}{\partial z_s} \right] - \gamma^2 \begin{bmatrix} J_x \\ J_y \\ J_z \end{bmatrix} \psi \, dV_s$$

Eq.3.20

It is worth noting that  $\tilde{J}(\tilde{r}_s)$  in Equation 3.18 is constant with respect to the  $\tilde{\nabla}$  operator. The similar dependence of  $\psi$  on the subscripted and unsubscripted coordinate variables allows substitution of

$$\frac{\partial \psi}{\partial x} = -\frac{\partial \psi}{\partial x_s}, \quad \frac{\partial \psi}{\partial y} = -\frac{\partial \psi}{\partial y_s} \quad \text{and} \quad \frac{\partial \psi}{\partial z} = -\frac{\partial \psi}{\partial z_s}$$

into Equation 3.20 to obtain, after some rearrangement of terms

$$\begin{bmatrix} E_x(\tilde{r}) \\ E_y(\tilde{r}) \\ E_z(\tilde{r}) \end{bmatrix} = \frac{1}{4\pi i \epsilon \omega} \int \begin{bmatrix} \frac{\partial^2 \psi}{\partial x^2} - \gamma^2 \psi & \frac{\partial^2 \psi}{\partial x \partial y} & \frac{\partial^2 \psi}{\partial x \partial z} \\ \frac{\partial^2 \psi}{\partial y \partial x} & \frac{\partial^2 \psi}{\partial y^2} - \gamma^2 \psi & \frac{\partial^2 \psi}{\partial y \partial z} \\ \frac{\partial^2 \psi}{\partial z \partial x} & \frac{\partial^2 \psi}{\partial z \partial y} & \frac{\partial^2 \psi}{\partial z^2} - \gamma^2 \psi \end{bmatrix} \begin{bmatrix} J_x(\tilde{r}_s) \\ J_y(\tilde{r}_s) \\ J_z(\tilde{r}_s) \end{bmatrix} dV_s$$

Eq.3.21

Equation 3.21 is a generalization to non-localized sources of Equation 3.11 for point sources. Matrix elements in Equation 3.21 not involving the  $x$ - variable are found in Equation 2.10 and these elements can now be defined as:

$$G_{yy}(\tilde{r}|\tilde{r}_s) = \frac{\partial^2 \psi}{\partial y^2} - \gamma^2 \psi$$

$$G_{yz}(\tilde{r}|\tilde{r}_s) = \frac{\partial^2 \psi}{\partial y \partial z}$$

$$G_{zy}(\underline{r}|\underline{r}_s) = \frac{\partial^2 \psi}{\partial z \partial y}$$

$$G_{zz}(\underline{r}|\underline{r}_s) = \frac{\partial^2 \psi}{\partial z^2} - \gamma^2 \psi \quad \text{Eqs. 3.22}$$

### 3.4 Generalization of the Theory to Include Lossy Media

The Ampere-Maxwell law states that

$$\nabla \times \underline{H} = \frac{\partial \underline{D}}{\partial t} + \underline{J}_{\text{tot}} \quad \text{Eq. 3.23}$$

where  $\underline{D} = \epsilon \underline{E}$

In lossless media the total current,  $\underline{J}_{\text{tot}}$ , includes nothing but the source current  $\underline{J}_s$  (and  $\underline{J}_s = \underline{J}_{\text{tot}}$ ). However, in conductive media, the source current radiates an electric field  $\underline{E}$  which in turn motivates current ( $\underline{J} = \sigma \underline{E}$ ) and Equation 3.23 should be written

$$\begin{aligned} \nabla \times \underline{H} &= \frac{\partial \underline{D}}{\partial t} + (\underline{J} + \underline{J}_s) \\ &= i\omega \left( \epsilon + \frac{\sigma}{i\omega} \right) \underline{E} + \underline{J}_s \end{aligned}$$

for  $e^{+i\omega t}$  time dependence of the fields. Using

$$\underline{D} = \epsilon^* \underline{E}$$

where

$$\epsilon^* = \epsilon \left( 1 + \frac{\sigma}{i\epsilon\omega} \right)$$

we return to Equation 3.23. Thus the theory for lossless media can be generalized to encompass dissipative media by replacing  $\epsilon$  with  $\epsilon \left( 1 + \frac{\sigma}{i\epsilon\omega} \right)$ .

It is noteworthy that from this point on  $\gamma$  will refer to the propagation constant in lossy media and is understood to be obtainable through

$$\gamma^2 = i\mu\omega (\sigma + i\epsilon\omega). \quad \text{Eq. 3.24}$$

### 3.5 Typical Tensor Elements

Expansion of the derivatives in Equations 3.22 leads to

$$\begin{aligned} G_{YY}(\underline{r}|\underline{r}_s) &= \frac{e^{-\gamma R}}{R} \left[ \frac{(y-y_s)^2}{R^2} \left( \gamma^2 + \frac{3\gamma}{R} + \frac{3}{R^2} \right) - \gamma^2 - \frac{\gamma}{R} - \frac{1}{R^2} \right] \\ G_{ZZ}(\underline{r}|\underline{r}_s) &= \frac{e^{-\gamma R}}{R} \left[ \frac{(z-z_s)^2}{R^2} \left( \gamma^2 + \frac{3\gamma}{R} + \frac{3}{R^2} \right) - \gamma^2 - \frac{\gamma}{R} - \frac{1}{R^2} \right] \\ G_{ZY}(\underline{r}|\underline{r}_s) &= G_{YZ}(\underline{r}|\underline{r}_s) = \frac{e^{-\gamma R}}{R} \frac{(y-y_s)(z-z_s)}{R^2} \left( \frac{\gamma + 3\gamma + 3}{R} + \frac{3}{R^2} \right) \end{aligned} \quad \text{Eq. 3.25}$$

where

$$R = |\underline{r} - \underline{r}_s| = [(x-x_s)^2 + (y-y_s)^2 + (z-z_s)^2]^{\frac{1}{2}}$$

To illustrate further the problems associated with Equation 2.10, an explicit form for the test function is now chosen, namely  $y^n z^m$  where  $n$  and  $m$  are integers. Test functions could also be linear combinations of these simple two variable polynomials (such as  $[1+y^n]z^m$  for example), as will be discussed in Chapter VI. However, the treatment (at least for singular integrands) of the linear combination would still be done term by term. So for simple test functions such as  $y^n z^m$ , it is apparent that matrix elements in Equation 2.10 will have one of the following forms:

$$y^n z^m - (\sigma_3 - \sigma_2) \int_V \frac{e^{-\gamma R}}{R} \left[ \frac{(y-y_s)^2}{R^2} \left( \gamma^2 + \frac{3\gamma}{R} + \frac{3}{R^2} \right) - \gamma^2 - \frac{\gamma}{R} - \frac{1}{R^2} \right] y_s^n z_s^m dV_s,$$

$$y^n z^m - (\sigma_3 - \sigma_2) \int_V \frac{e^{-\gamma R}}{R} \left[ \frac{(z-z_s)^2}{R^2} \left( \gamma^2 + \frac{3\gamma}{R} + \frac{3}{R^2} \right) - \gamma^2 - \frac{\gamma}{R} - \frac{1}{R^2} \right] y_s^n z_s^m dV_s,$$

or

$$-(\sigma_3 - \sigma_2) \int_V \frac{e^{-\gamma R}}{R} \frac{(y-y_S)(z-z_S)}{R^2} \left(\gamma^2 + \frac{3\gamma+3}{R} \frac{1}{R^2}\right) y_S^n z_S^m dV_S$$

where  $n$  and  $m$  are integers with values governed by the test function in use.

### 3.6 Integration of the Source Point over the Observation Point

When the source point and observation point coincide, the integrands expressed in Cartesian coordinations can be ill-behaved. The value of the integrands may depend on the direction from which  $\underline{r}_S$  approaches  $\underline{r}$ ; a problem alluded to by Van Bladel (1961). To circumvent this difficulty, the observation point is surrounded by a spherical region within which the integrands are recast in spherical coordinates. In this coordinate system the volume element goes to zero in the manner of  $R^2$  and this behaviour, coupled with the  $R^{n+m}$  behaviour of the test function, is enough (with the exception of the zeroth degree test function) to overpower the pole in the Green's function. A demonstration will clarify the matter.

A typical matrix element involving, say, the  $G_{yy}$  element of the Green's tensor at match point  $\underline{r}_1$  is

$$\begin{aligned} I &= \int_V G_{yy}(r|r_S) y_S^n z_S^m dV_S \\ &= \int_{z_L}^{z_U} \int_{y_L}^{y_U} \int_{x_L}^{x_U} \frac{e^{-\gamma R}}{R} \left[ \frac{(y-y_S)^2}{R} \left(\gamma^2 + \frac{3\gamma+3}{R} \frac{1}{R^2}\right) - \frac{\gamma-1}{R} \frac{1}{R^2} \right] y_S^n z_S^m dx_S dy_S dz_S \end{aligned} \quad \text{Eq. 3.26}$$

where  $R = [(x_1 - x_S)^2 + (y_1 - y_S)^2 + (z_1 - z_S)^2]^{\frac{1}{2}}$

and  $x_L, x_U, y_L, y_U, z_L$  and  $z_U$  are the upper and lower integration limits of the  $x, y$  and  $z$  variables. It is convenient to isolate

the singularity at the centre of a cube, the sides of which equal the thickness,  $\Delta x$ , of the scatterer. Equation 3.26 becomes

$$I = \int_{z_1 - \frac{\Delta x}{2}}^{z_1 + \frac{\Delta x}{2}} \int_{y_1 - \frac{\Delta x}{2}}^{y_1 + \frac{\Delta x}{2}} \int_{x_1 - \frac{\Delta x}{2}}^{x_1 + \frac{\Delta x}{2}} \frac{e^{-\gamma R}}{R} \left[ \frac{(y_1 - y_s)^2}{R^2} \frac{(\gamma^2 + 3\gamma + 3)}{R} \frac{-\gamma^2 - \gamma - 1}{R} \right] y_s^n z_s^m dx_s dy_s dz_s + [\text{Integrals over non-singular regions}].$$

Integrals over the non-singular regions can be handled using standard quadrature techniques and do not warrant further discussion here. Concerning the cube with the singularity, however, we apply the transformation

$$x_s = x_s + x_1$$

$$y_s = y_s + y_1$$

$$z_s = z_s + z_1$$

to obtain

$$I_{\text{SING}} = \int_{-\Delta x/2}^{\Delta x/2} \int_{-\Delta x/2}^{\Delta x/2} \int_{-\Delta x/2}^{\Delta x/2} \frac{e^{-\gamma R}}{R} \left[ \frac{y_s^2}{R^2} \frac{(\gamma^2 + 3\gamma + 3)}{R} \frac{-\gamma^2 - \gamma - 1}{R} \right] \times (y_s + y_1)^n (z_s + z_1)^m dx_s dy_s dz_s \quad \text{Eq. 3.26a}$$

where the expression for  $R$  is now simplified to

$$R = (x_s^2 + y_s^2 + z_s^2)^{\frac{1}{2}}.$$

Using Newton's binomial expansion formula further simplification is possible:

$$I_{\text{SING}} = \sum_{j=1}^{n+1} \frac{n! y^{n-j+1}}{(n-j+1)! (j-1)!} \sum_{k=1}^{m+1} \frac{m! z^{m-k+1}}{(m-k+1)! (k-1)!} \int_{-\Delta x/2}^{\Delta x/2} \int_{-\Delta x/2}^{\Delta x/2} \int_{-\Delta x/2}^{\Delta x/2} \frac{e^{-\gamma R}}{R} \left[ \frac{y_s^2}{R^2} \frac{(\gamma^2 + 3\gamma + 3)}{R} \frac{-\gamma^2 - \gamma - 1}{R} \right] y_s^{j-1} z_s^{k-1} dx_s dy_s dz_s$$

$$\text{Eq. 3.27}$$

It is apparent that when  $j$  or  $k$  or both are even integers, the integrand is an odd function over the limits of integration and the integral can be set to zero. For other values of  $j$  and  $k$  the integrand exhibits the ill-behaviour mentioned earlier. The volume of the cube is subdivided by an inscribed sphere into two regions: a sphere of diameter  $\Delta x$  and a remainder. Denoting the integral in Equation 3.27 and  $I_{\text{SING}}^{\text{CUBE}}$ , we designate

$$I_{\text{SING}}^{\text{CUBE}} = I_{\text{SING}}^{\text{SPHERE}} + I_{\text{SING}}^{\text{REMAINDER}}$$

In the 'remainder' region (cube minus sphere) it is convenient to transform to cylindrical coordinates through

$$y = y$$

$$x = r \cos \phi$$

$$z = r \sin \phi$$

Due cogitation over the limits of integration for this irregularly shaped region will now give

$$I_{\text{SING}}^{\text{REMAINDER}} = 8 \int_{y=0}^{\Delta x/2} \int_{\phi=0}^{\pi} \int_{R_{\text{LO}}}^{R_{\text{UP}}} \frac{e^{-\gamma R}}{R} \left[ \frac{y^2}{R^2} (\gamma^2 + 3\frac{\gamma}{R} + 3\frac{1}{R^2}) - \gamma^2 - \frac{\gamma}{R} - \frac{1}{R^2} \right] y^{j-1} (r \sin \phi)^{k-1} r dr d\phi dy$$

Eq. 3.28

$$\text{where } R = (r^2 + y^2)^{\frac{1}{2}}$$

$$R_{\text{UP}} = \begin{cases} \frac{\Delta x/2}{\cos \phi} ; & 0 \leq \phi \leq \frac{\pi}{4} \\ \frac{\Delta x/2}{\sin \phi} ; & \frac{\pi}{4} \leq \phi \leq \frac{\pi}{2} \end{cases}$$

$$\text{and } R_{\text{LO}} = (\Delta x/2 - y^2)^{\frac{1}{2}}$$

The integrand in this region is never singular and is handled with standard quadrature methods.

Inside the sphere, transformation to spherical coordinates

using

$$y = R \cos \theta$$

$$x = R \sin \theta \cos \phi$$

$$z = R \sin \theta \sin \phi$$

yields  $I_{\text{SPHERE}}^{\text{SING}} =$

$$\int_{\phi=0}^{2\pi} \int_{\theta=0}^{\pi} \int_{R=0}^{\Delta x/2} \frac{e^{-\gamma R}}{R} \left[ \frac{R^2 \cos^2 \theta}{R^2} (\gamma^2 + \frac{3\gamma+3}{R} \frac{1}{R^2}) - \gamma^2 - \frac{\gamma-1}{R} \frac{1}{R^2} \right] (R \cos \theta)^{j-1} \times \\ (R \sin \theta \sin \phi)^{k-1} R^2 dR \sin \theta d\theta d\phi$$

$$= \int_{R=0}^{\Delta x/2} e^{-\gamma R} R^{j+k-1} (\gamma^2 + \frac{3\gamma+3}{R} \frac{1}{R^2}) dR \int_{\theta=0}^{\pi} \cos^{j+1} \theta \sin^k \theta d\theta \int_{\phi=0}^{2\pi} \sin^{k-1} \phi d\phi \\ + \int_{R=0}^{\Delta x/2} e^{-\gamma R} R^{j+k-1} (-\gamma^2 - \frac{\gamma-1}{R} \frac{1}{R^2}) dR \int_{\theta=0}^{\pi} \cos^{j-1} \theta \sin^k \theta d\theta \int_{\phi=0}^{2\pi} \sin^{k-1} \phi d\phi$$

Eq. 3.29

The variables have separated and it is seen that the R integrands are non-singular except when j and k are unity. (When j=1 or k=2 or both, one or both of the integrals over the angular variables will vanish and the remaining singularity in the R integrand can be ignored.) These regular functions can be integrated using standard quadrature methods. When j and k are unity we are dealing with a zero degree polynomial and integration of this term over the sphere requires special attention. It is best to recall that in this case we are evaluating the electric field at the centre of a sphere in which flows constant uni-directional current which vanishes outside the sphere. A similar problem is solved by Van Bladel (1961) who considers current in a cylindrical region. The starting point

is Equation 3.16. The development is similar for the zero degree terms of both vector components. Choosing the y-component we set

$$\underline{\underline{J}}(\underline{\underline{r}}) = J \hat{j}$$

Since  $\nabla \cdot \underline{\underline{J}}(\underline{\underline{r}}) = 0$ , Equation 3.16 becomes

$$\underline{\underline{E}}(\underline{\underline{r}}) = - \frac{J}{4\pi i \epsilon \omega} \nabla \int_S \psi \hat{j} \cdot d\underline{\underline{s}}_S - \frac{i\omega\mu J}{4\pi} \int_V \psi dV_S \hat{j}$$

scalar potential          vector potential

Using the results of Appendix A we have

$$\underline{\underline{E}}(\underline{\underline{o}}) = \frac{J}{i\epsilon\omega} \left[ \frac{2}{3} e^{-\gamma\Delta x/2} \left( \frac{\gamma\Delta x}{2} + 1 \right) - 1 \right] \hat{j} \quad \text{Eq. 3.30}$$

### 3.7 Alternate Handling of the Zero Order Polynomial

Mathematically messier but computationally more efficient methods exist for handling the integrals involving the zero order polynomial both for regions including, and not including, the match point.

Consider a rectangular volume centred about the origin. If the cube is subdivided by an inscribed cylinder (axis parallel to the current flow) most of the integration can be done analytically. Van Bladel (1961) computes the electric field at the centre of a cylinder as previously mentioned and illustrated in Figure 3.1. He shows that

$$\underline{\underline{E}}_y(\underline{\underline{o}}) = \frac{J a}{\sigma + i\epsilon\omega} \left[ -\frac{e^{-\gamma a}}{a} + \frac{e^{-\gamma(a^2+b^2)^{\frac{1}{2}}}}{(a^2+b^2)^{\frac{1}{2}}} \right] + \left( \frac{i\omega\mu}{\sigma + i\epsilon\omega} \right)^{\frac{1}{2}} \int_0^a e^{-\gamma(b^2+y^2)^{\frac{1}{2}}} dy + \frac{J(e^{-\gamma a} - 1)}{\sigma + i\epsilon\omega} \quad \text{Eq. 3.31}$$



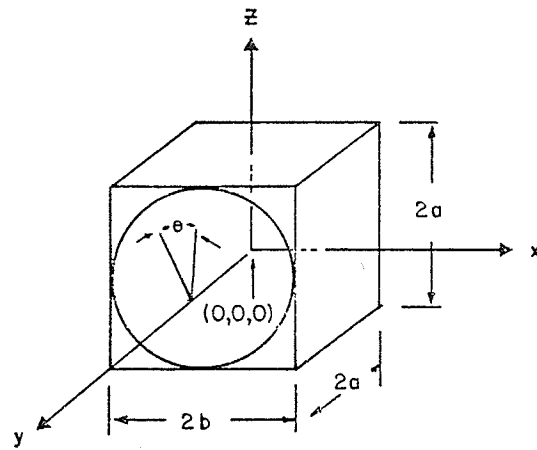


Figure 3-1 Cylindrical Region of Current Centred about the Singular Point

and uses the method described earlier for the sphere.

For the field at the origin, the volume of current outside the cylinder but inside the rectangular volume, Equation 3.18 can be used. For constant y-directed current (zero degree term) Equation 3.18 can be written

$$\tilde{E}_y(\tilde{0}) = \frac{\hat{J}_y}{4\pi i \epsilon \omega} \int_V \left[ \frac{\partial^2}{\partial y^2} \psi - \gamma^2 \psi \right] dV_S \quad \text{Eq. 3.32}$$

where terms involving  $\hat{i} \frac{\partial^2}{\partial y \partial x}$  and  $\hat{k} \frac{\partial^2}{\partial y \partial z}$  have been eliminated through symmetry considerations. Recalling that  $\psi$  satisfies the wave equation and is constant with respect to the angular variable, Equation 3.32 can be written in cylindrical coordinates as

$$E_y(\tilde{0}) = \frac{-8J}{4\pi(\sigma + i\epsilon\omega)} \int_{y=-a}^a \int_{\theta=0}^{\pi/4} \int_{r=b}^{b/\cos\theta} \frac{\partial}{\partial r} \left( r \frac{\partial \psi}{\partial r} \right) dr d\theta dy$$

where the prefixed constant has been adjusted for lossy media. Manipulation of the integrals eventually gives

$$E_y(\tilde{0}) = \frac{-8J}{4\pi(\sigma + i\epsilon\omega)} \int_{\theta=0}^{\pi/4} \left[ \frac{2r^2 e^{-\gamma R_c}}{y R_c} \Big|_{y=-a}^a + r^2 \int_{y=-a}^a \frac{e^{-\gamma R_c}}{y^2 R} dy \right] \Big|_{r=b}^{b/\cos\theta} d\theta \quad \text{Eq. 3.33}$$

where  $R_c = (r^2 + y^2)^{\frac{1}{2}}$ . Further reduction is possible using a power series expansion for  $e^{-\gamma R_c}$  and integrating term by term over  $y$ . The field at the centre due to the current in the entire rectangular region is obtained by summing the right hand sides of Equations 3.31 and 3.33.

For rectangular volumes not including the match point, much of the integration involving the zero order terms can

again be done analytically. For y-directed current, Equation 3.18 can be expanded into

$$\vec{E}(\vec{r}) = \frac{1}{4\pi(\sigma + i\epsilon\omega)} \int_V \left[ \hat{i} \frac{\partial^2 \psi}{\partial x_s \partial y_s} + \hat{j} \left( \frac{\partial^2 \psi}{\partial y_s^2} - \gamma^2 \psi \right) + \hat{k} \frac{\partial^2 \psi}{\partial z_s \partial y_s} \right] dV_s \quad \text{Eq. 3.34}$$

The x- and z- components can be reduced to surface integrals using identities of the form

$$\int_V \frac{\partial}{\partial x} f(x) dV = \int_S f(x) (\hat{u} \cdot \hat{i}) ds$$

where  $f(x)$  is a regular function and  $\hat{u}$  is the outward unit normal. Integrals of derivatives (with respect to the same variable) are seen to arise. If the limits of the region are  $x_L$  to  $x_u$ ,  $y_L$  to  $y_u$  and  $z_L$  to  $z_u$ , then the integrals defining the x- and z- components in Equation 3.34 become

$$\int_{z_L}^{z_u} \psi dz_s \int_{y_L}^{y_u} \int_{x_L}^{x_u} \quad \text{and} \quad \int_{x_L}^{x_u} \psi dx_s \int_{y_L}^{y_u} \int_{z_L}^{z_u}$$

respectively. The y-component in Equation 3.34 is more difficult because the integral over  $\psi$  is intractable. However, some reduction occurs using the relation

$$\frac{\partial^2 \psi}{\partial y^2} - \gamma^2 \psi = \frac{-\partial^2}{\partial x^2} \psi - \frac{\partial^2}{\partial z^2} \psi.$$

Clearly

$$\int_V \frac{\partial^2 \psi}{\partial x^2} dV_s = \int_{z_L}^{z_u} \int_{y_L}^{y_u} \frac{\partial \psi}{\partial x_s} dy_s dz_s \Big|_{x_L}^{x_u}$$

and with some effort can be shown to equal

$$- \left\{ (x - x_s) \int_{z_L}^{z_u} \frac{e^{-\gamma R}}{(y - y_s) R} dz_s \Big|_{y_L}^{y_u} - \int_{z_L}^{z_u} \int_{y_L}^{y_u} \frac{e^{-\gamma R}}{(y - y_s)^2 R} dy_s dz_s \right\} \Big|_{x_L}^{x_u}.$$

Further reduction is obtainable through a power series expansion of  $e^{-\gamma R}$  followed by term by term integration over the  $y$ -variable. The  $\partial^2\psi/\partial z^2$  term can be treated in similar fashion.

## CHAPTER IV

### CALCULATION AND INTEGRATION OF THE SECONDARY PART OF THE GREEN'S TENSOR

#### 4.1 Introduction

Chapter III discussed the development and integration of the primary part of the Green's tensor necessary for studying the fields in unbounded lossy media. This required solving the wave equation in infinite space, and was followed by a spatial integration process which generalized the results for a point source to give fields due to a volume distribution of sources. To study scattering in bounded media such as a half-space, a similar approach can be used but now it is necessary to solve for the fields in the presence of the interfaces. When expressions for the fields are developed, the primary terms will be recognized as those terms which receive special attention in the preceding chapter because of their singular behaviour when the source and observation points coincide. Although the secondary terms are non-singular, other difficulties arise in that it is not usually possible to express these terms in closed form. In general, the secondary terms are developed as Hankel transforms, the evaluation of which are

the subjects of Section 6.6.

Although it is possible to develop solutions for media having many parallel interfaces, this work is restricted to host media having not more than two boundaries (three regions). The upper region will invariably be assigned zero conductivity to simulate air, while the lower layers can be given values to simulate rock or overburden as desired. The conductive regions will be referred to collectively as a two-layer earth.

In Chapter III, dealing with unbounded space, the first column of the matrix was established explicitly, while the second and third columns were established through symmetry. To establish the Green's tensor in the presence of the interfaces requires separate solutions, since symmetry between vertical (perpendicular to the plane interfaces) and horizontal source dipoles does not occur.

To solve Equation 2.6 for the eddy currents in a scatterer imbedded in the lower semi-infinite layer requires a generalization of Equation 3.11. Establishing the first column of the generalized tensor requires solving for the field  $\vec{E}(\vec{r})$  due to a horizontal x-oriented electric dipole source, while the third column requires the electric field from a vertical z-oriented source. The second column is established from the first using symmetry.

The two problems to be discussed in Sections 4.2 and 4.3 have been well understood for many years. However, it is not possible to find in the literature solutions which employ consistent coordinate systems and notations, and which place



the source point and observation point in the appropriate media. For the above reasons and for clarity and completeness of the overall argument, solutions to these problems are included.

Although Chapters III and IV might have been combined, they remain separate largely because of the profound differences in the numerical handling of the primary and secondary parts of the Green's tensor. Furthermore, geophysically important extensions of this work such as electromagnetic effects in bore holes or mine tunnels may not require the secondary part and simplification of the problem can be achieved through its exclusion.

#### 4.2 A Horizontal Electric Dipole in the Lower Layer of a Two-Layer Earth

Figure 4-1 depicts a horizontal electric dipole in a space ordered by a Cartesian coordinate system. The dipole is at the origin and oriented in the x-direction. The z-direction is positive downward and the conductivity interfaces are planes perpendicular to the z-axis and intersecting the z-axis at  $z = -h$  and  $z = -(h+d)$ . Progressing from top to bottom, the three regions have conductivities  $\sigma_0$ ,  $\sigma_1$  and  $\sigma_2$ .

The fields can be computed through the Hertz electric vector potential  $\tilde{\pi}$  and the details of the calculation of  $\tilde{\pi}$  are given in Appendix B. The electric field, in rectangular coordinates, is given by (Ward, 1967, p. 99)

$$\tilde{E} = \nabla \nabla \cdot \tilde{\pi} - \gamma^2 \tilde{\pi} \quad \text{Eq. 4.1}$$

and the magnetic field by

$$\tilde{H} = (\sigma + i\epsilon\omega) \nabla \times \tilde{\pi} \quad \text{Eq. 4.2}$$

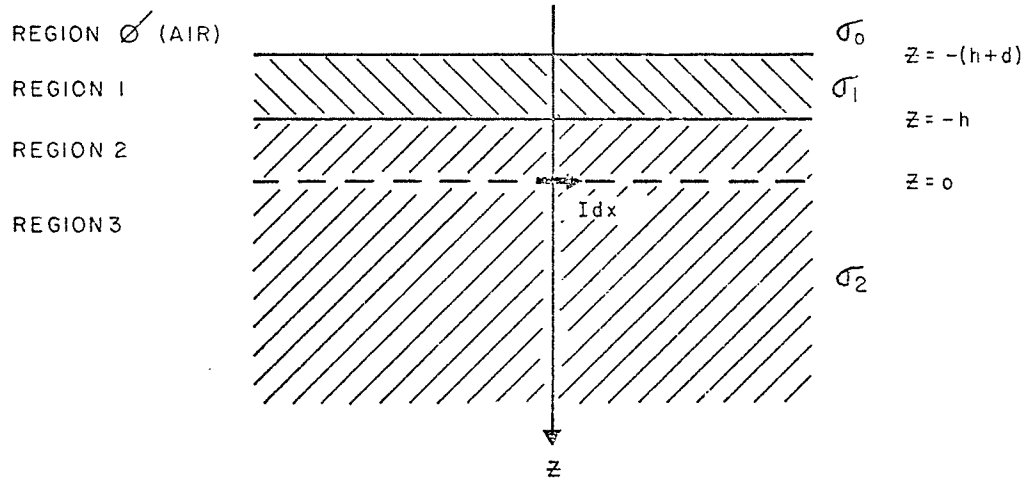


Figure 4-1 Horizontal Electric Dipole in a Two-Layer Earth



where the components of  $\underline{\pi}$  satisfy the wave equation in each region. The lack of symmetry gives the Hertz potential two components, and in general we write for the  $n^{\text{th}}$  region

$$\underline{\pi}_n = \pi_{x_n} \hat{i} + \pi_{z_n} \hat{k} \quad \text{Eq. 4.3}$$

where  $n=0,1,2$  or  $3$  specifying the regions as depicted in Figure 4.1. Although regions 2 and 3 have the same physical properties, they are separated because distinct solutions exist above and below the dipole.

The x-component of the potential in the four regions can be written as follows

$$\text{in air} \quad \pi_{x_0} = c \int_0^{\infty} \psi_1(\lambda) e^{u_0 z} J_0(\lambda \rho) d\lambda \quad \text{Eq. 4.4}$$

$$\text{in Region 1} \quad \pi_{x_1} = c \int_0^{\infty} [\psi_2(\lambda) e^{u_1 z} + \psi_3(\lambda) e^{-u_1 z}] J_0(\lambda \rho) d\lambda \quad \text{Eq. 4.5}$$

$$\text{in Region 2} \quad \pi_{x_2} = c \int_0^{\infty} [\psi_4(\lambda) e^{u_2 z} + \psi_5(\lambda) e^{-u_2 z}] J_0(\lambda \rho) d\lambda \quad \text{Eq. 4.6}$$

$$\text{in Region 3} \quad \pi_{x_3} = c \int_0^{\infty} [\psi_4(\lambda) e^{-u_2 z} + \psi_5(\lambda) e^{-u_2 z}] J_0(\lambda \rho) d\lambda \quad \text{Eq. 4.7}$$

where  $c = Idx/4\pi\kappa_2$ ,  $\kappa_n = (\sigma_n + i\epsilon\omega)$ ,  $u_n^2 = \lambda^2 + \gamma_n^2$ , for media

defined by  $n=0,1,2$  or  $3$  and  $\gamma_n$  is the propagation constant.

Furthermore

$$\psi_1(\lambda) = \frac{4\kappa_2 u_1 \lambda e^{u_0(h+d) - u_1 d - u_2 h}}{\kappa_0 \text{ DEN}} \quad \text{Eq. 4.8}$$

$$\psi_2(\lambda) = \frac{2\kappa_2 \lambda (u_0 + u_1) e^{(u_1 - u_2) h}}{\kappa_1 \text{ DEN}} \quad \text{Eq. 4.9}$$

$$\psi_3(\lambda) = \frac{-2\kappa_2 \lambda (u_0 - u_1) e^{-u_1(h+d) - u_1 d - u_2 h}}{\kappa_1 \text{ DEN}} \quad \text{Eq. 4.10}$$

$$\psi_4(\lambda) = \frac{\lambda}{u_2} \quad \text{Eq. 4.11}$$

and

$$\psi_5(\lambda) = \frac{-\lambda^2 [(-u_0 - u_1)(-u_1 + u_2) + (u_0 - u_1)(u_1 + u_2)] e^{-2u_1 d}}{u_2^2 \text{ DEN}} e^{-2u_2 h} \quad \text{Eq. 4.12}$$

where

$$\text{DEN} = (u_0 + u_1)(u_1 + u_2) + (u_1 - u_0)(u_2 - u_1) e^{-2u_1 d} \quad \text{Eq. 4.13}$$

In Equations 4.4 to 4.7,  $J_0(\lambda \rho)$  is the zeroth order Bessel function of the first kind and  $\rho = (x^2 + y^2)^{\frac{1}{2}}$  is the horizontal distance between the source and the observation points.

The z-components of the potential in the four regions are

$$\text{in air} \quad \pi_{z0} = \frac{x}{\rho} \int_0^{\infty} \phi_1(\lambda) e^{u_0 z} J_1(\lambda \rho) d\lambda$$

$$\text{in Region 1} \quad \pi_{z1} = \frac{x}{\rho} \int_0^{\infty} [\phi_2(\lambda) e^{u_1 z} + \phi_3(\lambda) e^{-u_1 z}] J_1(\lambda \rho) d\lambda$$

Eqs. 4.14

$$\text{in Region 2} \quad \pi_{z2} = \frac{x}{\rho} \int_0^{\infty} \phi_5(\lambda) e^{-u_2 z} J_1(\lambda \rho) d\lambda$$

$$\text{in Region 3} \quad \pi_{z3} = \frac{x}{\rho} \int_0^{\infty} \phi_5(\lambda) e^{-u_2 z} J_1(\lambda \rho) d\lambda$$

where

$$\phi_5(\lambda) = [-A_1 \kappa_1 (u_0 \kappa_1 + u_1 \kappa_0) e^{u_1 d} - 2A_2 u_1 \kappa_0 \kappa_1 + A_1 \kappa_1 (u_0 \kappa_1 - u_1 \kappa_0) e^{-u_1 d}] \times e^{-u_0(h+d)} / \text{DEN2} \quad \text{Eq. 4.15}$$

Where  $\text{DEN2} = [(u_0 \kappa_1 u_1 \kappa_2 + u_0 u_2 \kappa_1 \kappa_1 + u_1 u_1 \kappa_0 \kappa_2 + u_1 u_2 \kappa_0 \kappa_1)$

$$+ (u_0 u_1 \kappa_1 \kappa_2 - u_0 u_2 \kappa_1 \kappa_1 - u_1 u_1 \kappa_0 \kappa_2 + u_1 u_2 \kappa_0 \kappa_1) e^{-2u_1 d}] e^{-u_0(h+d) + u_1 d + u_2 h}, \quad \text{Eq. 4.16}$$

$$A_1 = c\lambda [-\psi_2(\lambda) e^{-u_1 h} - \psi_3(\lambda) e^{u_1 h} + \psi_4(\lambda) e^{-u_2 h} + \psi_5(\lambda) e^{u_2 h}],$$

and

$$A_2 = c\lambda [-\psi_1(\lambda)e^{-u_0(h+d)} + \psi_2(\lambda)e^{-u_1(h+d)} + \psi_3(\lambda)e^{u_1(h+d)}].$$

$J_1(\lambda p)$  is the first order Bessel function of the first kind.

When the scatterer occurs entirely within the lower layer, as will always be the case in this work, the eigenfunctions  $\phi_1(\lambda)$ ,  $\phi_2(\lambda)$  and  $\phi_3(\lambda)$  are not necessary for computing the interactions between current elements on the plate. For this reason  $\phi_1$ ,  $\phi_2$  and  $\phi_3$  are not presented explicitly.

Having completely specified the Hertz potential for the lower layer, it is now possible to use Equation 4.1 to obtain expressions for the electric field in the lower layer due to a horizontal electric dipole. Using Equation 4.3 in Equation 4.1 gives for Region n

$$E_{xx} = \frac{\partial}{\partial x} \left[ \frac{\partial \pi x n}{\partial x} + \frac{\partial \pi z n}{\partial z} \right] - \gamma_n^2 \pi x n \quad \text{Eq. 4.17}$$

$$E_{yx} = \frac{\partial}{\partial y} \left[ \frac{\partial \pi x n}{\partial x} + \frac{\partial \pi z n}{\partial z} \right] \quad \text{Eq. 4.18}$$

$$E_{zx} = \frac{\partial}{\partial z} \left[ \frac{\partial \pi x n}{\partial x} + \frac{\partial \pi z n}{\partial z} \right] - \gamma_n^2 \pi z n \quad \text{Eq. 4.19}$$

where, on the left hand side, the first subscript refers to the component of the field at the observation point and the second subscript gives the direction of the source dipole.

Substituting Equations 4.11 and 4.12 into Equation 4.6 (or Equation 4.7) and the result along with the last of Equations 4.14 into Equation 4.17 gives for the x-component in Region 2 (or Region 3)

$$E_{xx} = \frac{\partial}{\partial x} \left\{ \frac{\partial}{\partial x} \int_0^{\infty} \frac{c\lambda e^{\pm u_2 z}}{u_2} J_0(\lambda\rho) d\lambda + \frac{\partial}{\partial x} \int_0^{\infty} c\psi_5(\lambda) e^{-u_2 z} J_0(\lambda\rho) d\lambda \right. \\ \left. + \frac{\partial}{\partial z} \left[ \frac{cx}{\rho} \int_0^{\infty} \phi_5(\lambda) e^{-u_2 z} J_1(\lambda\rho) d\lambda \right] - \gamma_2^2 \int_0^{\infty} c\psi_5(\lambda) e^{-u_2 z} J_0(\lambda\rho) d\lambda \right\} \quad \text{Eq. 4.20}$$

Using the Sommerfeld integral (Wait and Fuller, 1971)

$$\frac{e^{-\gamma_n R}}{R} = \int_0^{\infty} \frac{\lambda}{u_n} e^{\pm u_n z} J_0(\lambda\rho) d\lambda, \quad \text{Eq. 4.21}$$

where  $R = (x^2 + y^2 + z^2)^{\frac{1}{2}}$  in Equation 4.20 and rearranging terms yields

$$E_{xx} = \left[ \frac{\partial^2}{\partial x^2} - \gamma_2^2 \right] c \frac{e^{-\gamma_2 R}}{R} + \left[ \frac{\partial^2}{\partial x^2} - \gamma_2^2 \right] \int_0^{\infty} c\psi_5(\lambda) e^{-u_2 z} J_0(\lambda\rho) d\lambda \\ + \frac{\partial}{\partial x \partial z} \left[ \frac{cx}{\rho} \int_0^{\infty} \phi_5(\lambda) e^{-u_2 z} J_1(\lambda\rho) d\lambda \right]. \quad \text{Eq. 4.22}$$

A similar treatment of Equation 4.18 gives for the y-component

$$E_{yx} = \frac{\partial^2}{\partial y \partial x} c \frac{e^{-\gamma_2 R}}{R} + \frac{\partial^2}{\partial y \partial x} \int_0^{\infty} c\psi_5(\lambda) e^{-u_2 z} J_0(\lambda\rho) d\lambda \\ + \frac{\partial^2}{\partial y \partial z} \left[ \frac{cx}{\rho} \int_0^{\infty} \phi_5(\lambda) e^{-u_2 z} J_1(\lambda\rho) d\lambda \right] \quad \text{Eq. 4.23}$$

and the z-component from Equation 4.19 is

$$E_{zx} = \frac{\partial^2}{\partial z \partial x} \frac{ce^{-\gamma_2 R}}{R} + \frac{\partial^2}{\partial z \partial x} \int_0^{\infty} c\psi_5(\lambda) e^{-u_2 z} J_0(\lambda\rho) d\lambda \\ + \left[ \frac{\partial^2}{\partial z^2} - \gamma_2^2 \right] \left[ \frac{cx}{\rho} \int_0^{\infty} \phi_5(\lambda) e^{-u_2 z} J_1(\lambda\rho) d\lambda \right] \quad \text{Eq. 4.24}$$

The initial terms of Equations 4.22 to 4.24 can now be recognized in column one of the matrix in Equation 3.11 as the primary parts of the Green's functions for an x-oriented dipole. The remaining terms are necessary to account for the proximity of the two conductivity interfaces. These remaining terms in each of Equations 4.22 to 4.24 will be referred to collectively as the secondary part of the appropriate Green's tensor element.

The partial differentiations in Equations 4.22 to 4.24 can be performed analytically, and the use of relations such as

$$\frac{\partial}{\partial x} J_0(\lambda\rho) = -\frac{\lambda x}{\rho} J_1(\lambda\rho)$$

$$\frac{\partial^2}{\partial x \partial y} J_0(\lambda\rho) = \frac{\lambda^2 xy}{\rho^2} J_2(\lambda\rho)$$

$$\frac{\partial^2}{\partial x^2} J_0(\lambda\rho) = \frac{\lambda^2 x^2}{\rho^2} J_2(\lambda\rho) - \frac{\lambda}{\rho} J_1(\lambda\rho)$$

$$\frac{\partial}{\partial x} \frac{J_1(\lambda\rho)}{\rho} = -\frac{\lambda x}{\rho^2} J_2(\lambda\rho)$$

and

$$J_2(\lambda\rho) = \frac{2}{\lambda\rho} J_1(\lambda\rho) - J_0(\lambda\rho)$$

as can be derived from Relation 9.1.30 of Abramowitz and Stegun (1968, p. 361) as well as the relation

$$u^2 = \lambda^2 + \gamma^2$$

yields from Equation 4.22

$$\begin{aligned} E_{xx} = & \left[ \frac{\partial^2}{\partial x^2} - \gamma^2 \right] \frac{c e^{-\gamma_2 R}}{R} \\ & + \int_0^\infty \left[ -c \left[ \frac{x^2 \lambda^2}{\rho^2} + \gamma_2^2 \right] \psi_5(\lambda) - \frac{u^2 \lambda x^2}{\rho^2} \phi_5(\lambda) \right] e^{-u_2 z} J_0(\lambda\rho) d\lambda \\ & + \int_0^\infty [c \lambda \psi_5(\lambda) + u_2 \phi_5(\lambda)] \left[ \frac{2x^2}{\rho^3} - \frac{1}{\rho} \right] e^{-u_2 z} J_1(\lambda\rho) d\lambda \end{aligned} \quad \text{Eq. 4.25}$$

In a like fashion, Equation 4.23 simplifies to

$$E_{yx} = \frac{\partial^2}{\partial y \partial x} \frac{ce^{-\gamma_2 R}}{R} - \frac{xy}{\rho^2} \int_0^{\infty} [c\lambda^2 \psi^5(\lambda) + u_2 \lambda \phi_5(\lambda)] e^{-u_2 z} J_0(\lambda \rho) d\lambda \\ + \frac{2xy}{\rho^3} \int_0^{\infty} [c\lambda \psi_5(\lambda) + u_2 \phi_5(\lambda)] e^{-u_2 z} J_1(\lambda \rho) d\lambda$$

Eq. 4.26

and Equation 4.24 reduces to

$$E_{zx} = \frac{\partial^2}{\partial x \partial z} \frac{ce^{-\gamma_2 R}}{R} + \frac{x}{\rho} \int_0^{\infty} [c\lambda u_2 \psi_5(\lambda) + \lambda^2 \phi_5(\lambda)] e^{-u_2 z} J_1(\lambda \rho) d\lambda$$

Eq. 4.27

The constant  $c$  carries with it the strength,  $I dx$ , of the electric dipole source. When this quantity  $I dx$  is set to unity, the right hand sides of Equations 4.25 to 4.27 give the first column of the generalized Green's tensor.

The second column is obtained by repeating the argument of this section, beginning instead with a  $y$ -oriented electric dipole. The results can be inferred from Equations 4.25 to 4.27 by interchanging the independent variables  $x$  and  $y$ . This leads to

$$E_{xy} = \frac{\partial^2}{\partial x \partial y} \frac{ce^{-\gamma_2 R}}{R} - \frac{xy}{\rho^2} \int_0^{\infty} [c\lambda^2 \psi_5(\lambda) + u_2 \lambda \phi_5(\lambda)] e^{-u_2 z} J_0(\lambda \rho) d\lambda \\ + \frac{2xy}{\rho^3} \int_0^{\infty} [c\lambda \psi_5(\lambda) + u_2 \phi_5(\lambda)] e^{-u_2 z} J_1(\lambda \rho) d\lambda$$

Eq. 4.28

$$E_{yy} = \left[ \frac{\partial^2}{\partial y^2} - \gamma^2 \right] \frac{ce^{-\gamma_2 R}}{R} + \int_0^{\infty} \left[ -c \left[ \frac{y^2 \lambda^2}{\rho^2} + \gamma_2^2 \right] \psi_5(\lambda) - \frac{u \lambda y^2}{\rho^2} \phi_5(\lambda) \right] \times \\ e^{-u_2 z} J_0(\lambda \rho) d\lambda \\ + \int_0^{\infty} [c\lambda \psi_5(\lambda) + u_2 \phi_5(\lambda)] \left[ \frac{2y^2}{\rho^3} - \frac{1}{\rho} \right] e^{-u_2 z} J_1(\lambda \rho) d\lambda$$

Eq. 4.29

and

$$E_{zy} = \frac{\partial^2}{\partial z \partial y} \frac{ce^{-\gamma_2 R}}{R} - \frac{y}{\rho} \int_0^{\infty} [c\lambda u_2 \psi_5(\lambda) + \lambda^2 \phi_5(\lambda)] e^{-u_2 z} J_1(\lambda \rho) d\lambda$$

Eq. 4.30

The first term on the right of these equations can be recognized in column two of the matrix in Equation 3.11.

The third column of the generalized tensor requires special consideration and is the subject of the next section.

#### 4.3 A Vertical Electric Dipole in the Lower Layer of a Two-Layer Earth

To establish the third column, it is necessary to consider a vertical electric dipole as depicted in Figure 4-2. The source location, the coordinate system, the locations of the interfaces, and the physical properties assigned to each region are as in Section 4.2. Only the dipole orientation has changed.

The fields are again computed from the Hertz potential through Equations 4.1 and 4.2. But in this case radial symmetry allows us to calculate the fields from a vector potential having a single vertical component. It is shown in Appendix C that the potential in the four regions is given by

$$\text{in air} \quad \pi_{z_0} = c \int_0^{\infty} \psi_1(\lambda) e^{u_0 z} J_0(\lambda \rho) d\lambda \quad \text{Eq. 4.31}$$

$$\text{in Region 1} \quad \pi_{z_1} = c \int_0^{\infty} [\psi_3(\lambda) e^{u_1 z} + \psi_4(\lambda) e^{-u_1 z}] J_0(\lambda \rho) d\lambda \quad \text{Eq. 4.32}$$

$$\text{in Region 2} \quad \pi_{z_2} = c \int_0^{\infty} [\psi_5(\lambda) e^{u_2 z} + \psi_6(\lambda) e^{-u_2 z}] J_0(\lambda \rho) d\lambda \quad \text{Eq. 4.33}$$

$$\text{in Region 3} \quad \pi_{z_3} = c \int_0^{\infty} [\psi_5(\lambda) e^{-u_2 z} + \psi_6(\lambda) e^{-u_2 z}] J_0(\lambda \rho) d\lambda \quad \text{Eq. 4.34}$$

where

$$\psi_1(\lambda) = 4\kappa_1 \kappa_2 u_1 \lambda e^{u_0(h+d) - u_1 d - u_2 h} / \text{DEN}$$

$$\psi_3(\lambda) = 2\kappa_2 \lambda (\kappa_0 u_1 + \kappa_1 u_0) e^{(u_1 - u_2) h} / \text{DEN}$$

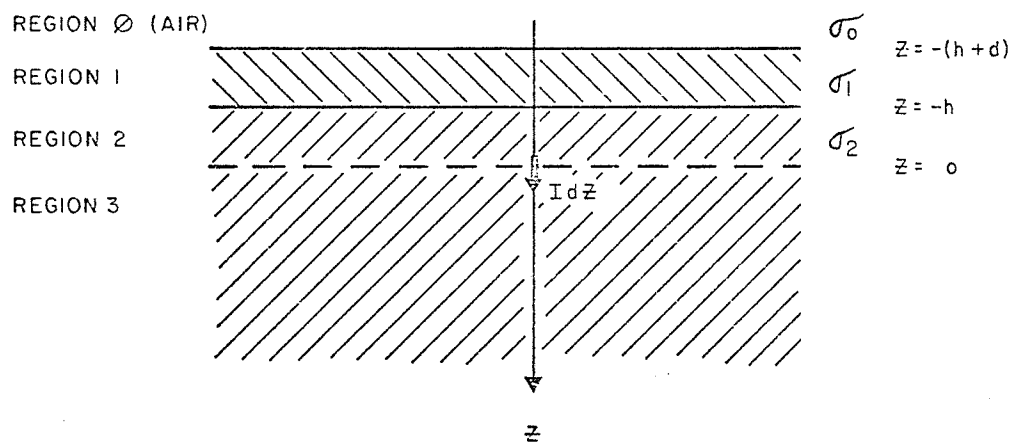


Figure 4-2 Vertical Electric Dipole in a Two-Layer Earth



$$\psi_4(\lambda) = 2\kappa_2 \lambda (\kappa_0 u_1 - \kappa_1 u_0) e^{u_1(h+2d)} u_2 h \quad /DEN$$

$$\psi_5(\lambda) = \lambda / u_2 \quad \text{Eq. 4.35}$$

$$\psi_6(\lambda) = \frac{\lambda}{u_2} [\kappa_0 \kappa_1 u_1 u_2 + \kappa_1 \kappa_1 u_0 u_2 - \kappa_0 \kappa_2 u_1 u_1 - \kappa_2 \kappa_1 u_0 u_1 + (\kappa_0 \kappa_1 u_1 u_2 - \kappa_1 \kappa_1 u_0 u_2 + \kappa_0 \kappa_2 u_1 u_1 - \kappa_2 \kappa_1 u_0 u_1) e^{-2u_1 d}] e^{-2u_2 h} /DEN$$

$$\text{Eq. 4.36}$$

where

$$DEN = (\kappa_0 \kappa_1 u_1 u_2 + \kappa_1 \kappa_1 u_0 u_2 + \kappa_0 \kappa_2 u_1 u_1 + \kappa_2 \kappa_1 u_0 u_1) + (\kappa_0 \kappa_1 u_1 u_2 - \kappa_1 \kappa_1 u_0 u_2 - \kappa_0 \kappa_2 u_1 u_1 - \kappa_2 \kappa_1 u_0 u_1) e^{-2u_1 d}$$

For a vertical vector potential  $\pi_{zn}$ , the electric field as specified by Equation 4.1 is

$$E_{xz} = \frac{\partial^2}{\partial x \partial z} \pi_{zn}$$

$$E_{yz} = \frac{\partial^2}{\partial y \partial z} \pi_{zn}$$

$$E_{zz} = \left( \frac{\partial^2}{\partial z^2} - \gamma_n^2 \right) \pi_{zn} \quad \text{Eqs. 4.37}$$

where the double subscript on the left hand side refers to the field component and the source orientation as before. Equation 4.33 or 4.34 can be substituted into Equations 4.37, remembering Equation 4.21 and the fact that  $u_2^2 = \lambda^2 + \gamma_2^2$ , to obtain

$$E_{xz} = \frac{\partial^2}{\partial x \partial z} \frac{c e^{-\gamma_2 R}}{R} + \frac{x c}{\rho} \int_0^{\infty} u_2 \lambda \psi_6(\lambda) e^{-u_2 z} J_1(\lambda \rho) d\lambda \quad \text{Eq. 4.38}$$

$$E_{yz} = \frac{\partial^2}{\partial y \partial z} \frac{c e^{-\gamma_2 R}}{R} + \frac{y c}{\rho} \int_0^{\infty} u_2 \lambda \psi_6(\lambda) e^{-u_2 z} J_1(\lambda \rho) d\lambda \quad \text{Eq. 4.39}$$

$$E_{zz} = \left( \frac{\partial^2}{\partial z^2} - \gamma_2^2 \right) \frac{c e^{-\gamma_2 R}}{R} + \int_0^{\infty} \lambda^2 c \psi_6(\lambda) e^{-u_2 z} J_0(\lambda \rho) d\lambda \quad \text{Eq. 4.40}$$

The first term on the right of Equations 4.38 to 4.40 can be found in the third column of the matrix in Equation 3.11.

In summary, it is now clear that the electric field

Green's tensor for an electric dipole source in infinite space, as described by Equation 3.11, can be generalized to the case of a dipole in a two-layer earth by constructing column one from the right hand sides of Equations 4.25 to 4.27, column two from the right hand sides of Equations 4.28 to 4.30, and column three from the right hand sides of Equations 4.38 to 4.40.

One further generalization is necessary: we require the fields about a distributed source rather than a point dipole. However, since all terms generated by the inclusion of the boundaries can be shown to be non-singular when the source point and observation point coincide, no additional mathematical problems arise. Standard quadrature methods can be used for the spatial integration over the volume of the scatterer.

## CHAPTER V

### CALCULATION OF INCIDENT FIELDS AND SECONDARY FIELDS PERTINENT TO THE HORIZONTAL LOOP PROSPECTING SYSTEM

#### 5.1 Introduction

Chapters II to IV dealt with a method which could be used to compute the electromagnetic response of a tabular conducting scatterer in a two-layer earth to an arbitrary EM prospecting system. The subsequent discussion particularizes this procedure to obtain the response of a vertical thin tabular conductor in a two-layer earth to the horizontal loop prospecting system.

Having established the elements of the Green's tensor  $G(\underline{r}|\underline{r}_s)$  in Equation 2.6, it remains to develop an expression for the incident electric field generated by the transmitter, before the integral equation is completely specified. It remains also to specify more explicitly the means (Equation 2.11) for obtaining the primary and secondary magnetic fields at the receiver location. These two final theoretical problems are the subjects of this chapter and the developments which borrow heavily from Keller and Frischknecht (1970) and Wait (1951)

go no further than is necessary for the computation of horizontal loop anomalies.

### 5.2 Vertical Magnetic Dipole above a Two-Layer Earth

The transmitter for the horizontal loop system is a horizontal current loop (vertical magnetic dipole), held at waist height, which generates an electric field having horizontal circular flow lines in a stratified earth.

Figure 5-1 depicts a vertical magnetic dipole over a two-layer earth. The dipole is at the origin of the coordinate system. The horizontal boundaries occur at  $z=h$  (air/earth) and at  $z=h+d$  (upper layer/lower layer) and the regions are distinguished by conductivities  $\sigma_0$ ,  $\sigma_1$  and  $\sigma_2$ . Free space values are taken for the dielectric constant and magnetic permeability.

It is assumed that the solution can be expressed in terms of the magnetic Hertz potential  $\pi^*$  (Ward, 1967, p. 17) which has only a  $z$ -component, and from which the fields can be generated through

$$\vec{E} = -i\omega\mu\vec{\nabla}\times\pi^* \quad \text{Eq.5.1}$$

and

$$\vec{H} = -\gamma^2\pi^*\vec{z} + \vec{\nabla}\nabla\cdot\pi^*\vec{z} \quad \text{Eq.5.2}$$

where, as before,  $\gamma$  is the propagation constant.

The magnetic Hertz potential satisfies the wave equation, the general solution of which is given by Equation B6 in Appendix B. Continuous symmetry with respect to  $\theta$  requires that  $n=0$  in Equation B6 and for the four regions it can be said:

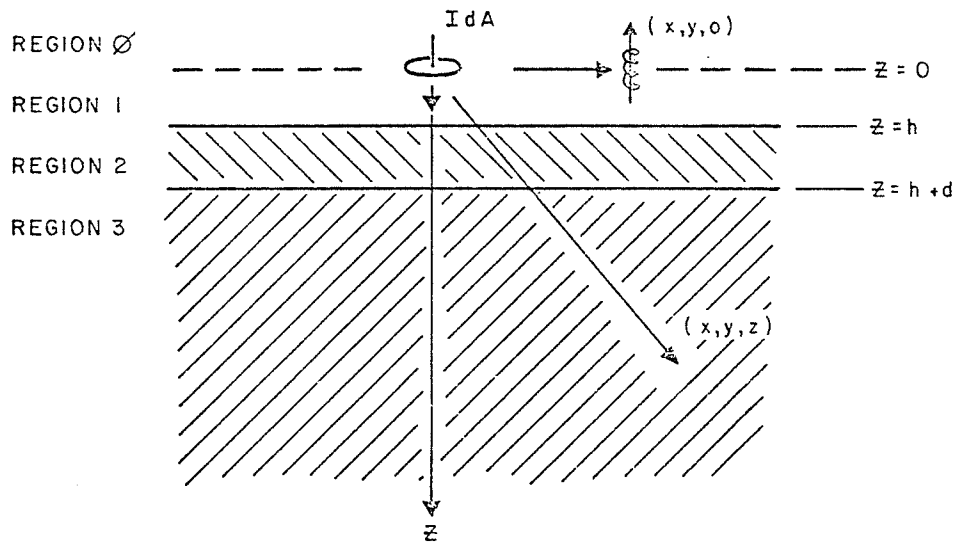


Figure 5-1 Vertical Magnetic Dipole above a Two-Layer Earth

in air above the dipole (Region 0)

$$\pi_{Z_0}^* = \int_0^{\infty} [\xi_1(\lambda) e^{u_0 z} + \xi_2(\lambda) e^{-u_0 z}] J_0(\lambda \rho) d\lambda \quad \text{Eq. 5.3}$$

in air below the dipole (Region 1)

$$\pi_{Z_1}^* = \int_0^{\infty} [\xi_3(\lambda) e^{-u_1 z} + \xi_4(\lambda) e^{u_1 z}] J_0(\lambda \rho) d\lambda \quad \text{Eq. 5.4}$$

in the upper earth layer

$$\pi_{Z_2}^* = \int_0^{\infty} [\xi_5(\lambda) e^{-u_2 z} + \xi_6(\lambda) e^{u_2 z}] J_0(\lambda \rho) d\lambda \quad \text{Eq. 5.5}$$

and in the lower layer

$$\pi_{Z_2}^* = \int_0^{\infty} [\xi_5(\lambda) e^{-u_2 z} + \xi_6(\lambda) e^{u_2 z}] J_0(\lambda \rho) d\lambda \quad \text{Eq. 5.6}$$

where  $\xi$  instead of  $\psi$  represents the eigenfunctions to avoid confusion with the earlier usage in Chapter IV.

There can be no upward travelling wave in the lower layer so that  $\xi_6(\lambda) = 0$ . Furthermore, the term containing  $\xi_1(\lambda)$  must depict the primary potential in air so that we must have

$$\int_0^{\infty} \xi_1(\lambda) e^{\pm u_0 z} J_0(\lambda \rho) d\lambda = \frac{IdA}{4\pi} \frac{e^{-\gamma_0 R}}{R}$$

where  $R$  is the distance between the source point and the observation point. Recalling the Sommerfeld integral, Equation B5 this requires

$$\xi_1(\lambda) = \frac{IdA}{4\pi} \frac{\lambda}{u_0} \quad \text{Eq. 5.7}$$

The remaining eigenfunctions,  $\xi_2$ ,  $\xi_3$ ,  $\xi_4$  and  $\xi_5$ , are obtained by insisting on the continuity of the tangential fields at the boundaries of the medium. From Equations 5.1 and 5.2, the tangential fields are

$$E_{\phi} = i\omega\mu \frac{\partial \pi^*}{\partial \rho} \quad \text{and} \quad H_r = \frac{\partial^2 \pi^*}{\partial \rho \partial z}$$

Equating the tangential field components at  $z=h$  and  $z=h+d$  and integrating over  $\rho$  (the integration constant must be zero for the potentials to vanish at infinity) yields

$$\pi_{z_0}^* = \pi_{z_1}^* \quad \text{Eq. 5.8}$$

and

$$\frac{\partial \pi_{z_0}^*}{\partial z} = \frac{\partial \pi_{z_1}^*}{\partial z} \quad \text{Eq. 5.9}$$

at  $z=h$ , and

$$\pi_{z_1}^* = \pi_{z_2}^* \quad \text{Eq. 5.10}$$

and

$$\frac{\partial \pi_{z_1}^*}{\partial z} = \frac{\partial \pi_{z_2}^*}{\partial z} \quad \text{Eq. 5.11}$$

at  $z=h+d$ . Substituting Equations 5.4 to 5.7 into Equations 5.8 to 5.11 yields a set of simultaneous equations (Equation 5.12 in matrix form) for the remaining eigenfunctions.

$$\begin{bmatrix} e^{u_0 h} & -e^{-u_1 h} & -e^{u_1 h} & 0 \\ 0 & e^{-u_1(h+d)} & e^{u_1(h+d)} & -e^{-u_2(h+d)} \\ u_0 e^{u_0 h} & u_1 e^{-u_1 h} & -u_1 e^{u_1 h} & 0 \\ 0 & -u_1 e^{-u_1(h+d)} & u_1 e^{u_1(h+d)} & u_2 e^{-u_2(h+d)} \end{bmatrix} \begin{bmatrix} \xi_2(\lambda) \\ \xi_3(\lambda) \\ \xi_4(\lambda) \\ \xi_5(\lambda) \end{bmatrix} = \begin{bmatrix} \frac{-IdA}{4\pi} \frac{\lambda}{u_0} e^{-u_0 h} \\ 0 \\ \frac{-IdA}{4\pi} \lambda e^{-u_0 h} \\ 0 \end{bmatrix} \quad \text{Eq. 5.12}$$

The incident electric field at the plate, due to the vertical magnetic dipole above the earth, can now be obtained by substituting Equation 5.6 (recalling  $\xi_6 = 0$ ) into Equation 5.1 to give

$$E_x^i = -i\omega\mu \frac{y}{\rho} \int_0^{\infty} \xi_5(\lambda) e^{-u_2 z} J_1(\lambda \rho) \lambda d\lambda$$

$$E_y^i = i\omega\mu \frac{x}{\rho} \int_0^{\infty} \xi_5(\lambda) e^{-u_2 z} J_1(\lambda \rho) \lambda d\lambda$$

$$E_z^i = 0 .$$

Eq.5.14

Equation 5.12 can be used to obtain

$$\xi_5(\lambda) = \frac{IdA}{4\pi} \frac{\lambda u_1 e^{-u_0 h - u_1 d + u_2(h+d)}}{[u_1 u_2 + u_1 u_1 + u_0 u_2 + u_0 u_1 + (u_1 u_2 - u_1 u_1 - u_0 u_2 + u_0 u_1) e^{-u_1 d}]}$$

The primary magnetic field (including the layered half-space response) at the receiver location,  $z=0$  and  $\rho>0$ , is obtained by substituting Equation 5.3 into Equation 5.2 to yield

$$\begin{aligned} H_z^P &= \frac{IdA}{4\pi} (-\gamma_0^2 + \frac{\partial^2}{\partial z^2}) \frac{e^{-\gamma_0 R}}{R} + \frac{IdA}{4\pi} (\frac{\partial^2}{\partial z^2} - \gamma_0^2) \int_0^\infty \xi_2(\lambda) e^{u_0 z} J_0(\lambda \rho) d\lambda \\ &= \frac{IdA}{4\pi} \left\{ \frac{e^{-\gamma_0 R}}{R} \left[ \frac{1}{R} (-\gamma_0^2 - \frac{1}{R}) - \gamma_0^2 \right] + \int_0^\infty \lambda^2 \xi_2(\lambda) J_0(\lambda \rho) d\lambda \right\} \end{aligned}$$

where from Equation 5.12

$$\xi_2(\lambda) = \frac{IdA}{4\pi} \frac{\lambda [u_1 u_2 + u_1 u_1 - u_0 u_2 - u_0 u_1 + (u_1 u_2 - u_1 u_1 + u_0 u_2 - u_0 u_1) e^{-2u_1 d}] e^{-2u_0 h}}{u_0 [-u_1 u_2 - u_1 u_1 - u_0 u_2 - u_0 u_1 + (-u_1 u_2 + u_1 u_1 + u_0 u_2 - u_0 u_1) e^{-2u_1 d}]}$$

Eq.5.15

### 5.3 The Secondary Magnetic Field at the Receiver Location due to the Eddy Currents in the Plate

Consider an electric dipole at the origin in the lower layer of a two-layer earth radiating a magnetic field to a receiver location  $(x, y, z)$  in the upper (air) region. For a horizontal  $x$ -directed electric dipole, the Hertz potential in the upper layer is given by

$$\pi_{x_0}^h = \pi_{x_0}^h \hat{i} + \pi_{x_0}^h \hat{k} \quad \text{Eq.5.16}$$

where  $\pi_{x_0}^h$  is given by the right hand side of Equation 4.4 and

$\pi_{z_0}^h$  is given by the first of Equations 4.14.

The horizontal loop receiver measures only the vertical component of the magnetic field. Vertical current dipoles, generating only horizontal magnetic fields in horizontally stratified media can therefore be ignored



as can the vertical component,  $\pi_{z0}^h$ , of the Hertz potential in Equation 5.16. The vertical magnetic field above the surface due to the x-directed current element at a point  $r = (0, 0, 0)$  on the plate is given, via Equation 4.2, by

$$H_{zx} = \frac{-\kappa_0 \partial \pi_{x0}^h}{\partial y} \quad \text{Eq. 5.18}$$

$$= \kappa_0 c \frac{y}{\rho} \int_0^{\infty} \psi_1(\lambda) e^{u_0 z} J_1(\lambda \rho) \lambda d\lambda \quad \text{Eq. 5.19}$$

where use has been made of Equation 4.4, and  $\psi_1(\lambda)$  is given by Equation 4.8. For y-directed current elements, the vertical magnetic field in the upper layer is, by similar argument,

$$H_{zy} = -\kappa_0 c \frac{x}{\rho} \int_0^{\infty} \psi_1(\lambda) e^{u_0 z} J_1(\lambda \rho) \lambda d\lambda \quad \text{Eq. 5.20}$$

The magnetic field due to a volume distribution of current can be obtained by summing the contributions from all source points, and the summation is represented by the integral in Equation 2.11.

## CHAPTER VI

### A DESCRIPTION OF THE ALGORITHM

#### 6.1 Introduction

Having eliminated the physical and mathematical problems generated by the strategy chosen in Chapter II, the algorithm used to affect a solution can now be discussed.

The solution to the problem as described by Figure 1-1 is subject to a number of limitations: the plate must be rectangular and vertical, it must be inductively thin (that is, the thickness must be much less than the skin depth of the scatterer), and the top edge of the plate must be horizontal and beneath the rock/overburden interface. Furthermore, the source must irradiate the plate with an incident field which is symmetrical across the x-z plane (Section 6.3).

In spite of these restrictions, a number of important parameters remain free. They include the operating frequency, all conductivities (even though  $\sigma_0$  is always zero for this work), coil height, and all linear dimensions provided they do not violate the limitations in the preceding paragraph.

## 6.2 Application of the Point Collocation Method

The Point Collocation Method, described and demonstrated in Section 2.3, requires the application of the integral equation at several unique points, called match points or collocation points. In number, they usually equal the number of test functions in order that a square matrix will develop. In the present case, the match points are half as numerous as the test functions because two polynomial surfaces are being generated to approximate the two dimensional vector field of the solution.

The locations of the match points are somewhat arbitrary and variations may lead to better or worse solutions. Herein, a rectangular array was chosen, and is shown in relation to the coordinate system in Figure 6-1. The number of points in the y-direction compared with the number of points in the z-direction is normally chosen with some regard for the shape (length/width) of the plate. Based on the match point locations, the plate is subdivided into a number of rectangular patches which provide the basis for evaluating the integrals over the plate.

The integrals of Equation 2.10 are evaluated by integrating patch-by-patch over the entire plate. Some advantage lies in this patchwise summing because the Gaussian quadrature order can be increased for patches near the match point where the integrand becomes unpolynomic. Further advantage is taken of the fact that for a given test function , integrals

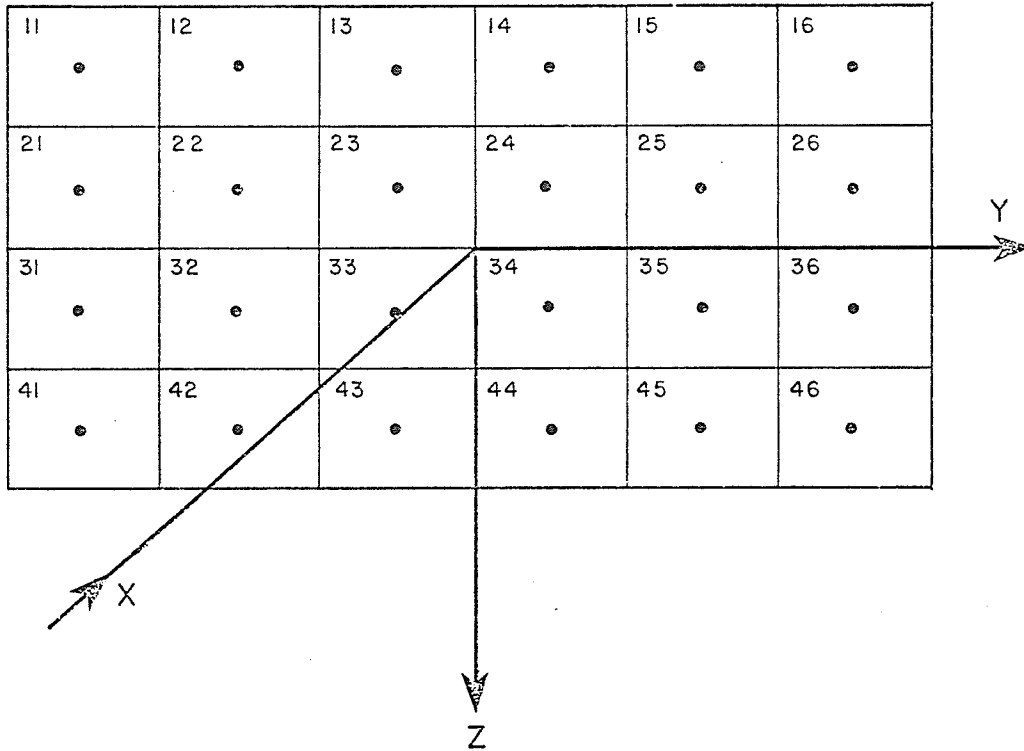


Figure 6-1 Match Points and the Subdivision of the Plate into Patches

may be the same (or different by a sign, depending on the parity of the integrand) for groups of match points located symmetrically about the axes. One such group, for integrands involving primary Green's functions, would be those designated 12, 15, 42 and 45 in Figure 6-1. For secondary Green's functions, pairs can be established by symmetry in the  $y=0$  plane but not in the  $z=0$  plane because the coupling with the surface depends on depth.

### 6.3 Test Functions

Reducing an integral equation or partial differential equation to a matrix equation for the purpose of determining the coefficients of a linear combination of test functions is a common line of attack, when the formulating equation cannot be solved exactly. While choosing a strategy for setting up the matrix equation is probably the single most important decision in solving problems of this nature, it should not be overlooked that a judicious choice of test functions can considerably reduce the numerical effort in acquiring a solution of given accuracy (McDonald, et al., 1974).

To reduce computing costs, it was decided that considerable value could be obtained from solutions having symmetry across the  $y=0$  plane. This loss of generality requires that the plate must be irradiated with a symmetric incident field, but also means that only half as many test functions are required. In this case the expected scatter current on the plate is such that the  $y$ -component is symmetric (in the  $y=0$  plane)

and the z-component is antisymmetric. Thus for the polynomial surface simulating the y-component of the solution vector, only even functions of y need appear. For the surface simulating the z-component, only odd functions of y appear. There being no symmetry in the z=0 plane, both even and odd functions of z are used in simulating the two surfaces.

Simple two-variable polynomials of the form  $y^n z^m$  were initially used as test functions. Although the phase and general form of the plate current were intuitively satisfying over a wide range of plate conductivities, wild increases in the current strength near the plate edges seriously detracted from the usefulness of the solution. West (1979) argued that since the plate is thin, current entering the plate perpendicular to the edges would be negligible compared to the amount of current entering the plate through the large surfaces. This implies an 'almost' homogeneous Dirichlet boundary condition (Harrington, 1964) for the y-component of the current at the vertical plate boundaries, as well as for the z-component of the current at the horizontal plate edges. This led to a revision of the trial functions so as to yield a solution which obeys these boundary conditions naturally. The components of the field were simulated using

$$\begin{aligned}
 E_y(y, z) &= \sum_{I=1}^N a_I \left[ 1 - \left( \frac{y}{S_2} \right)^{N^{ev}+2} \right] z^M \\
 E_z(y, z) &= \sum_{I=1}^N b_I y^{N^{od}} \left[ K(z) - \left( \frac{z}{W_2} \right)^{M+2} \right]
 \end{aligned}
 \tag{Eqs. 6.1}$$

where

$$K(z) = \begin{cases} 1 & ; M \text{ even} \\ z/W_2 & ; M \text{ odd} \end{cases}$$

and where  $S_2 = S/2$  and  $W_2 = W/2$ .  $S$  and  $W$  are plate strike-length and width respectively. The exponents were chosen so as to create a linear sequence of functions using the algorithm

$$M = (I-1)/N_2$$

$$N^{ev} = (I-1-(I-1)/N_2 * N_2) * 2$$

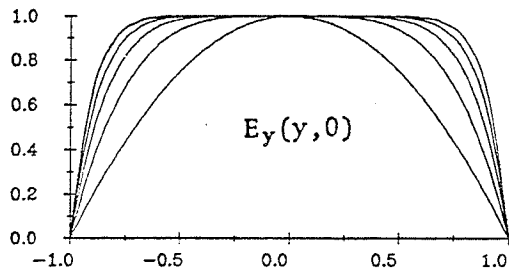
$$N^{od} = N^{ev} + 1$$

where  $I=1,2,3,\dots, N$  and  $N$  is the number of match points.

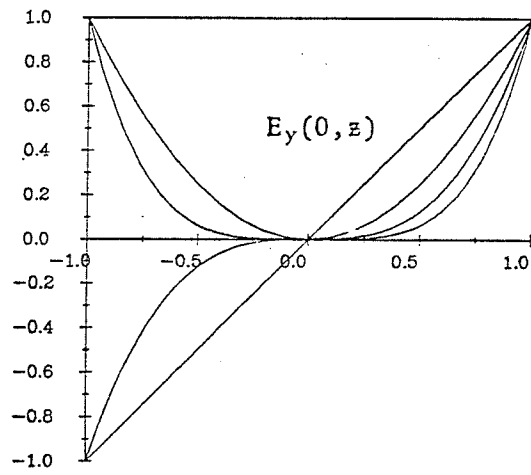
Figure 6-2a and b illustrate the  $y$ -variation of  $E_y$  and the  $z$ -variation of  $E_y$  in Equations 6.1. Figures 6-2c and 6-2d illustrate the  $y$ -variation of  $E_z$  and the  $z$ -variation of  $E_z$  respectively. Because symmetry halves the number of test functions, only the match points on the left half of the plate in Figure 6-1 are used and  $N_2$  in the algorithm refers to the number of match points in the  $y$ -direction. "/" and "\*" refer to integer division and multiplication as defined in FORTRAN.

These new test functions pose no problems for integrals over regions remote from a match point. When the match point is inside the region of integration, additional manipulation is necessary. Consider again a cube-shaped region centered about match point  $r_1$ . Using the new trial functions for the  $y$ -component of the solution, Equation 3.26a, for example, can be shown to be

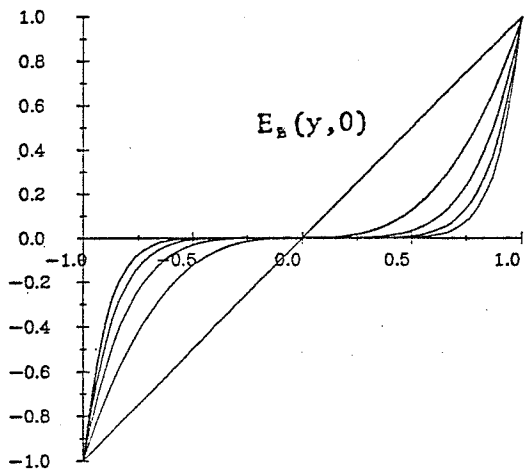
$$I_{SING} = \int_{CUBE} G_{YY}(r_1 | r_s) (z_s + z_1)^m dv_s - \frac{1}{S_2^{ne}} \int_{CUBE} G_{YY}(r_1 | r_s) (y_s + y_1)^{ne} (z_s + z_1)^m dv_s \quad \text{Eq. 6.2}$$



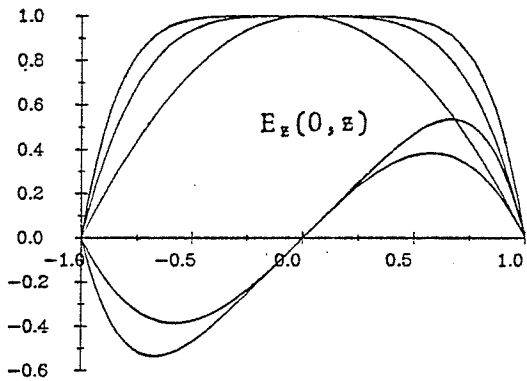
a. y-variation of the y-component



b. z-variation of the y-component



c. y-variation of the z-component



d. z-variation of the z-component

Figure 6-2 Test Functions



For the z-component of the solution Equation 3.26a becomes

$$I_{\text{SING}} = -\frac{1}{W_2^m} \int_{\text{CUBE}} G_{YY}(\underline{r}_1 | \underline{r}_s) (y_s + y_1)^{n_o} (z_s + z_1)^m dV_s$$

$$+ \begin{cases} \int_{\text{CUBE}} G_{YY}(\underline{r}_1 | \underline{r}_s) \frac{(z_s + z_1)(y_s + y_1)^{n_o} dV_s}{W_2} ; m \text{ odd} \\ \int_{\text{CUBE}} G_{YY}(\underline{r}_1 | \underline{r}_s) (y_s + y_1)^{n_o} dV_s ; m \text{ even} \end{cases} \text{ Eq. 6.3}$$

where  $n_e = N^{\text{ev}} + 2$ ,  $n_o = N^{\text{od}}$  and  $m = M + 2$ .

Applying Newton's expansion formula to the binomials converts Equation 6.2 into

$$I_{\text{SING}} = \sum_{k=1}^{m+1} \frac{m! z_1^{m-k+1}}{(m-k+1)!(k-1)!} \int_{\text{CUBE}} G_{YY}(\underline{r}_1 | \underline{r}_s) z^{k-1} dV_s$$

$$- \frac{1}{s_2^2} \sum_{j=1}^{n+1} \frac{n! y_1^{n-j+1}}{(n-j+1)!(j-1)!} \sum_{k=1}^{m+1} \frac{m! z_1^{m-k+1}}{(m-k+1)!(k-1)!} \int_{\text{CUBE}} G_{YY}(\underline{r}_1 | \underline{r}_s) y_s^{j-1} z_s^{k-1} dV_s$$

and Equation 6.3 into

Eq. 6.4

$$I_{\text{SING}} = \frac{1}{W_2^m} \sum_{j=1}^{n_o+1} \frac{n_o! y_1^{n_o-j+1}}{(n_o-j+1)!(j-1)!} \sum_{k=1}^{m+1} \frac{m! z_1^{m-k+1}}{(m-k+1)!(k-1)!}$$

$$\int_{\text{CUBE}} G_{YY}(\underline{r}_1 | \underline{r}_s) y_s^{j-1} z_s^{k-1} dV_s$$

$$+ \begin{cases} \frac{1}{W_2} \sum_{j=1}^{n_o+1} \frac{n_o! y_1^{n_o-j+1}}{(n_o-j+1)!(j-1)!} \left[ z_1 \int_{\text{CUBE}} G_{YY}(\underline{r}_1 | \underline{r}_s) y_s^{j-1} dV_s \right. \\ \left. + \int_{\text{CUBE}} G_{YY}(\underline{r}_1 | \underline{r}_s) y_s^{j-1} z_s dV_s \right]; m \text{ odd} \\ \sum_{j=1}^{n_o+1} \frac{n_o! y_1^{n_o-j+1}}{(n_o-j+1)!(j-1)!} \int_{\text{CUBE}} G_{YY}(\underline{r}_1 | \underline{r}_s) y_s^{j-1} dV_s; m \text{ even} \end{cases} \text{ Eq. 6.5}$$

All integrals are now of the form discussed in Sections 3.6 and 3.7. It is noted, for use in the next section, that Equa-

tions 6.4 and 6.5 are also true when the region of integration is an entire singular patch.

#### 6.4 Integration of Terms Involving $G_{yz}^P$ Over Regions Containing a Match Point

Singular patches (regions containing a match point) require special attention because of the unpolynomic nature of the integrand at the centre of the patch. For integrands  $G_{yy}^P y_s^0 z_s^0$  the limits of integration are shown for one quadrant of a singular patch in Figure 6-3 where  $\Delta y_2$  is half the patch length and  $\Delta z_2$  is half the patch height. The rectangular region beneath  $z = -T/2$  is one quarter of a square cylinder and is handled using the method described in the initial part of Section 3.7, while the final paragraph of Section 3.7 describes the method used for the other regions. In all cases tested, eighteenth order Gaussian quadrature causes the line integrals to converge to more than seven figures of accuracy. Integrals of terms  $G_{yz}^P y_s^0 z_s^0$  are zero because  $G_{yz}$  is an odd function.

For integrands of the form  $G_{yy}^P y_s^n z_s^m$  or  $G_{yz}^P y_s^n z_s^m$ , the singular patch is subdivided as shown in Figure 6-4. Over the cube centred at the match point, integration is performed using a method described in Section 3.6. For the other regions, which double in size progressing away from the central cube, tenth order Gauss quadrature is used.

Having integrated functions like  $G_{yy}^P y_s^n z_s^m$  and  $G_{zy}^P y_s^n z_s^m$  for all values of  $n$  and  $m$  over the entire singular patch, the

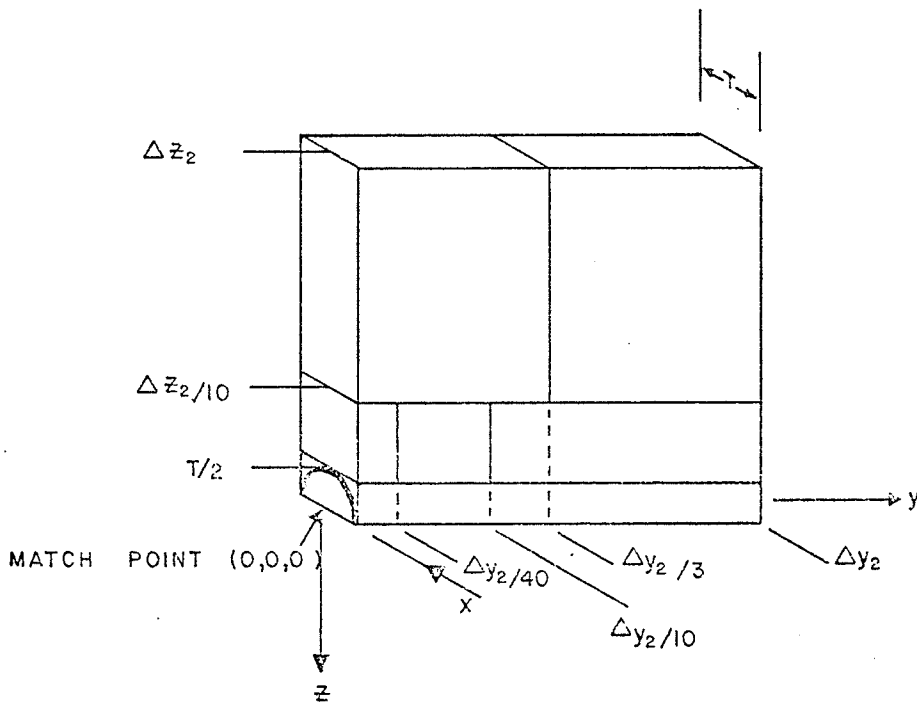


Figure 6-3 Subdivision of One Quadrant of a Singular Patch for Integration  $G^P_{y^0 z^0}$

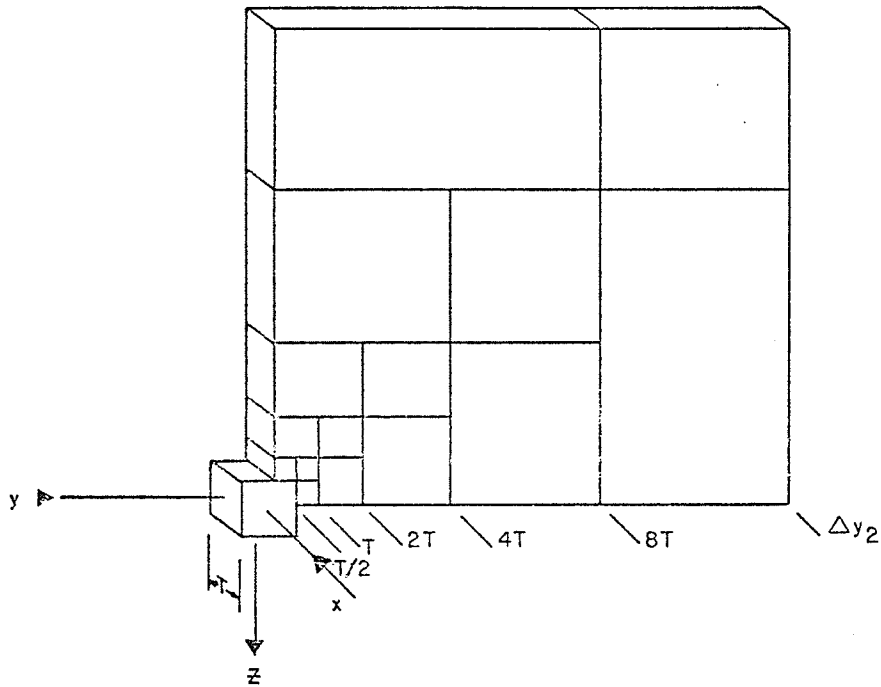


Figure 6-4 Subdivision of One Quadrant of a Singular Patch for Integration of  $G^P y^n z^m$

integrals involving the actual test functions can be constructed using the summations given in Equations 6.4 and 6.5.

### 6.5 Integration of Terms Involving $G^P$ over Remote Regions

When the match point lies outside the patch being integrated, none of the Green's functions are singular and Gauss quadrature is applied over the entire patch without any subdivision. It appears that fourth order quadrature is adequate for the y- and z- integration, while second order quadrature suffices to make the x-integrals converge. Some adjustment of the quadrature orders is built into the program for plate shapes and match point arrays that yield patches with a length much different from their width.

It is lamentable that not all quadrature is guaranteed to converge and that integration limits and quadrature orders are chosen in so arbitrary a fashion. However, in the solution of integral equations, integration is so extensive that to check each one might double or triple the already lengthy execution times.

### 6.6 Hankel Transforms and the Spatial Integration of Terms Involving $G^S$

Chapter IV gives expressions for the secondary parts of the Green's function which, without exception, require an integration from zero to infinity. The functions to be integrated are the product of a Bessel function and a kernel

function which, in geophysical literature, generally refers to everything else in the integrand. The integrands are oscillatory because of the Bessel function, and the oscillations are damped out for increasing values of the integration variable, at a rate governed mainly by the kernel function.

Traditionally, such integrals have been handled with a method described by Longman (1956), wherein the region of integration is subdivided by the zeros of the Bessel function. Integrating over the subregions creates an alternating series, the convergence of which can be accelerated using Euler's transformation.

More recently, digital filtering techniques (first reported by Ghosh, 1971) to evaluate Hankel transform integrals have become popular, and for good reason. The method, which uses numerical convolution with predetermined filter coefficients, avoids completely the evaluation of the Bessel function and appears to be about an order of magnitude faster than the traditional method.

In this work, Hankel transforms were initially handled using the method described by Longman (1956) but this method was abandoned in favour of the digital filtering method following the publication by Anderson (1979) of a computer program (ZHANKS) for applying the filter method. Comparison of the two methods was undertaken to ensure consistent results for a wide range of transforms encountered in the present work; the agreement was never worse than four significant figures and was frequently much better.

Having thus obtained values for any of the secondary Green's functions for any source point - observation point configuration, the spatial integration of the terms over any patch was executed using Gaussian quadrature. Second order quadrature in the y- and z- directions and first order in the x-direction was used for all patches regardless of the match point location, and appears to be adequate.

In a straightforward application of the point collocation method, there will be considerable redundancy in the computation of the Hankel transforms. Considering, for example, match point (observation point) 13 in Figure 6-1, there will be Gaussian quadrature nodes (source points) in patch 14 which will have corresponding points in patch 12 that yield for match point 13 the same value for the secondary Green's function. A sign change may be involved as well. The computer program which generated the results in Chapter VII avoids this redundancy by computing in advance the values of all the secondary Green's functions for all source point - observation point combinations. Integrating functions like  $G_{YZ}^S [1 - (\frac{y}{s_2})^n] z^m$  over the plate is then an exercise in recognizing which source - observation pair is being encountered and choosing the appropriate Green's function value from a file. The computational saving is well worth the effort required to program the filing system.

### 6.7 Construction of the Matrix

Much of the foregoing discussion has been directed

toward expressing the elements of the matrix in Equation 2.10 in the form

$$f^i(\underline{r}_j) - (\sigma_3 - \sigma_2) \int G^P(\underline{r}_j | \underline{r}_s) f^i(\underline{r}_s) dV_s - (\sigma_3 - \sigma_2) \int G^S(\underline{r}_j | \underline{r}_s) f^i(\underline{r}_s) dV_s$$

where  $G^P$  and  $G^S$  denote a primary or secondary Green's function without specifying any particular tensor element. There is some advantage in creating a separate matrix of elements

$$\int G^P(\underline{r}_j | \underline{r}_s) f^i(\underline{r}_s) dV_s$$

since these terms are unaffected by the interfaces in the host media, and when the plate depth or upper layer conductivity is changed, only elements involving secondary Green's functions

$$\int G^S(\underline{r}_j | \underline{r}_s) f^i(\underline{r}_s) dV_s$$

need be recomputed. Obviously, neither of them need be recalculated when only the plate conductivity is changed, so two basic matrices are computed and stored for later use in assembling the main matrix.

### 6.8 Calculation of the Secondary Field at the Surface

Having established the matrix elements, the source vector (right hand side of Equation 2.10), which is the incident field at the match points, can be calculated using the method of Section 5.2, and the matrix equation is then completely specified. When the matrix equation has been solved for the coefficients of the trial functions, Equations 2.8 can be used to compute the vertical and horizontal components of the electric field at any point on the plate.

Using the results of Section 5.3, the vertical component



of the magnetic field at the receiver location is obtained by integrating over the plate the product of the horizontal electric field on the plate and the Green's function as given by Equation 5.20. Twentieth order Gauss quadrature was used for both the y- and z- variables with no regional subdivision of the plate.

## CHAPTER VII

### NUMERICAL RESULTS

#### 7.1 Introduction

The results of this chapter are presented with consideration for the fact that evidence supporting the veracity of the solution is not, for the most part, incontrovertible. It will be shown that certain necessary conditions are satisfied, but it cannot be shown that any sufficient conditions, such as agreement with experiment over a wide range of parameters, are met.

Before presenting the data it is necessary to define what is meant by a horizontal loop response, or measurement.

If

$H_Z^O$  = vertical magnetic field intensity at the receiver when all conductivities are zero,

$H_Z^H$  = vertical magnetic field intensity at the receiver in the presence of the host medium only, and

$H_Z^S$  = vertical magnetic field intensity at the receiver generated by the scatter currents only,

then the horizontal loop response defined for a point midway between the transmitter and receiver is

$$(P_R, Q_R) = \left[ \frac{H_Z^H + H_Z^S}{H_Z^O} - 1 \right] \times 100 \quad \text{Eq. 7.1}$$

given in percent. Some authors (C.P. Gupta, 1973) compare the field intensity at the receiver with field intensity in the presence of the medium only ( $H_Z^H$  in the denominator of the above expression) which leads to zero response at points remote from the scatterer. By comparing the intensity at the receiver with the field intensity in free space, a non-zero background response is obtained at remote locations which can be used in appraising the conductivity of the host medium. The response definition used herein is used by Gupta Sarma and Maru (1971). Since the transmitter-receiver distance is much less than a free space wavelength,  $H_Z^O$  is essentially a pure real number. However, both  $H_Z^H$  and  $H_Z^S$  are significantly phase-shifted with respect to the field at the source and are complex numbers, hence the designation  $(P_R, Q_R)$ .  $P_R$  (in-phase response) is the real part while  $Q_R$  (quadrature response) is the imaginary part. The response most different from the background response occurs when the array straddles the conductor and will be referred to as the peak anomaly value and designated  $(P_P, Q_P)$ .

During the development of the computer program, it was apparent that significant error occurred for source dipoles close to the plate. Interchanging the transmitter and receiver locations (both on the same side of the plate) produced different computed responses, contravening the theorem on reciprocity as well as basic field experience. Satisfying

the theorem on reciprocity is a necessary, but not sufficient condition for a valid solution. To signal any such obvious errors associated with the peak anomaly values presented in subsequent sections, a reciprocity test was devised and is described in Figure 7-1.  $Tx^1$  and  $Rx^1$  are used for obtaining the peak anomaly value. Two more responses are computed using the  $Tx^3 - Rx^3$  and  $Tx^2 - Rx^2$  arrays which should be reciprocal. If they are not, then either the current on the plate or the field at the receiver as computed from the current on the plate, or both, must be in error. Comparing the two in-phase values and the two quadrature values and expressing the differences in percent, yields an objective and quantitative description of one kind of error which can affect the validity of the peak anomaly value.

To avoid specifying conductivities, linear dimensions, and frequency, and to facilitate the correlation of the computed results with field data, dimensionless parameters are used to describe the conductivity regions. The parameters are defined as follows:

$$\text{plate } \alpha_p = \mu\omega\sigma_3tL$$

$$\text{host } \alpha_H = \mu\omega\sigma_2L^2$$

$$\text{layer } \alpha_L = \mu\omega\sigma_1dL$$

When  $t$  is much smaller than  $L$ ,  $\sigma_3t$  acts as a single variable, as does  $\sigma_1d$  when  $d$  is also small. Knowing the values of  $\omega$  and  $L$  used in the field, an interpreter can estimate  $\sigma_3t$ ,  $\sigma_1d$  and  $\sigma_2$  from the values of  $\alpha_p$ ,  $\alpha_H$  and  $\alpha_L$  which best fit his data.

Sections 7.2 and 7.3 present some numerical results

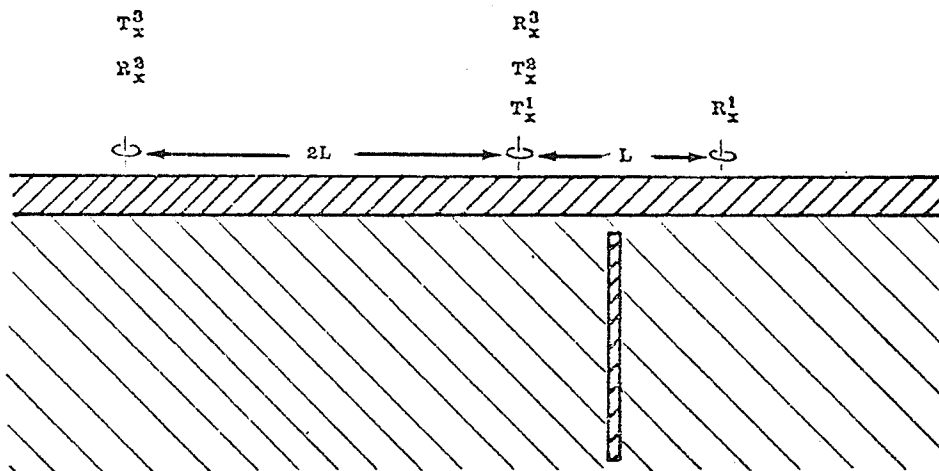


Figure 7-1 Transmitter and Receiver Locations for the Reciprocity Test

which qualitatively satisfy the basic physical requirements, while in Sections 7.4 to 7.6 an attempt is made to specify ranges within which the numerical solution can be regarded with some confidence.

### 7.2 The Effect of Host Conductivity on Peak Anomaly Value

A hypothetical horizontal loop response profile obtained from a traverse across a steeply dipping conductor in a conductive host is illustrated in Figure 7-2. The background response is designated  $(P_B, Q_B)$ , while the peak anomaly value is denoted  $(P_P, Q_P)$ . In the vicinity of the conductor the anomalous computed responses take on the background values at  $\pm L/2$ , corresponding to cases where the transmitter is over the conductor (no induced eddy currents) or when the receiver is over the conductor (secondary magnetic field has no vertical component). Positive and negative deviations occur when the primary and secondary fields add or subtract.

Several horizontal loop profiles for a conductor of size  $3L \times 1.5L \times .005L$  at a depth of  $.2L$  beneath the surface of a homogeneous half-space are given in Figure 7-3. The coil height above the surface is  $.005L$ . The plate response parameter increases in factors of 2 from 1 to 128 while the host parameter takes values 0, .25, .5, 1, ..., 32. The profiles are arrayed to demonstrate the effects of changing  $\alpha_P$  and  $\alpha_H$ . Progressing across a given row shows how the response of a plate of given  $\sigma_3 t$  changes for increasing values of host conductivity. The background values are seen to change as

$$\alpha_p = \mu \omega \sigma_3 t L$$

$$\alpha_H = \mu \omega \sigma_2 L^2$$

$$\alpha_L = \mu \omega \sigma_1 d L$$

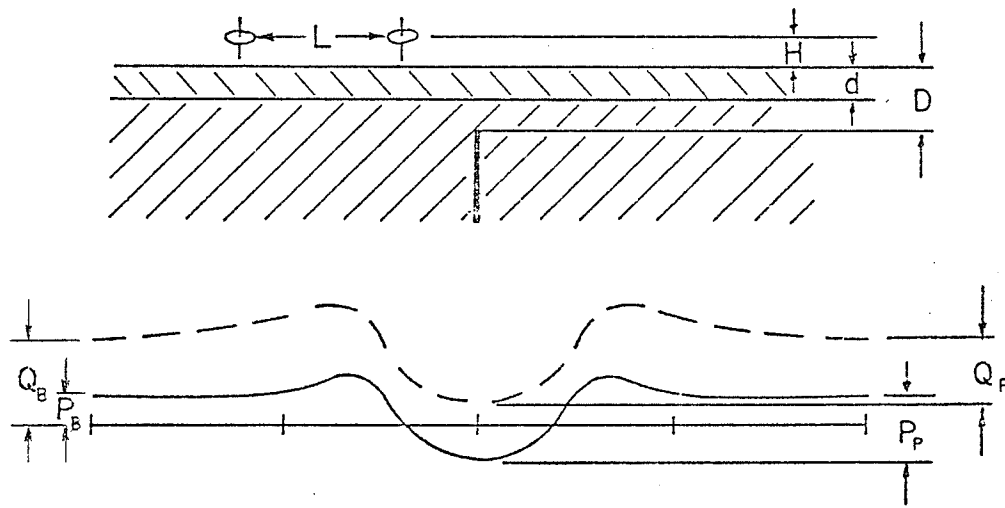


Figure 7-2 Typical Horizontal Loop Profile across a Vertical Conductor in a Conductive Host

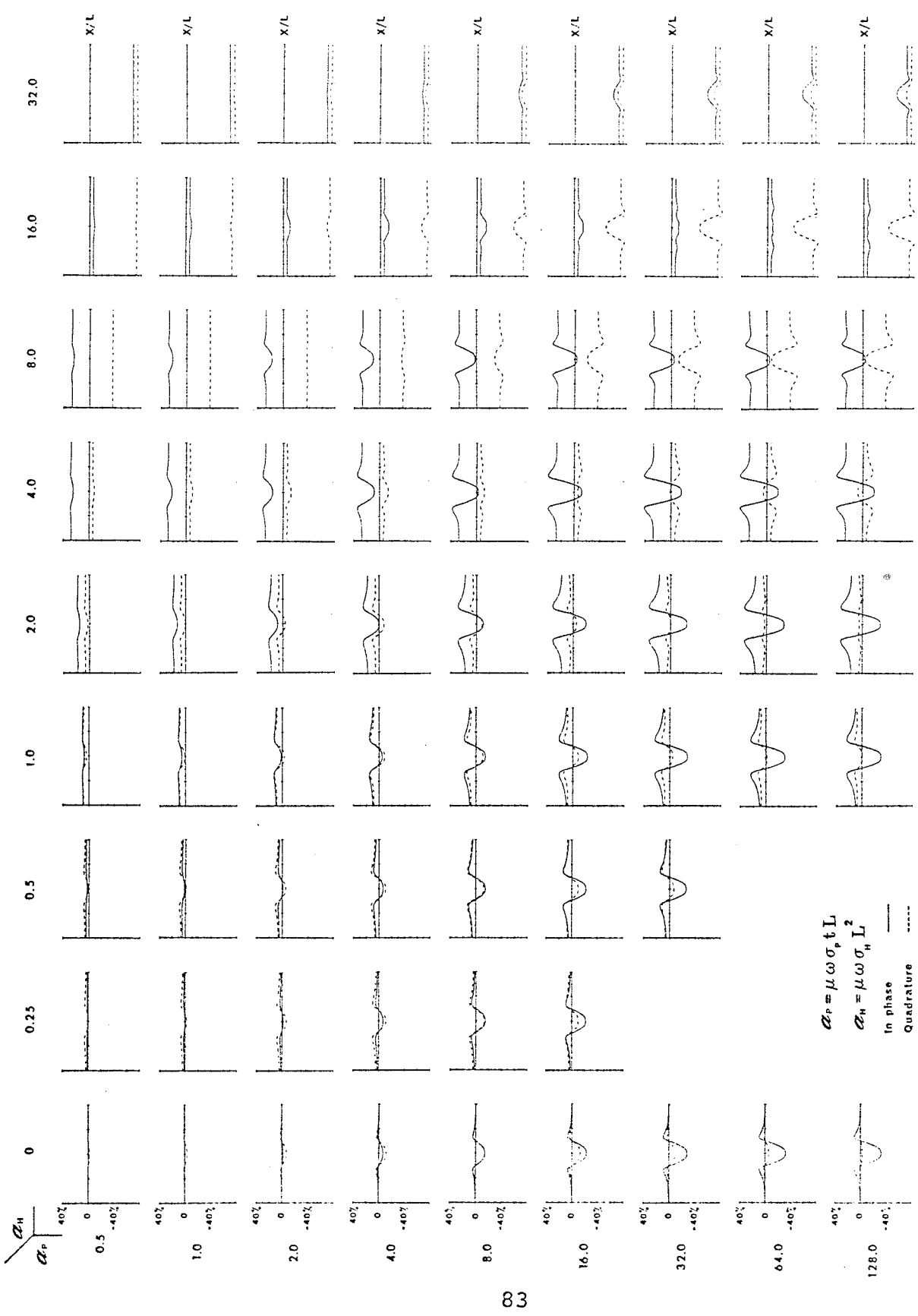


Figure 7-3: Horizontal loop response of a thin plate in a half space.



well as the magnitude,  $[(P_P - P_B)^2 + (Q_P - Q_B)^2]^{\frac{1}{2}}$ , and phase  $\tan^{-1}[(P_P - P_B)/(Q_P - Q_B)]$ , of the response at the centre of each profile. Proceeding down a given column shows changes in the profile when the plate conductivity increases but the host conductivity is held constant. The effect is one of increasing anomaly magnitudes and increasing phase angles. Progressing diagonally downward and to the right shows the effect of doubling  $\alpha_H$  and  $\alpha_P$  simultaneously, and is equivalent to doubling the operating frequency, all other parameters remaining constant. The five missing profiles of Figure 7-3 were eliminated because of unreliable results.

Figure 7-4 displays the plate current for the peak anomaly response in selected profiles from Figure 7-3. Two plate outlines are shown for each value of  $\alpha_P$  and  $\alpha_H$ , in order to display the in-phase and quadrature components of the current separately. The numbers above each current display indicate the maximum current amplitude (at the top centre of the plate) for each current display. The transmitter is  $.2L$  above the plate,  $.5L$  behind the plate and the magnetic dipole is directed along the positive  $z$ -axis. The  $\alpha_P = .5$  row of Figure 7-4 displays current distributions which, in form, do not greatly differ from the host currents in the absence of a conductor. The higher values of  $\alpha_H$  show greater concentrations of current at the top of the plate as well as significant phase rotation and amplitude attenuation. (For  $\alpha_H = .5$ ,  $\delta = 2L$  and for  $\alpha_H = 32$ ,  $\delta = L/4$  where  $\delta$  is the skin depth in the host.) Similar phase rotation and attenuation can be seen in other rows which depict

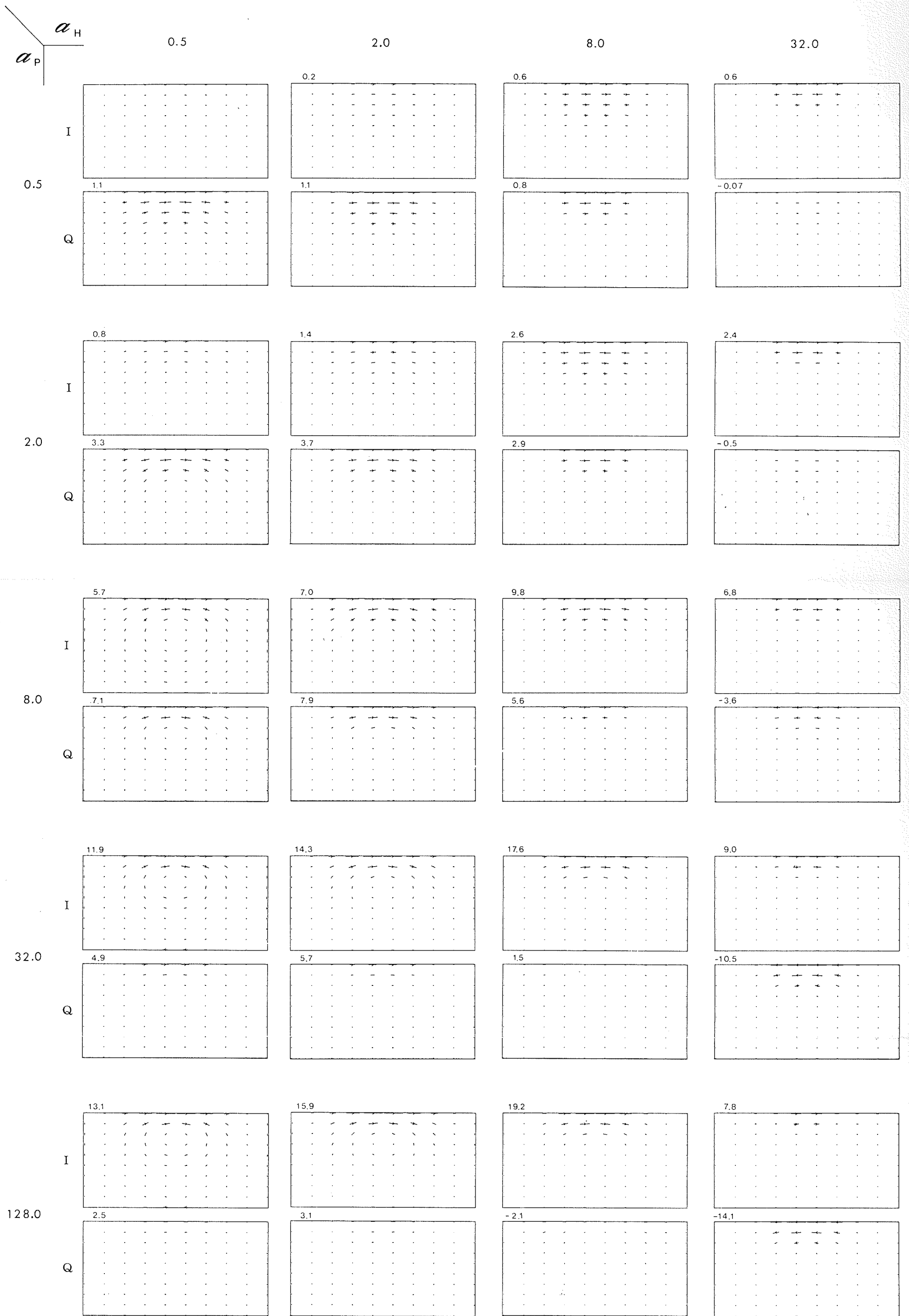


Figure 7-4: Plate current for peak anomaly value.

the current in plates of higher conductivity. The overall picture is one of magnetic effects manifest by a vortex when  $\alpha_P$  is greater than  $\alpha_H$ , and one of electric effects when  $\alpha_P$  is less than  $\alpha_H$ .

While it is really the inverse problem (use the observed results to calculate a model) which an interpreter must solve, the solution of the forward problem (specify a model and compute the response) requires enough effort as to make only a few iterations of a formal inversion routine prohibitively expensive. A more economical alternative is to epitomize each profile with the peak anomaly value and present many peak anomaly values on an Argand diagram of the type shown by Grant and West (1965), Strangway (1967), Nair, et al. (1968), and others. As seen in Figure 7-6 the responses are easily categorized for plates of constant depth (arcs) and plates of constant  $\alpha_P$  value (radiating lines). Figure 7-6 gives peak anomaly values for plates of size  $3L$  by  $1.5L$  in free space and was generated using program PLATE (A.V. Dyck, 1980).

Similar argand diagrams were prepared for plates in a conductive half-space. The response of the half-space host ( $P_B, Q_B$ ) for many values of  $\alpha_H$  is given in Figure 7-5. The maximum excursions from background, given by  $P = P_P - P_B$  and  $Q = Q_P - Q_B$  are presented for several values of  $\alpha_H$  in Figures 7-7a to 7-7i. The host response parameter increases in factors of 2 from  $\alpha_H = .125$  in Figure 7-7a to  $\alpha_H = 32$  in Figure 7-7i. Comparing the  $\alpha_H = 0$  and  $\alpha_H = .125$  Argand diagrams, it is apparent that

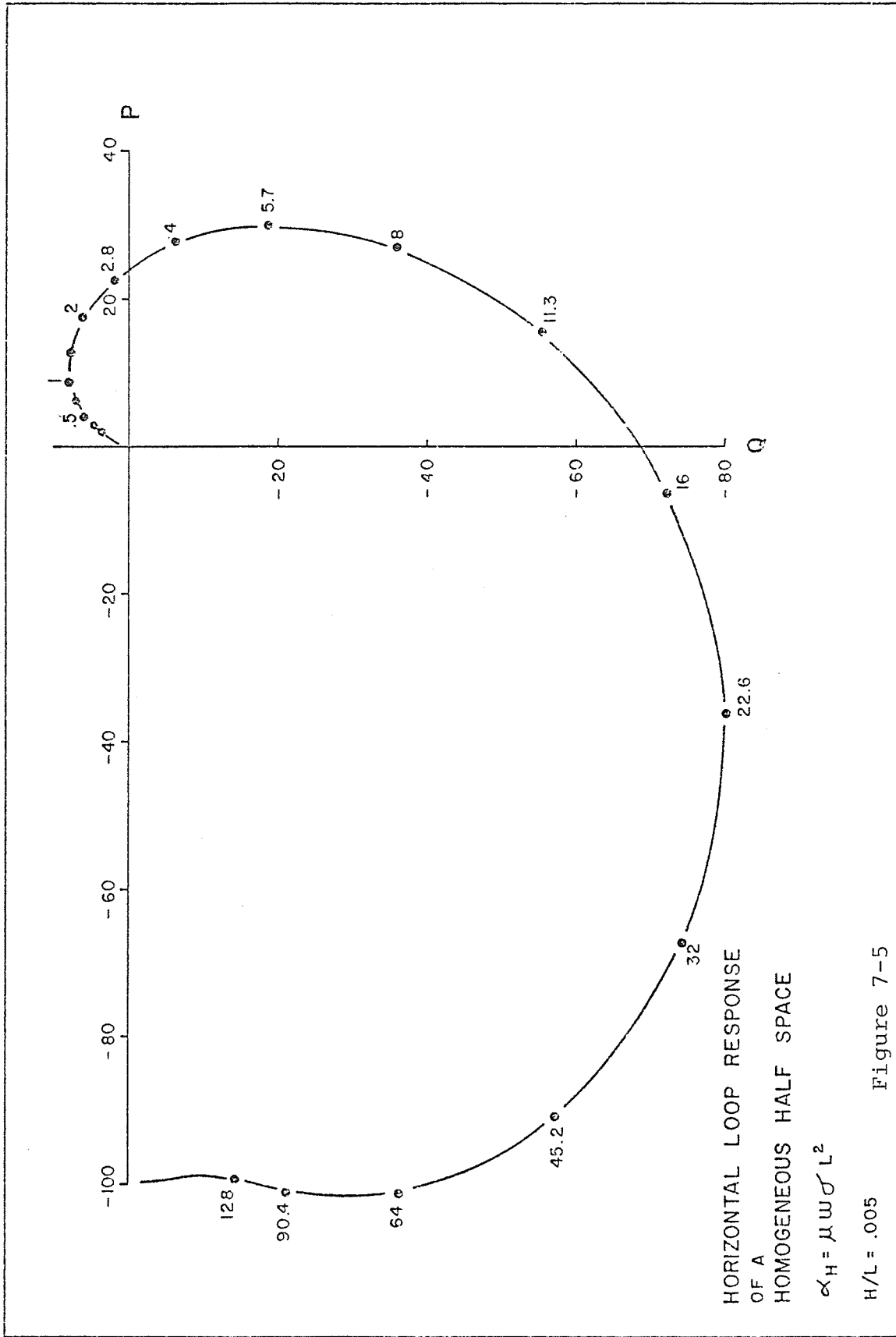


Figure 7-5

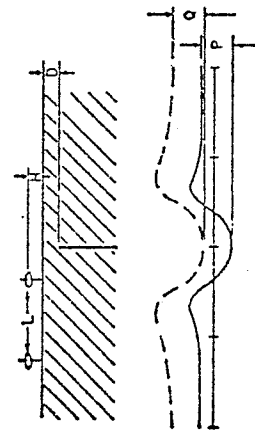
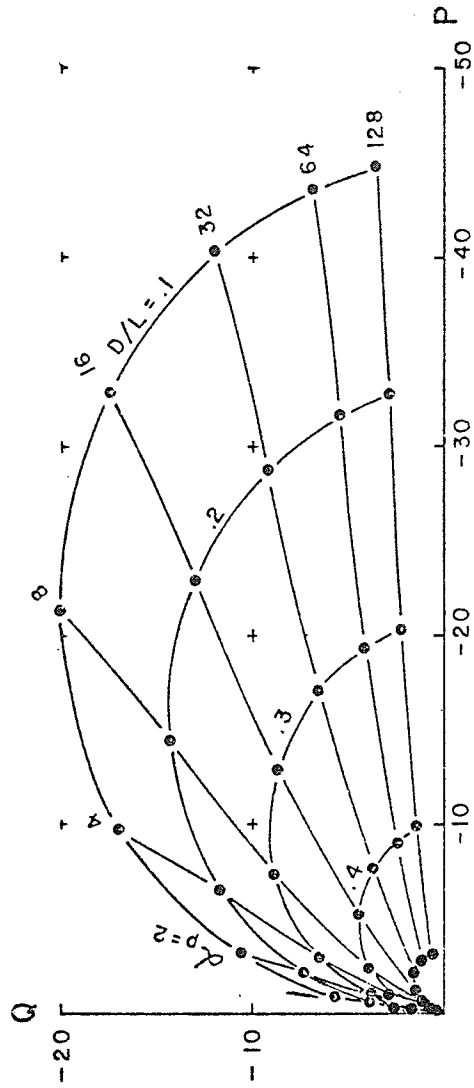


Figure 7-6  
 HORIZONTAL LOOP RESPONSE  
 LARGE VERTICAL CONDUCTOR  
 IN A  
 HOMOGENEOUS HALF-SPACE

$$\alpha_p = \mu \omega \sigma t L$$

$$\alpha_H = \mu \omega \sigma^2 = 0$$

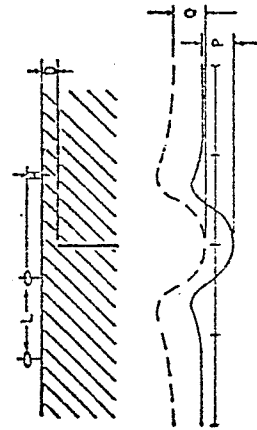
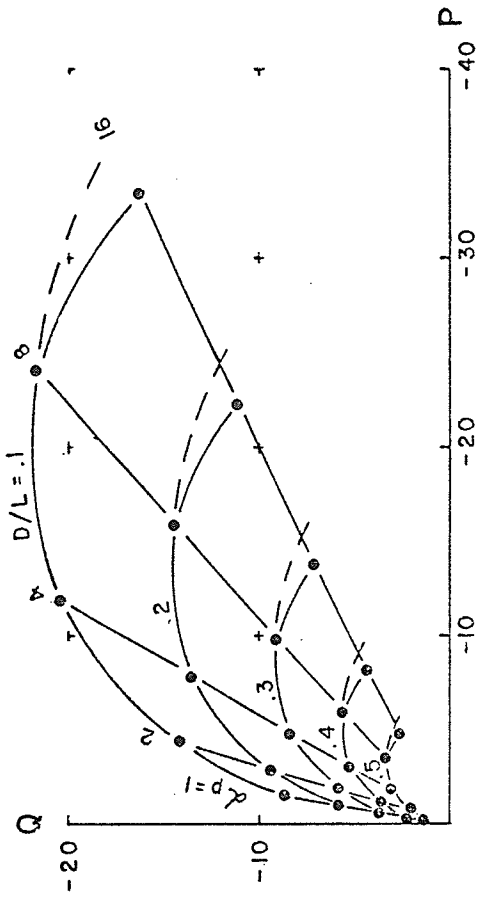


Figure 7-7a  
 HORIZONTAL LOOP RESPONSE  
 LARGE VERTICAL CONDUCTOR  
 IN A  
 HOMOGENEOUS HALF-SPACE

$$\alpha_p = \mu \omega \sigma l$$

$$\alpha_n = \mu \omega \sigma l^2 \cdot .125$$

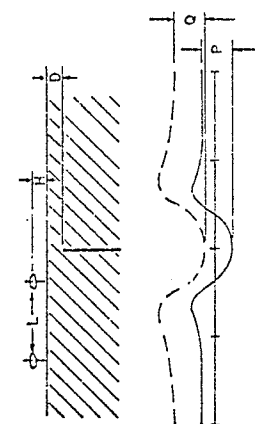
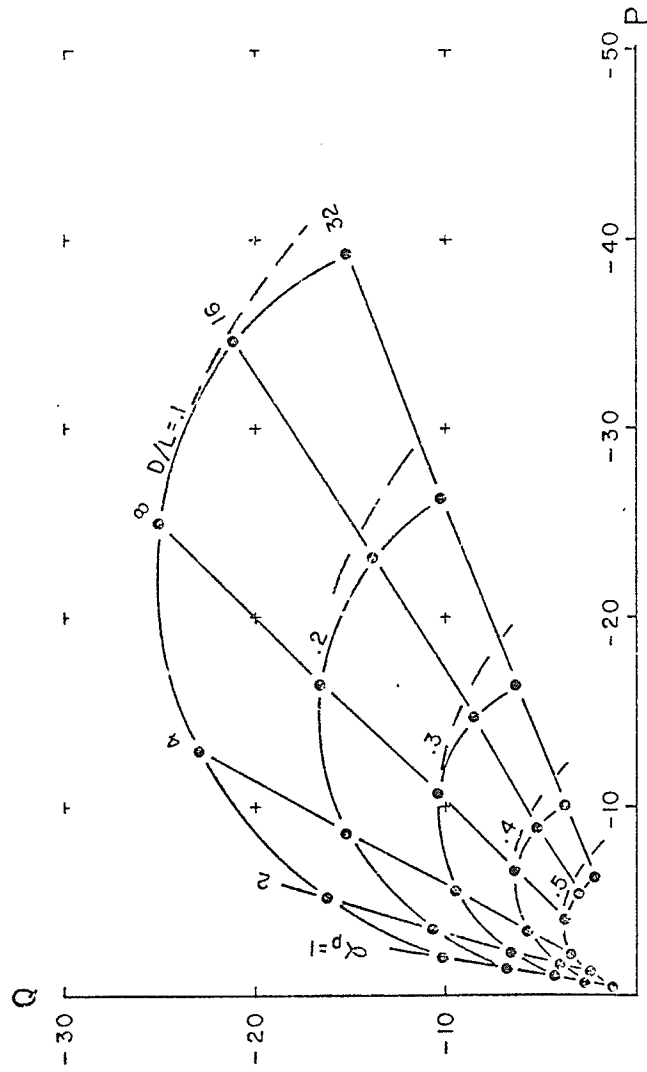


Figure 7-7b  
 HORIZONTAL LOOP RESPONSE  
 LARGE VERTICAL CONDUCTOR  
 IN A  
 HOMOGENEOUS HALF-SPACE  
 $\alpha_p = \mu_w \sigma L$   
 $\alpha_H = \mu_w \sigma L^2 \times .25$

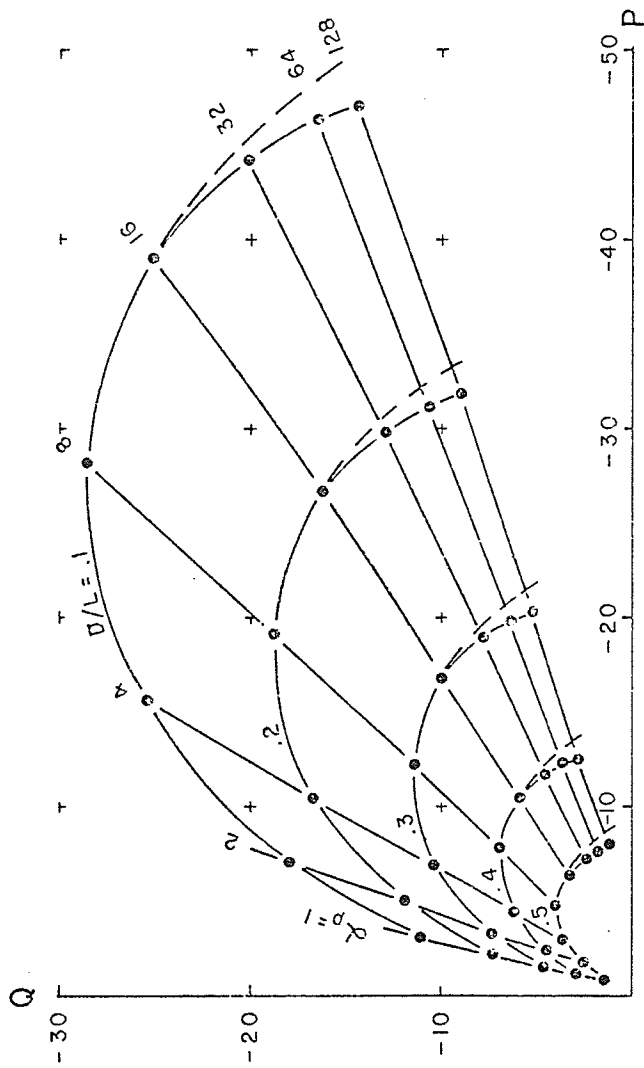
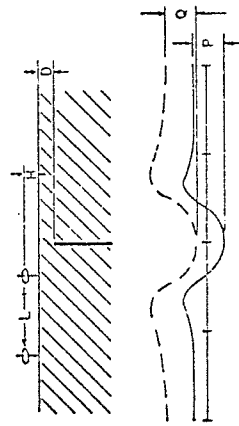


Figure 7-7c

HORIZONTAL LOOP RESPONSE  
 LARGE VERTICAL CONDUCTOR  
 IN A  
 HOMOGENEOUS HALF-SPACE

$$\alpha_p = \mu \omega \sigma l$$

$$\alpha_H = \mu \omega \sigma l^2 = .5$$





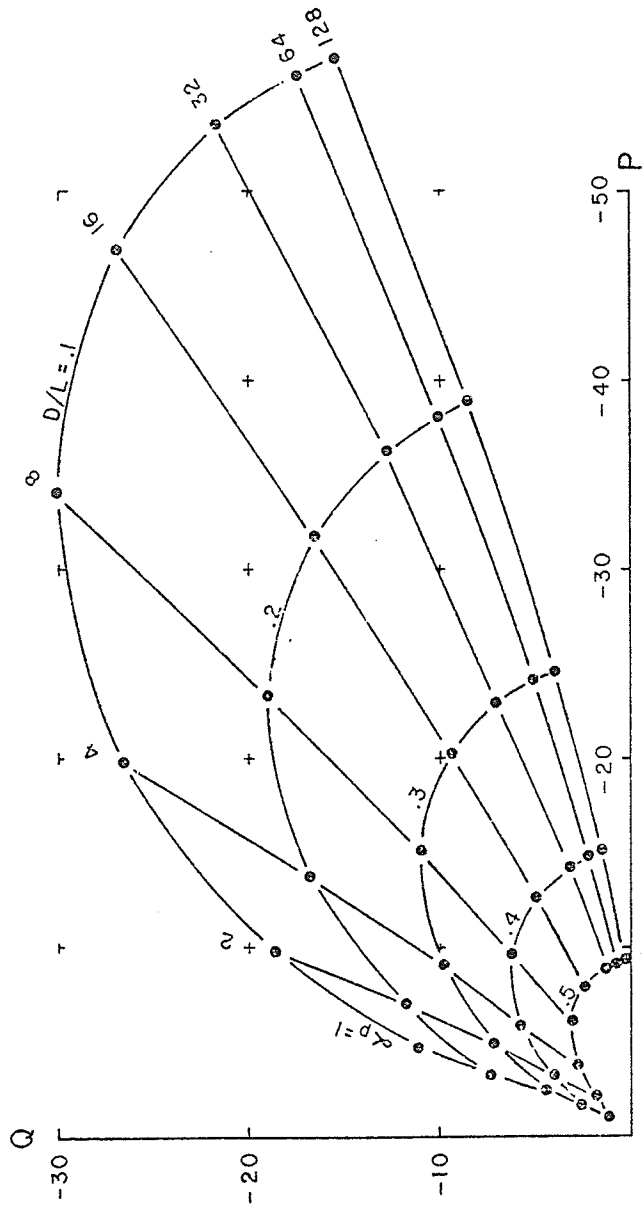
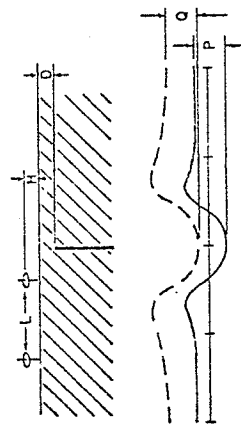


Figure 7-7d  
 HORIZONTAL LOOP RESPONSE  
 LARGE VERTICAL CONDUCTOR  
 IN A  
 HOMOGENEOUS HALF-SPACE

$$\alpha_p = \gamma_1 \omega \sigma \tau L$$

$$\alpha_H = \gamma_1 \omega \sigma \tau^2 \cdot 1$$



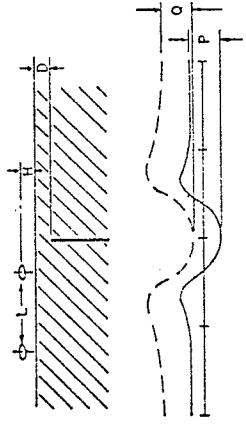
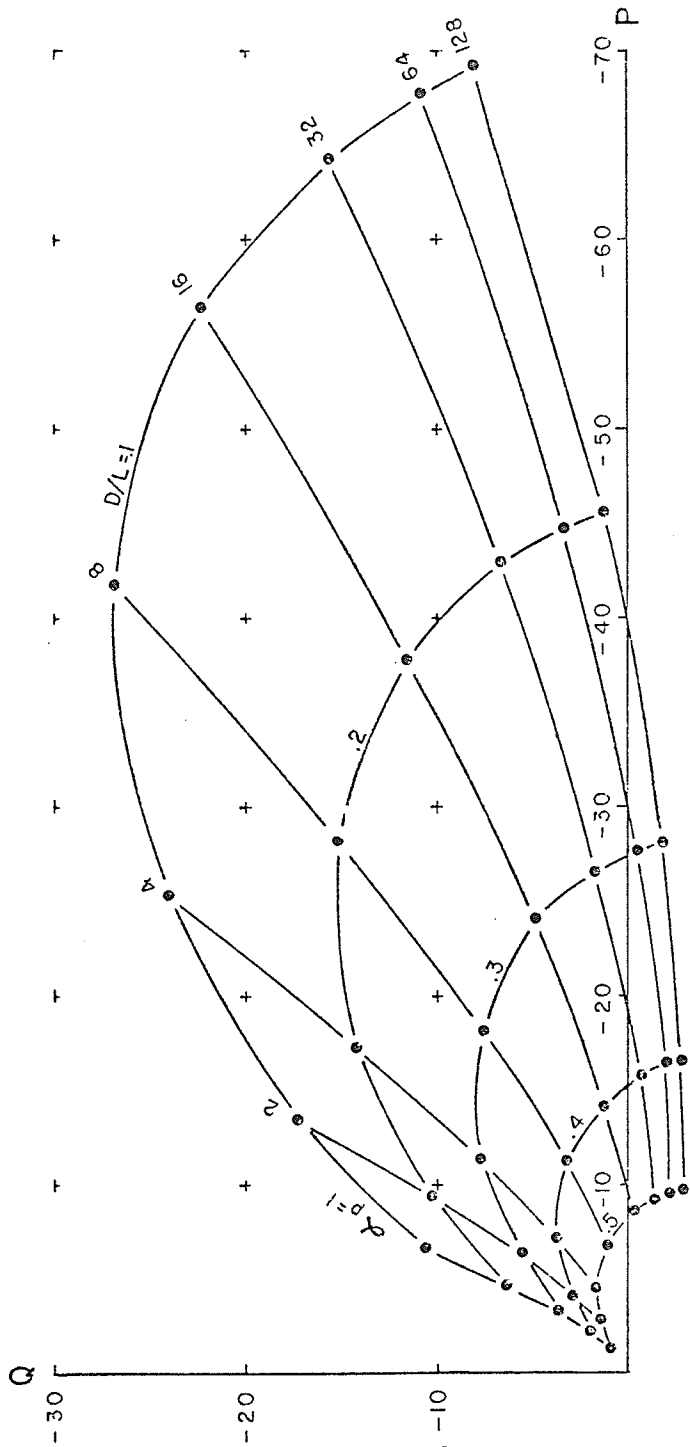


Figure 7-7e  
 HORIZONTAL LOOP RESPONSE  
 LARGE VERTICAL CONDUCTOR  
 IN A  
 HOMOGENEOUS HALF-SPACE  
 $\alpha_p = j\omega\sigma t L$   
 $\alpha_H = j\omega\sigma L^2 = 2$



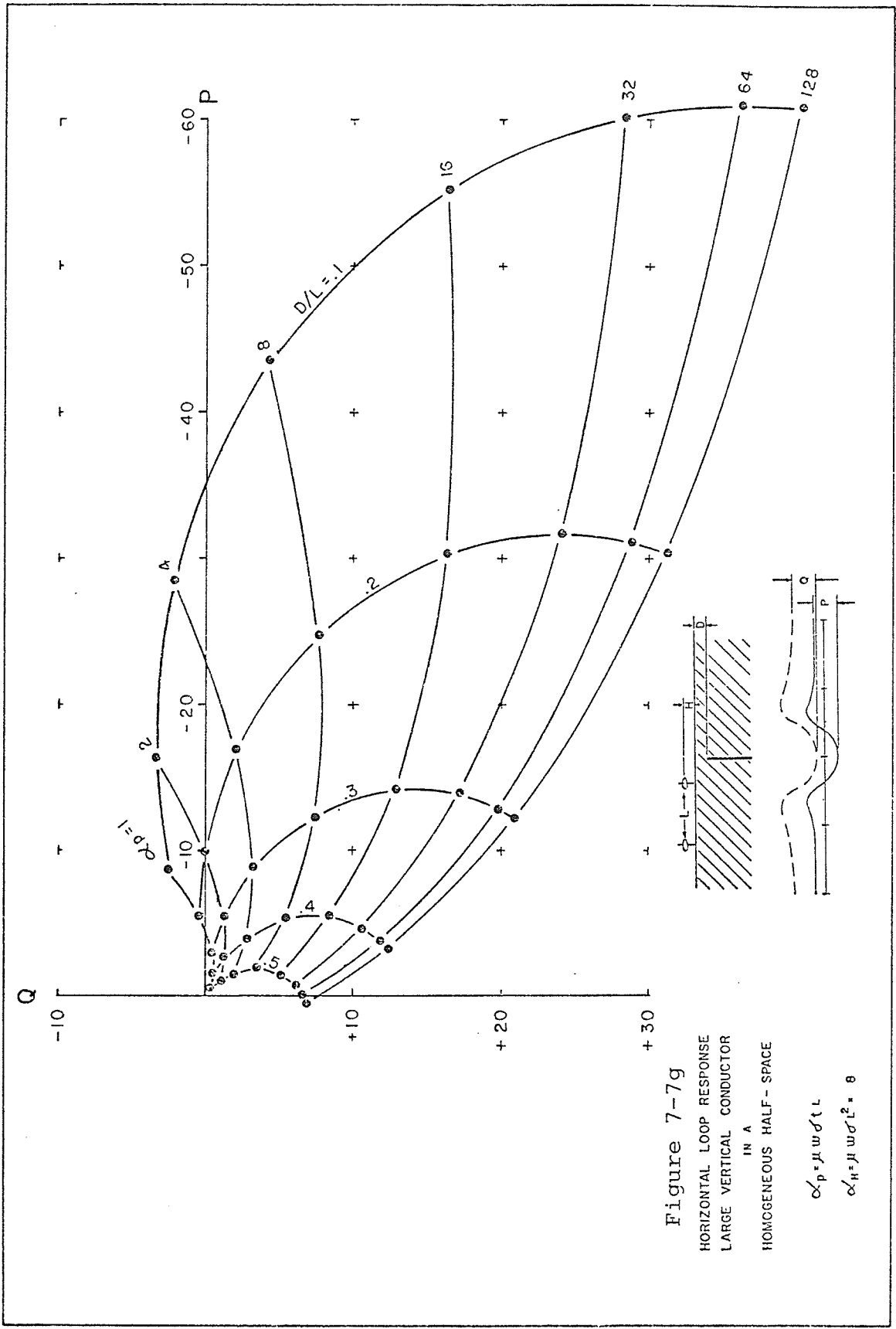


Figure 7-7h  
 HORIZONTAL LOOP RESPONSE  
 LARGE VERTICAL CONDUCTOR  
 IN A  
 HOMOGENEOUS HALF-SPACE

$$\alpha_p = \mu \omega \sigma l$$

$$\alpha_H = \mu \omega \sigma l^2 = 16$$

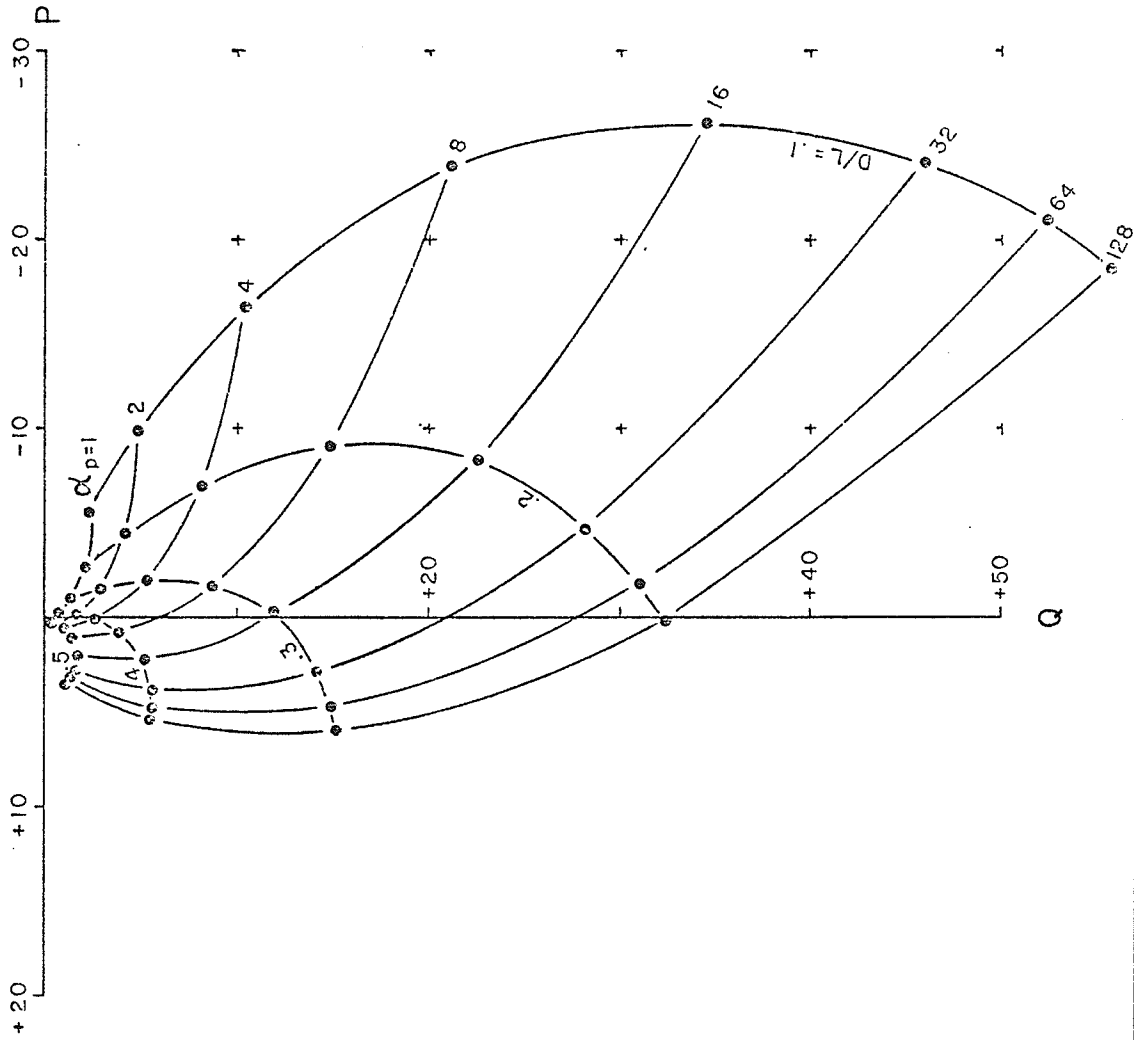
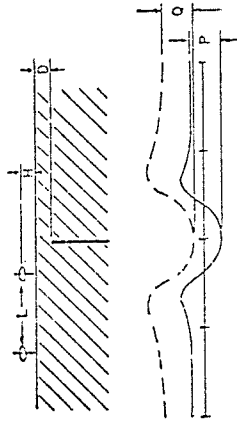
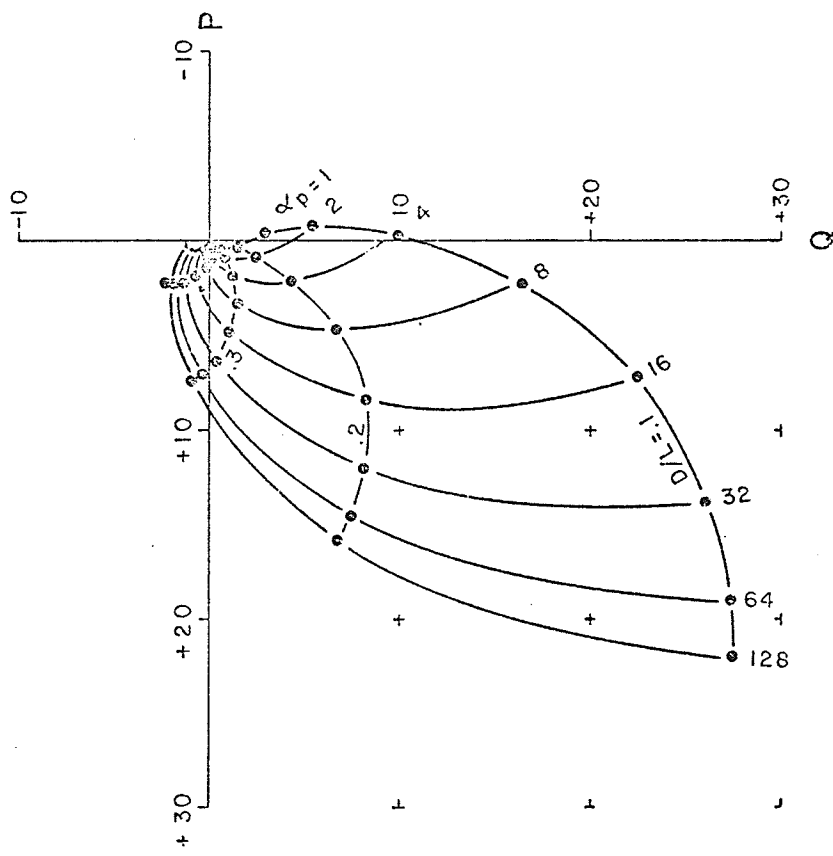
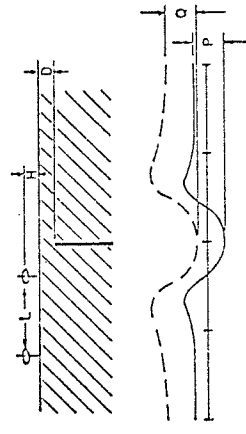


Figure 7-7i  
 HORIZONTAL LOOP RESPONSE  
 LARGE VERTICAL CONDUCTOR  
 IN A  
 HOMOGENEOUS HALF-SPACE

$$\alpha_p = \mu_w \sigma t L$$

$$\alpha_H = \mu_w \sigma t^2 \cdot 32$$



the initial effects of the host conductivity are to enhance the magnitude and rotate the phase slightly in the counter-clockwise direction. Further increase in the host response continues to enhance the anomaly magnitude, but clockwise changes in the phase begin to occur. Further increases in the background conductivity produce only clockwise anomaly rotations. Anomaly magnitudes increase with increasing  $\alpha_H$  until they are almost double the respective free space magnitudes at  $\alpha_H \approx 4$  (compare Figures 7-6 and 7-7f). Further increases in  $\alpha_H$  attenuate the anomaly magnitude while clockwise phase rotations continue.

Figure 7-8a combines the  $D/L=.2$  curves from Figures 7-6 and 7-7b to 7-7i, and shows in a single diagram the effect of changing host conductivity. For  $\alpha_H=4$  the horizontal loop response of the plate appears to be almost double its response in free space.

Figure 7-8b is constructed from the same data as Figure 7-8a, but the points are joined so as to illustrate the effect of increasing frequency. The dashed lines join points of constant  $\alpha_P/\alpha_H$  ratio while the solid lines join points having common  $\alpha_P$  values. The dashed lines can be interpreted as the loci of the conductor responses as the frequency changes, other parameters remaining constant. The solid lines are the loci of the response points for changing  $\sigma_3 t$ ; all other parameters, including frequency, held constant. The effect of increasing frequency is seen to be predominantly clockwise anomaly phase rotations coupled with dramatic increases (especially for low

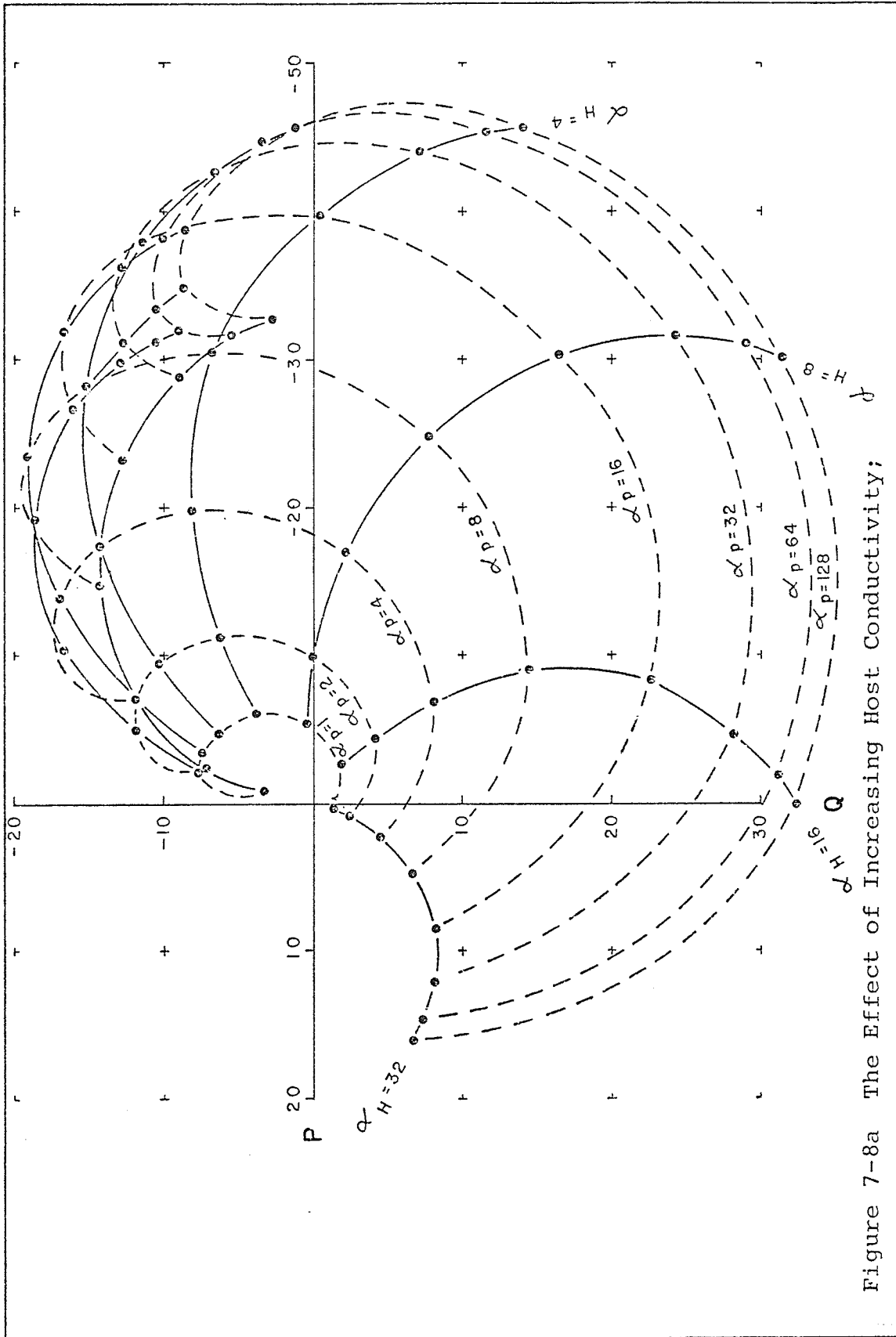


Figure 7-8a The Effect of Increasing Host Conductivity;



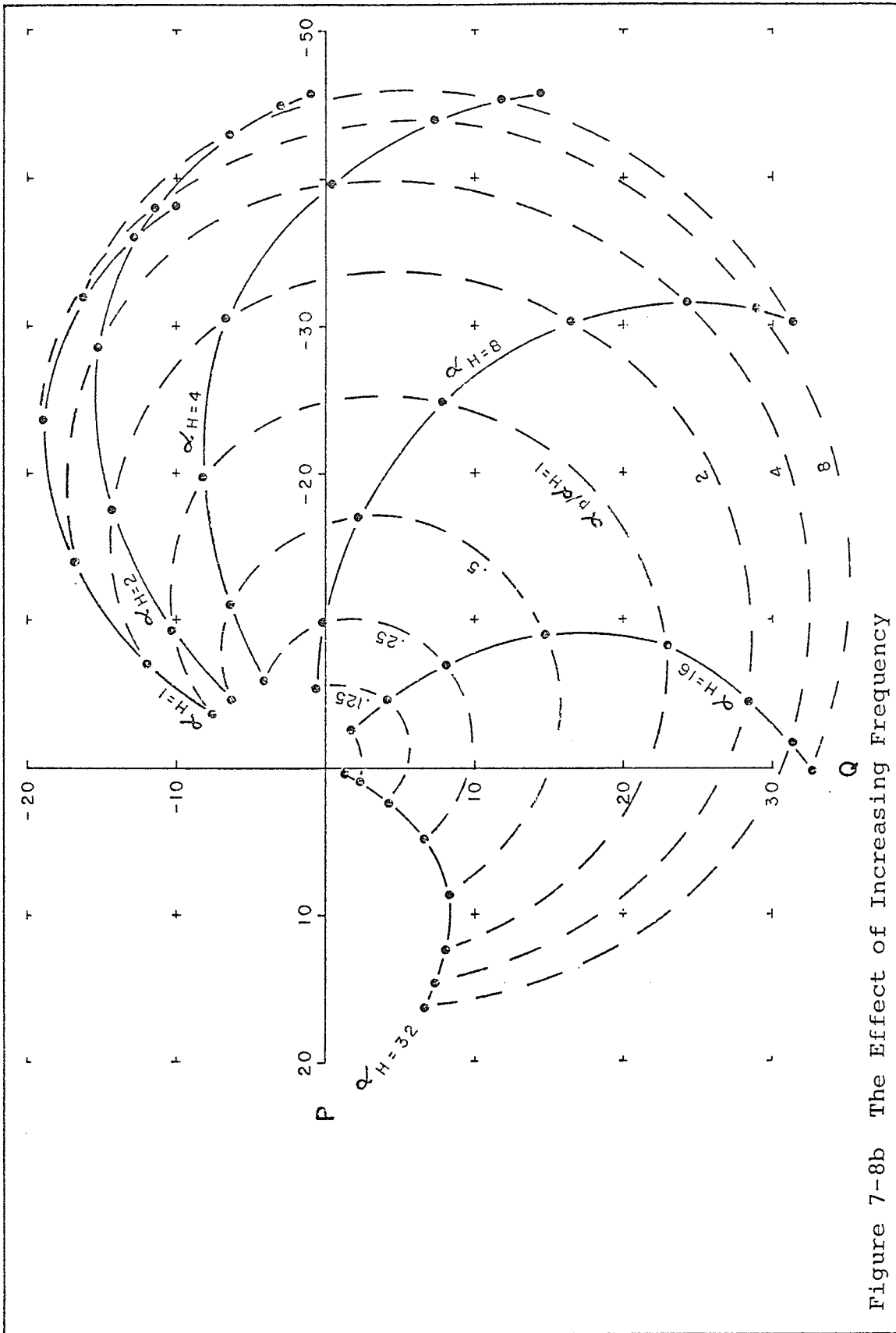


Figure 7-8b The Effect of Increasing Frequency

$\alpha_P/\alpha_H$  values) of a factor of 5 and greater in the anomaly magnitudes. It is apparent that for a given  $\alpha_P/\alpha_H$  value, there is an optimum prospecting frequency which maximizes the conductor response. The optimum frequency increases as  $\alpha_P/\alpha_H$  decreases and Figure 7-8b shows that for a conductor at a depth of  $.2L$  in a homogeneous half-space, the optimum prospecting frequency for  $\alpha_P/\alpha_H=1/8$  is about two octaves higher than it is for  $\alpha_P/\alpha_H=8$ . While only minor enhancements occur for high  $\alpha_P/\alpha_H$  values, the present analysis could be useful in designing a survey to detect faults or shear zones where  $\alpha_P/\alpha_H$  values are considerably lower and the enhancements due to frequency optimization are much greater. Qualitatively similar frequency effects have been described by Lajoie and West (1976) for the Turam prospecting method.

In Figures 7-7a, b and c, the constant depth arcs have dashed branches for high  $\alpha_P$  values where the solution, for reasons given in Section 7.4, is believed to be invalid. The dashed lines give what are believed to be better estimates of the correct responses.

### 7.3 The Conductive Overburden Effect

After the homogeneous half-space, the next simplest host model is the two-layer earth and is useful in simulating overburden effects. The effect of conductive overburden, provided it is not in electrical contact with the target conductor, is to partially shield the conductor from the incident field generated at the surface. This effect is demonstrated in

Figure 7-9 which gives computed responses for a  $3L \times 1.5L$  plate at depth  $.2L$  beneath the surface of a two-layer earth. The layer thickness is  $.05L$ . Conductivities and frequency are chosen so as to make  $\alpha_H = .5$  while  $\alpha_P$  ranges from 1 to 64 in factors of 2 and  $\alpha_L$  ranges from  $.125$  to 8, also in factors of 2.  $\alpha_L = .125$  represents, for  $d = .05L$ , a conductivity ratio ( $\sigma_1/\sigma_2$ ) of 10.

As the conductivity of the upper layer increases, the immediate effect is a clockwise rotation of the anomaly phase. Anomaly attenuation becomes apparent when  $\alpha_H$  exceeds 2, and the anomaly enhancement discussed in Section 7.2 is absent; the lower layer conductivity being kept constant.

Phase diagrams were computed for a vertical conductor in a two-layer earth. The chosen earth model has a layer thickness of  $0.05L$  and an upper layer conductivity 3.2 times as great as that of the lower medium ( $\sigma_1/\sigma_2 = 3.2$ ). The horizontal loop response of this earth model is shown in Figure 7-10 and the index numbers along the curve are the values of  $\alpha_H$ . Figure 7-10 can be used by an interpreter to appraise the similarities between the host media encountered in the field and the numerical model before attempting to fit the conductor response to the phase diagrams that follow in Figures 7-11a to 7-11f. The phase diagrams themselves require little discussion except to note that anomalies are relatively more attenuated and phase rotated clockwise compared to those cases where the overburden has the same conductivity as the lower layer. This illustrates again the effect of phase rotation and attenuation of primary

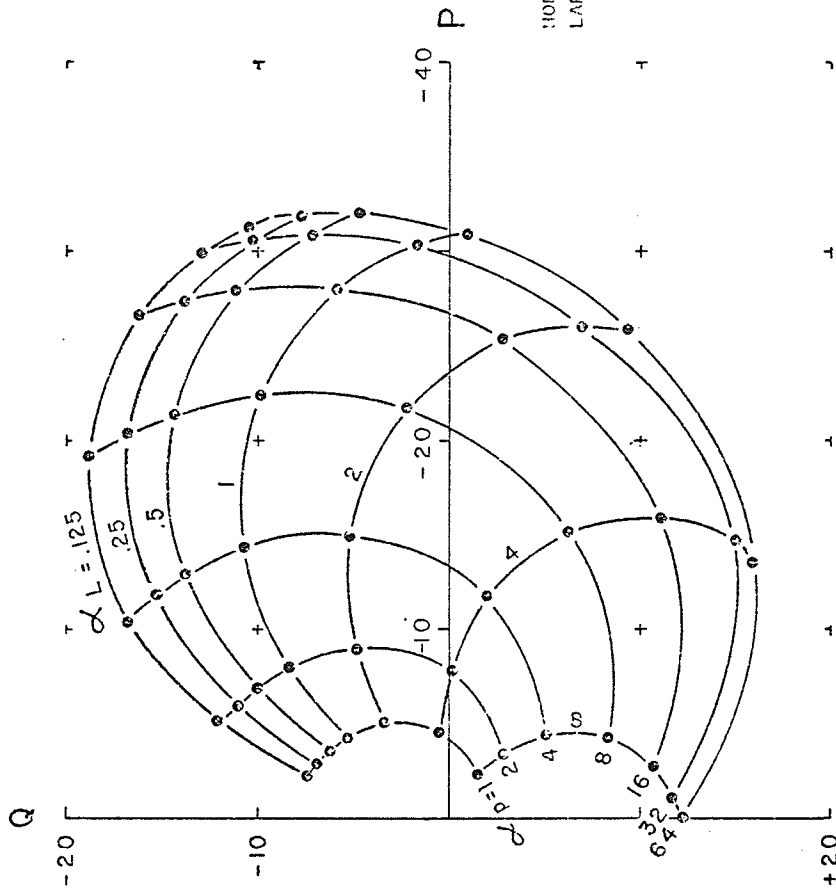


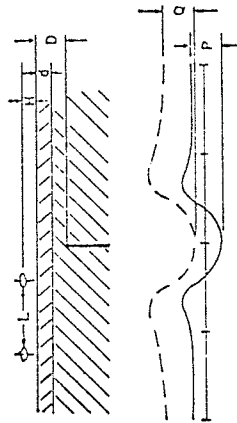
Figure 7-9

HORIZONTAL LOOP RESPONSE  
 LARGE VERTICAL CONDUCTOR  
 IN A  
 TWO-LAYER EARTH

$$\alpha_p = \mu_1 \omega \sigma_1 t$$

$$\alpha_H = \mu_1 \omega \sigma_1 L^2 + .5$$

$$\alpha_L = \mu_1 \omega \sigma_1 L = \text{VARIABLE}$$



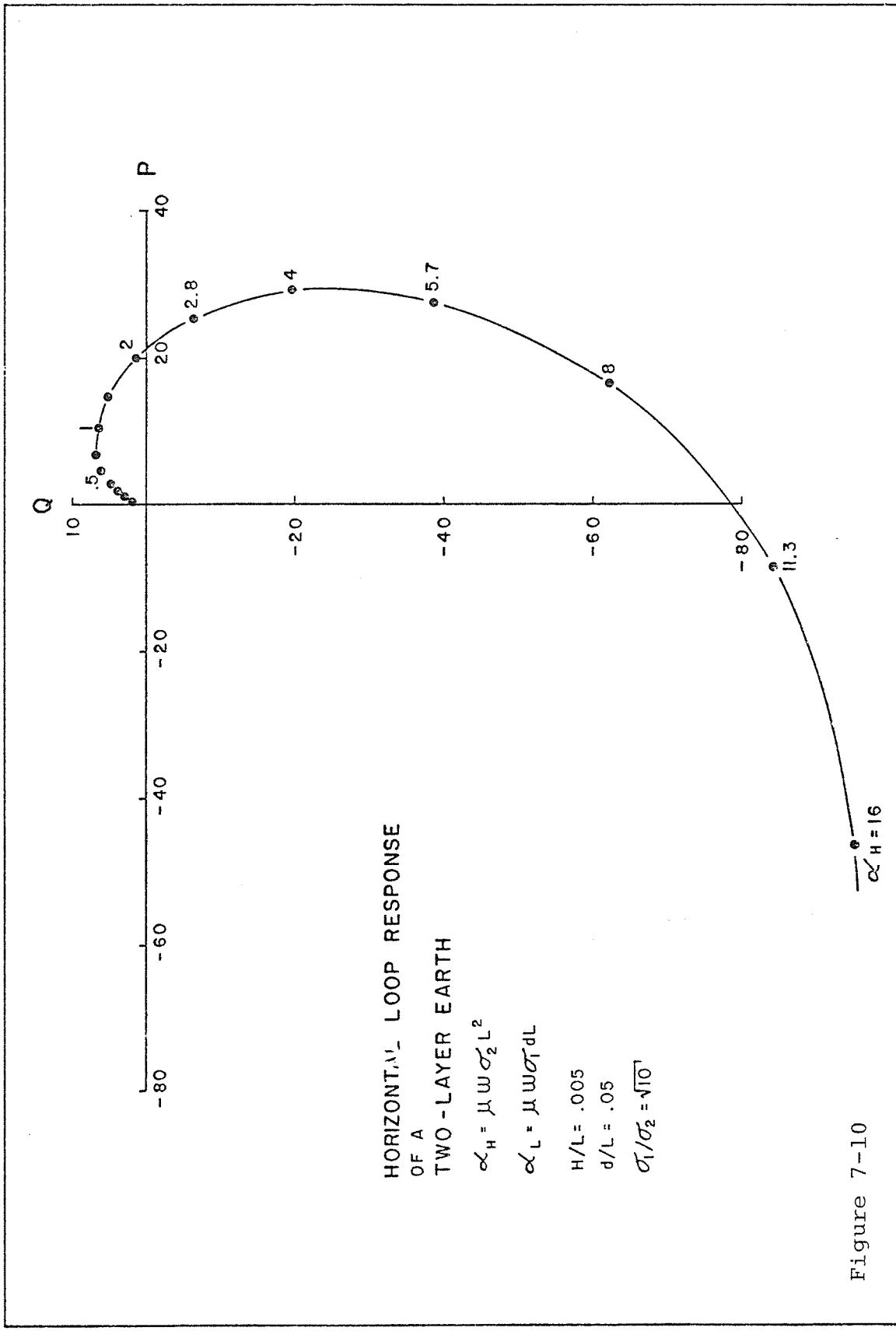


Figure 7-10

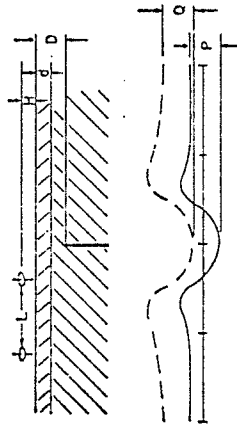
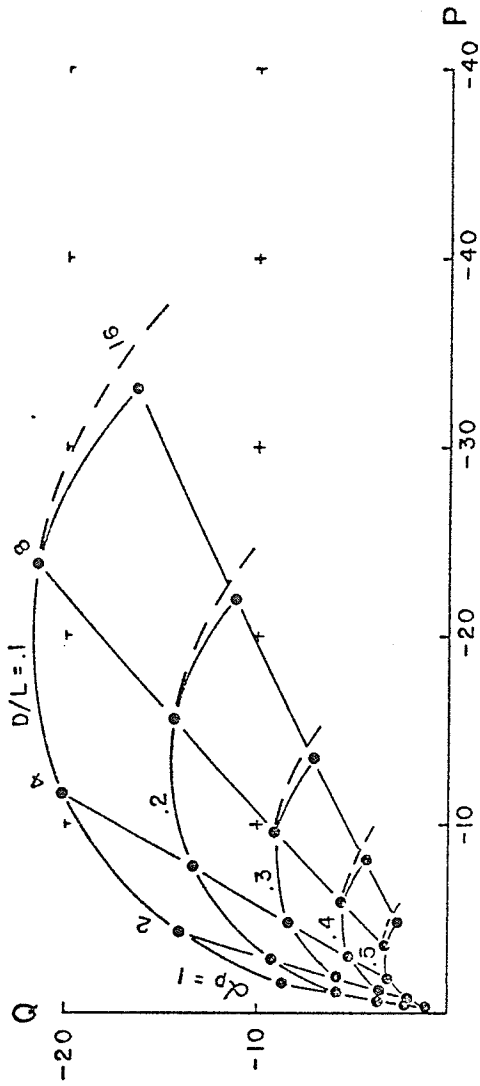
Figure 7-11a

HORIZONTAL LOOP RESPONSE  
 LARGE VERTICAL CONDUCTOR  
 IN A  
 TWO-LAYER EARTH

$$\alpha_P = \mu \omega \sigma_1 t_L$$

$$\alpha_H = \mu \omega \sigma_1 l^2 = .125$$

$$\alpha_L = \mu \omega \sigma_{eq} L = .02$$



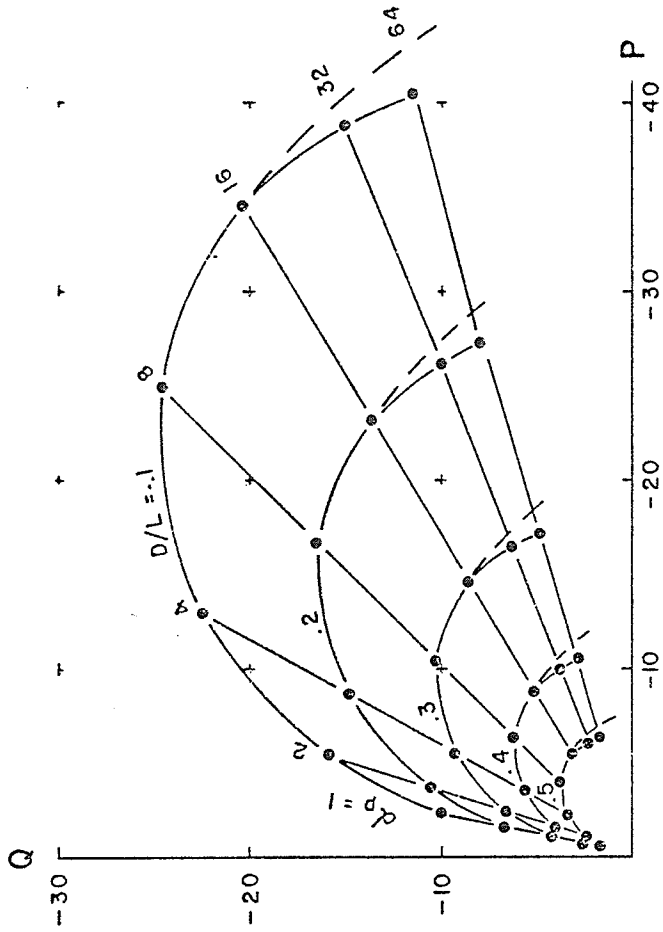


Figure 7-11b

HORIZONTAL LOOP RESPONSE  
LARGE VERTICAL CONDUCTOR

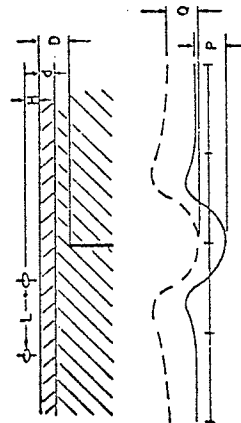
IN A

TWO-LAYER EARTH

$$\alpha_p = \mu_1 \omega \sigma_1 t_1$$

$$\alpha_H = \mu_1 \omega \sigma_2^2 = .25$$

$$\alpha_L = \mu_1 \omega \sigma_2 t_2 = .04$$



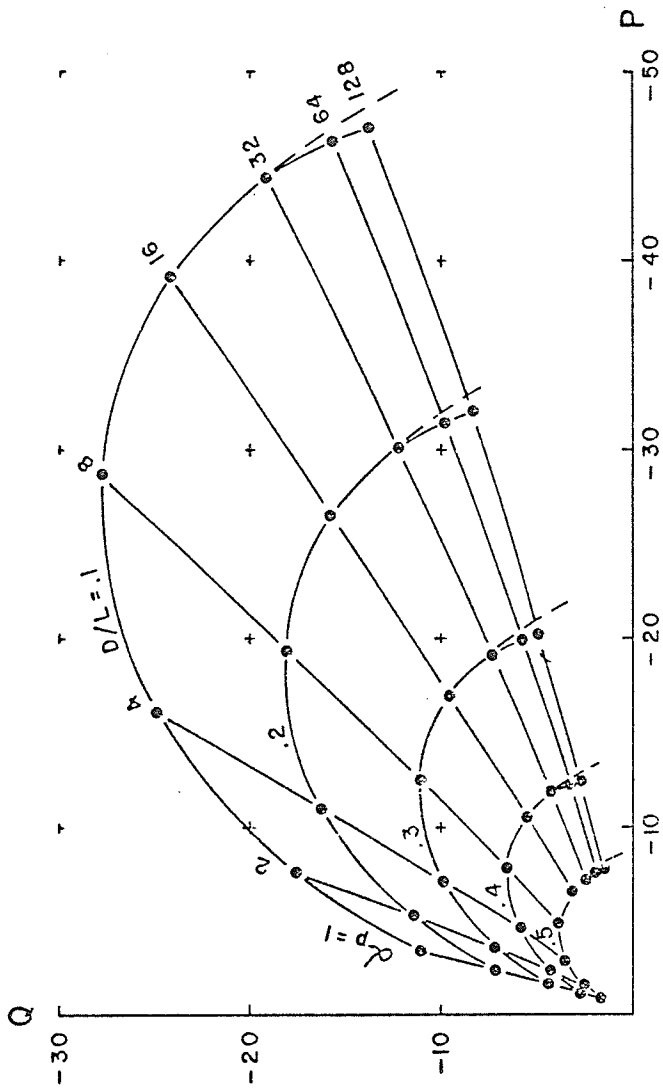


Figure 7-11c

HORIZONTAL LOOP RESPONSE  
LARGE VERTICAL CONDUCTOR

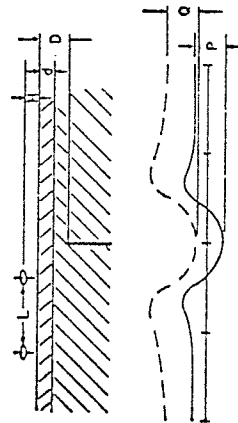
IN A

TWO-LAYER EARTH

$$\alpha_p = \mu_1 \omega \sigma_1^2 L$$

$$\alpha_H = \mu_1 \omega \sigma_2^2 \cdot .5$$

$$\alpha_L = \mu_1 \omega \sigma_2 L \cdot .08$$





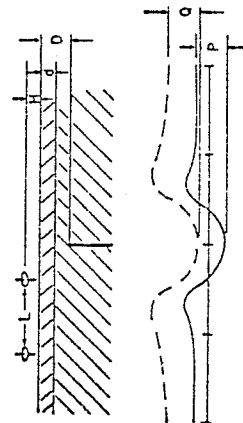
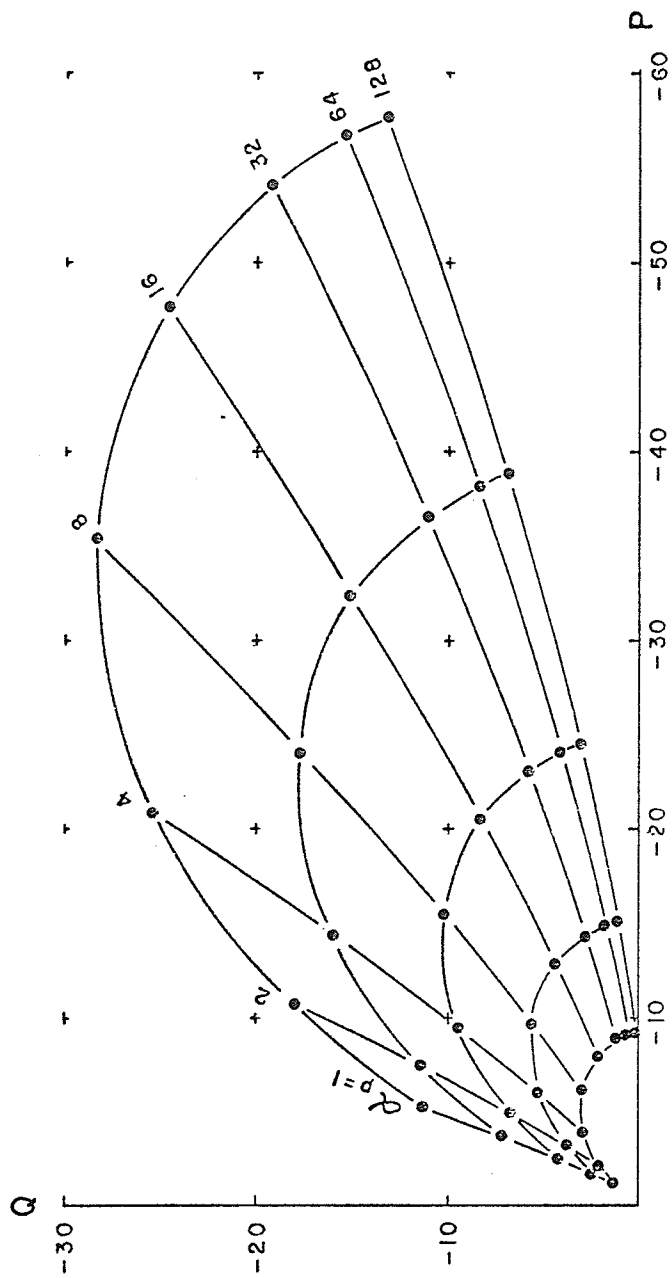


Figure 7-11d

HORIZONTAL LOOP RESPONSE  
LARGE VERTICAL CONDUCTOR  
IN A

TWO-LAYER EARTH

$$\propto \rho \cdot \mu \cdot \omega \sigma_1^2 L$$

$$\propto \mu \cdot \mu \cdot \omega \sigma_1^2 \cdot 1$$

$$\propto \rho \cdot \mu \cdot \omega \sigma_1 \cdot 16$$

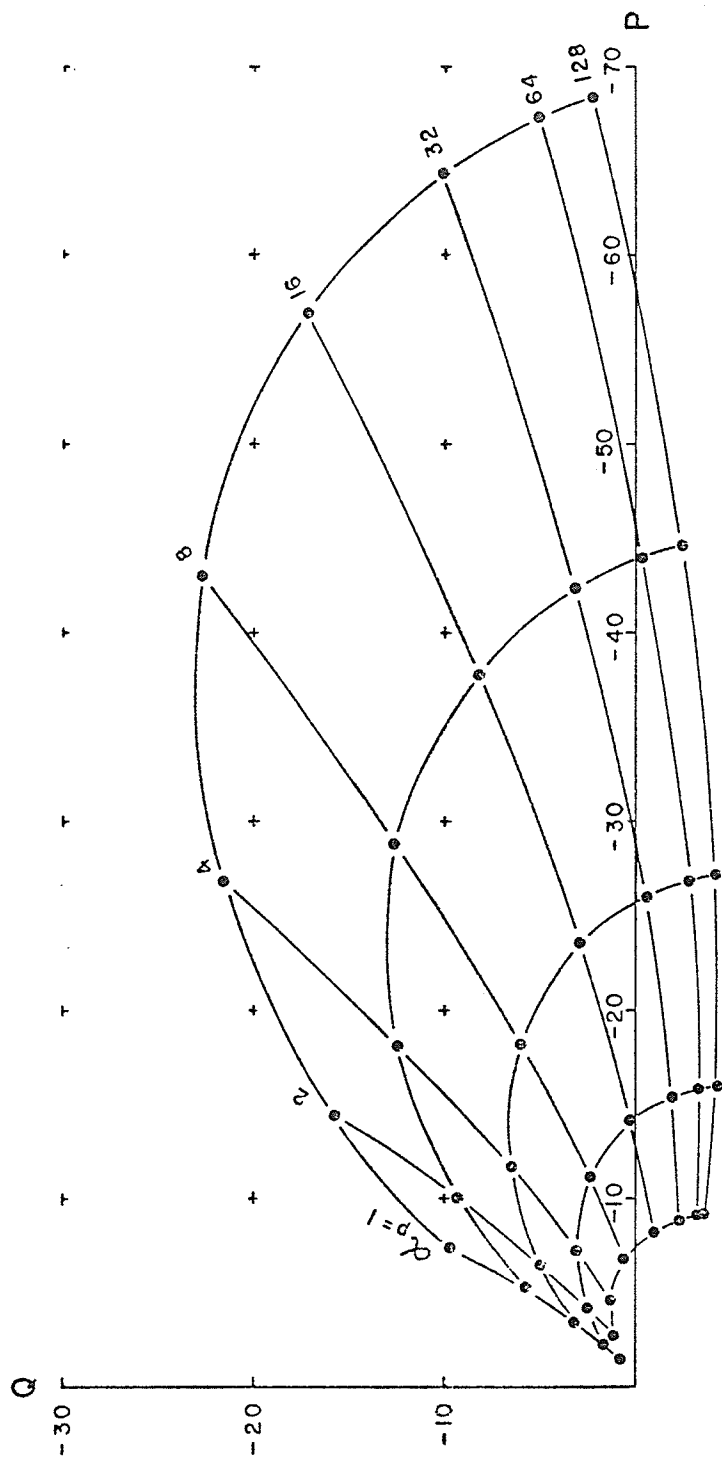


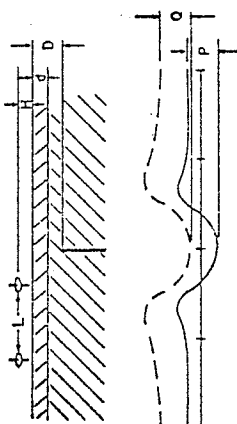
Figure 7-11e

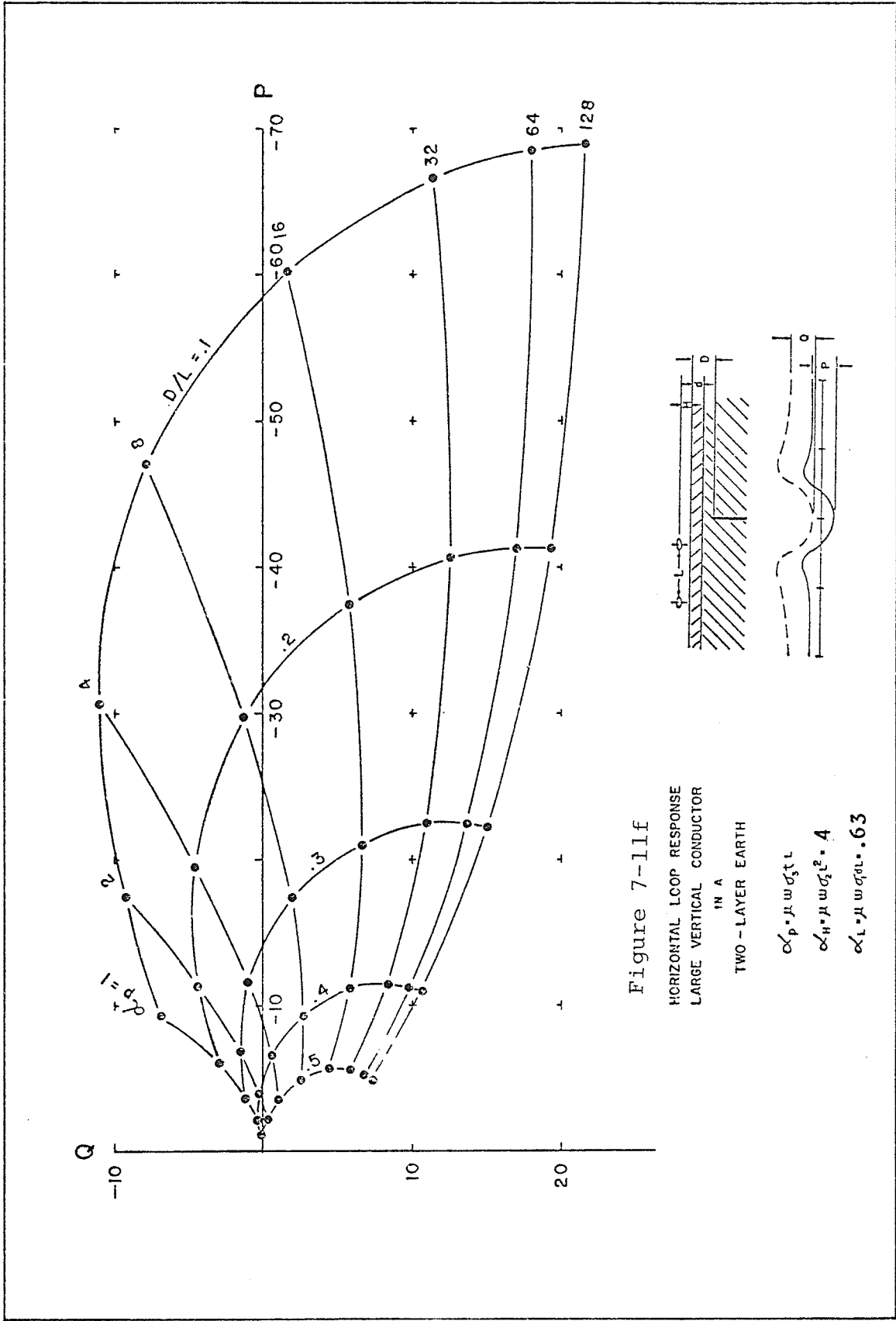
HORIZONTAL LOOP RESPONSE  
 LARGE VERTICAL CONDUCTOR  
 IN A  
 TWO-LAYER EARTH

$$\alpha_p = \mu_w \sigma_1 t_L$$

$$\alpha_H = \mu_w \sigma_1^2 \cdot 2$$

$$\alpha_L = \mu_w \sigma_1 t_L \cdot .32$$





and secondary fields passing through the more conductive layer.

Additional Argand diagrams were prepared in order to accommodate a wider range of host media in the interpretation of field data. Figures 7-12 to 7-17e comprise three additional suites of Argand diagrams for layered hosts having increasingly conductive upper layers. Each suite is preceded by a response curve for the host only (See Figure 7-12,  $\alpha_L/\alpha_H = .5$ ; Figure 7-14,  $\alpha_L/\alpha_H = 1.6$ , and Figure 7-16,  $\alpha_L/\alpha_H = 5$ ). When measured background values from a multi-frequency survey are found to lie on one of the host response curves, the response parameter,  $\alpha_H$  for the lower layer can be estimated for each frequency and the appropriate Argand diagrams for a vertical plate in that particular host can be employed to estimate depth and conductivity-thickness.

#### 7.4 Finiteness of the Background Resistivity

In the early stages of program development and testing, it was apparent that highly conducting plates in weakly conducting hosts were being poorly modelled. The judgement was based on physical intuition and the manifestation of the problem lay in the behaviour of the current on the plate. The in-phase component of current density at a given point, near the top centre of the plate say, is expected to increase as the plate

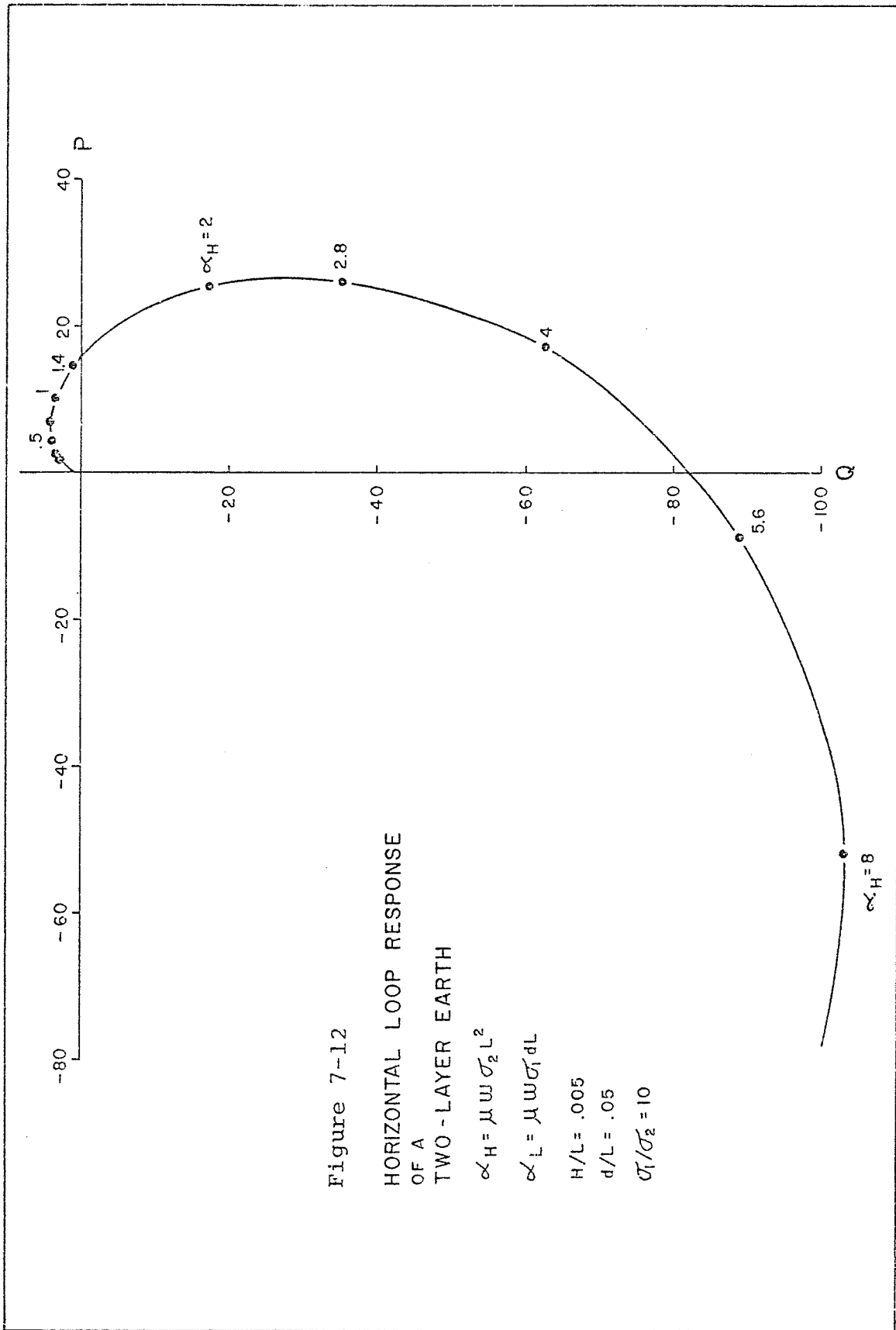


Figure 7-13a

HORIZONTAL LOOP RESPONSE  
LARGE VERTICAL CONDUCTOR

IN A

TWO-LAYER EARTH

$$\alpha_p = \mu_1 \omega \sigma_2 L$$

$$\alpha_H = \mu_1 \omega \sigma_2 L^2 = .125$$

$$\alpha_L = \mu_1 \omega \sigma_1 L = .06$$

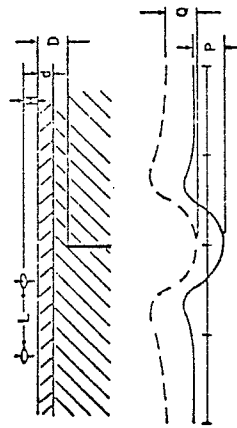
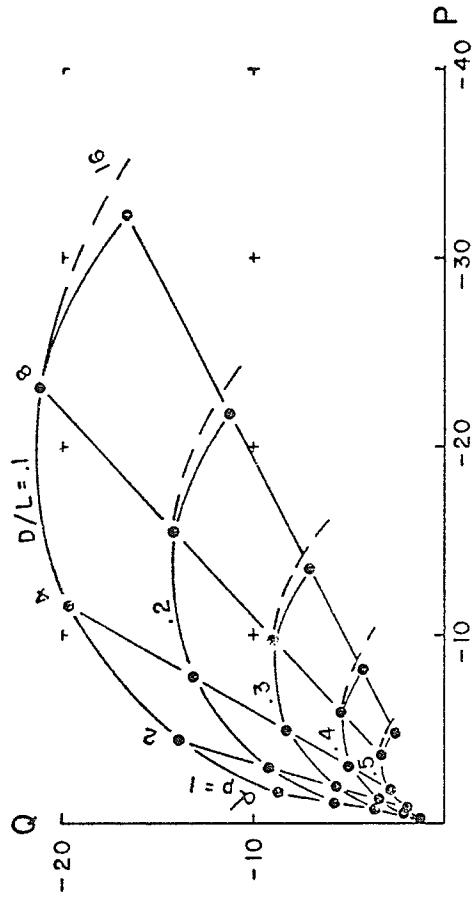


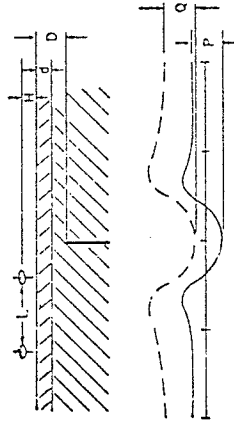
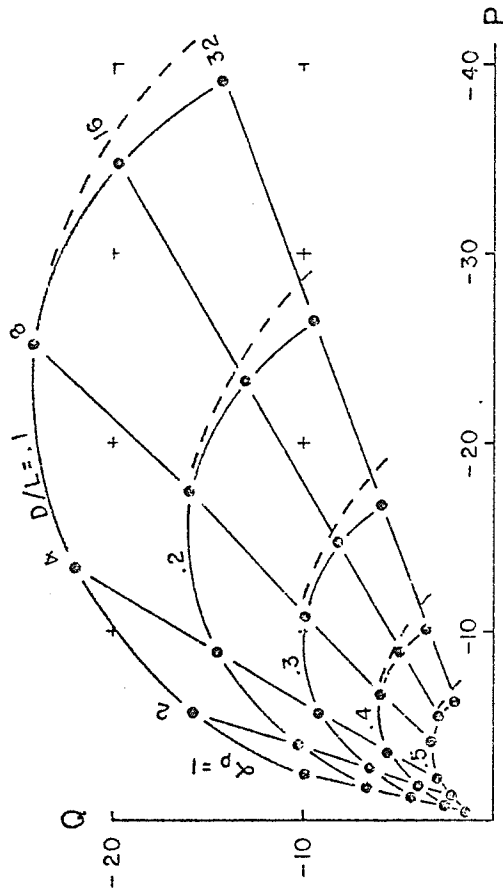
Figure 7-13b  
 HORIZONTAL LOOP RESPONSE  
 LARGE VERTICAL CONDUCTOR  
 IN A

TWO-LAYER EARTH

$$\alpha_p = \mu \omega \sigma_1 l$$

$$\alpha_H = \mu \omega \sigma_2 l^2 = .25$$

$$\alpha_L = \mu \omega \sigma_2 l = .125$$



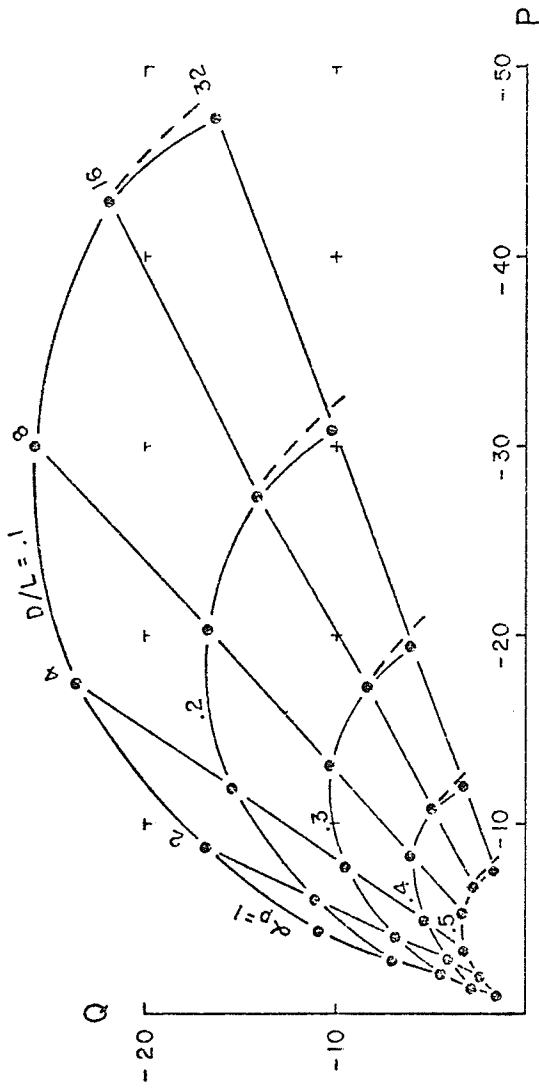
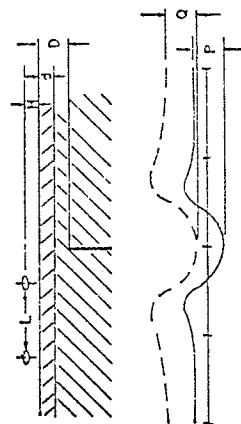


Figure 7-13c  
 HORIZONTAL LOOP RESPONSE  
 LARGE VERTICAL CONDUCTOR

IN A

TWO-LAYER EARTH

- $\alpha_p = j\omega\sigma_1 L$
- $\alpha_H = j\omega\sigma_2 L^2 = .5$
- $\alpha_L = j\omega\sigma_2 L = .25$





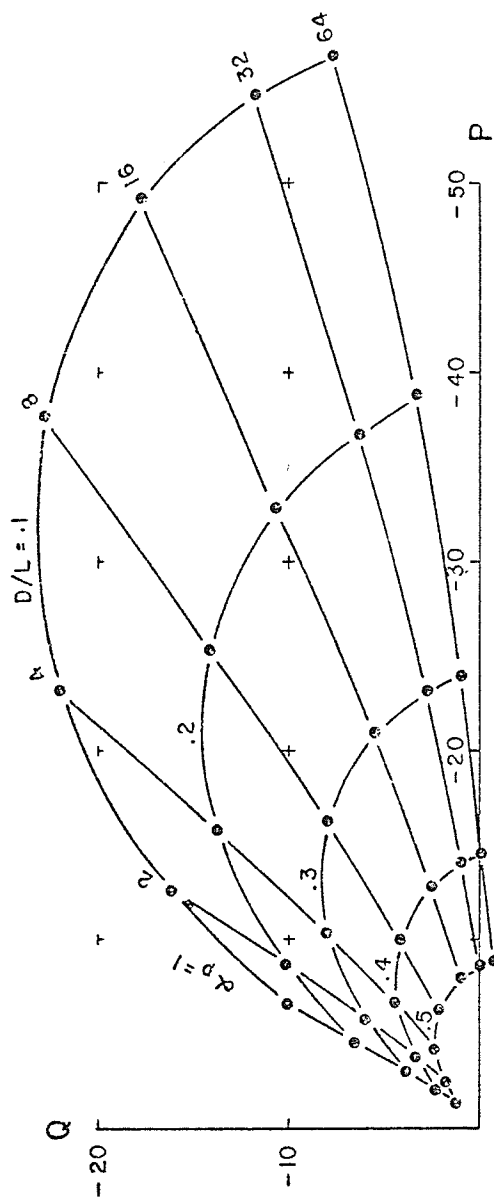


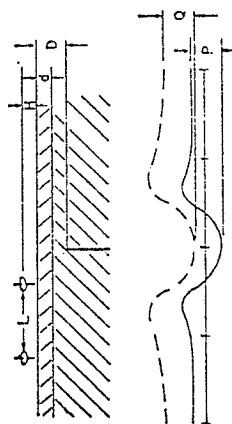
Figure 7-13d  
 HORIZONTAL LOOP RESPONSE  
 LARGE VERTICAL CONDUCTOR  
 IN A

TWO-LAYER EARTH

$$\alpha_p = \mu_1 \omega \sigma_1 l$$

$$\alpha_H = \mu_1 \omega \sigma_1 l^2 = 1$$

$$\alpha_L = \mu_1 \omega \sigma_1 l = .5$$



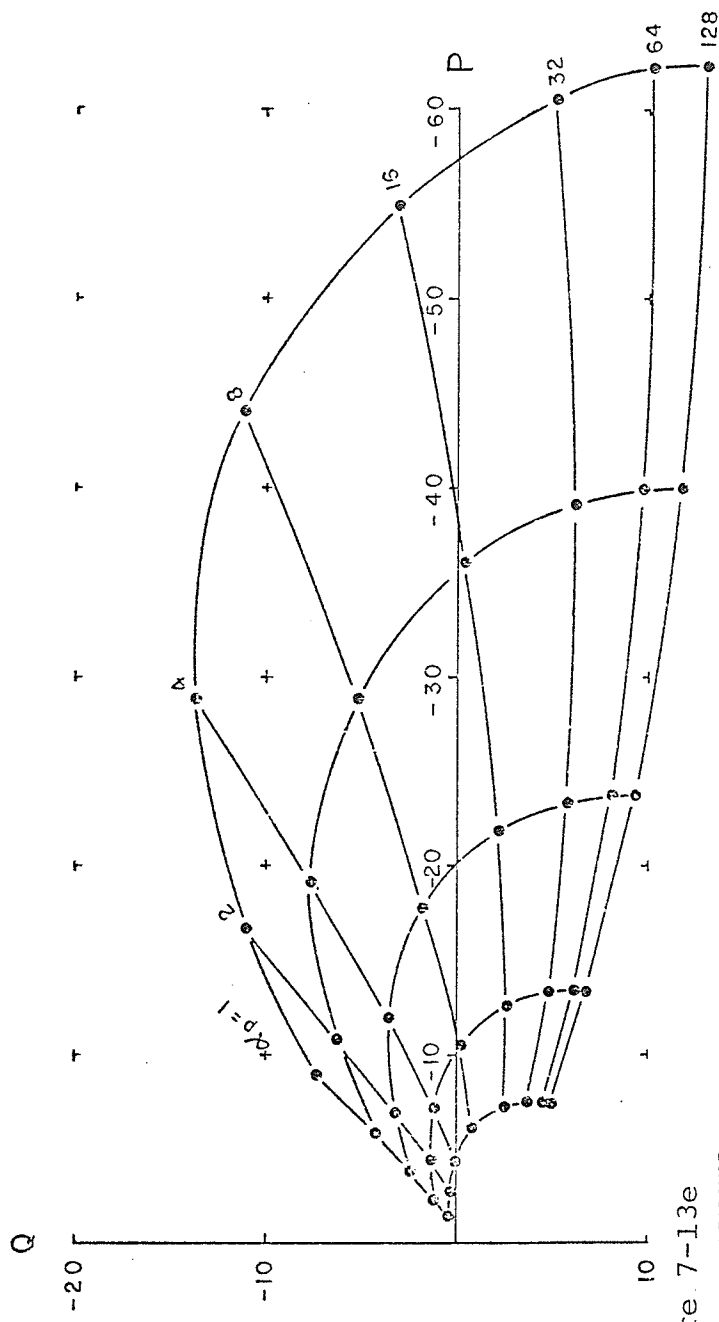


Figure 7-13e

HORIZONTAL LOOP RESPONSE  
LARGE VERTICAL CONDUCTOR

IN A

TWO-LAYER EARTH

$$\alpha_p = \mu_1 \omega \sigma_1 l$$

$$\alpha_H = \mu_1 \omega \sigma_1 l^2 = 2$$

$$\alpha_L = \mu_1 \omega \sigma_1 l = 1$$

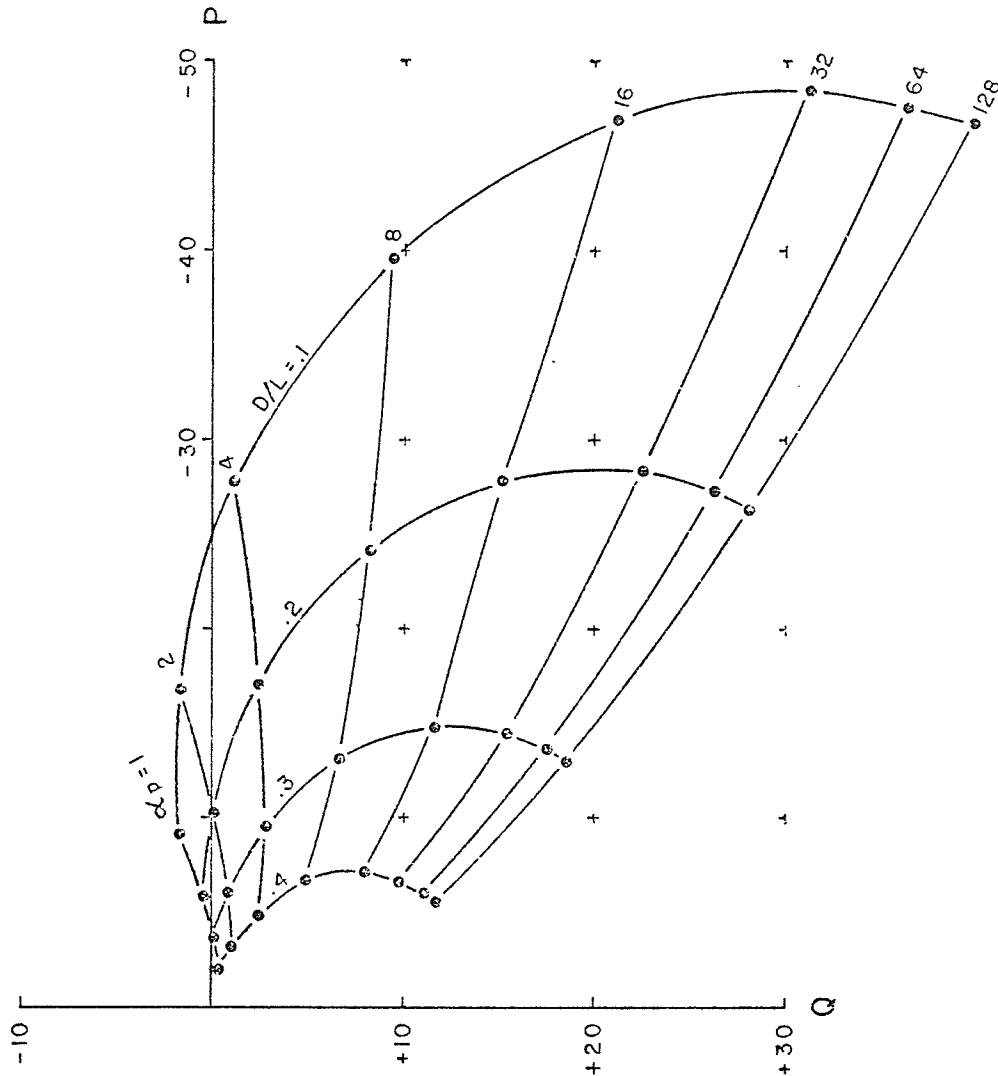


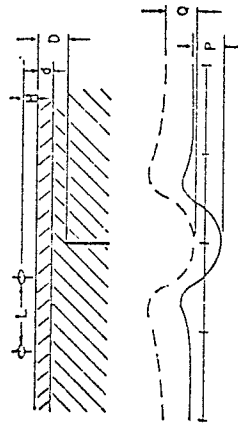
Figure 7-13f  
 HORIZONTAL LOOP RESPONSE  
 LARGE VERTICAL CONDUCTOR

IN A  
 TWO-LAYER EARTH

$$\alpha_p = H W \sigma t l$$

$$\alpha_H = H W \sigma l^2 = 4$$

$$\alpha_L = H W \sigma l L = 2$$



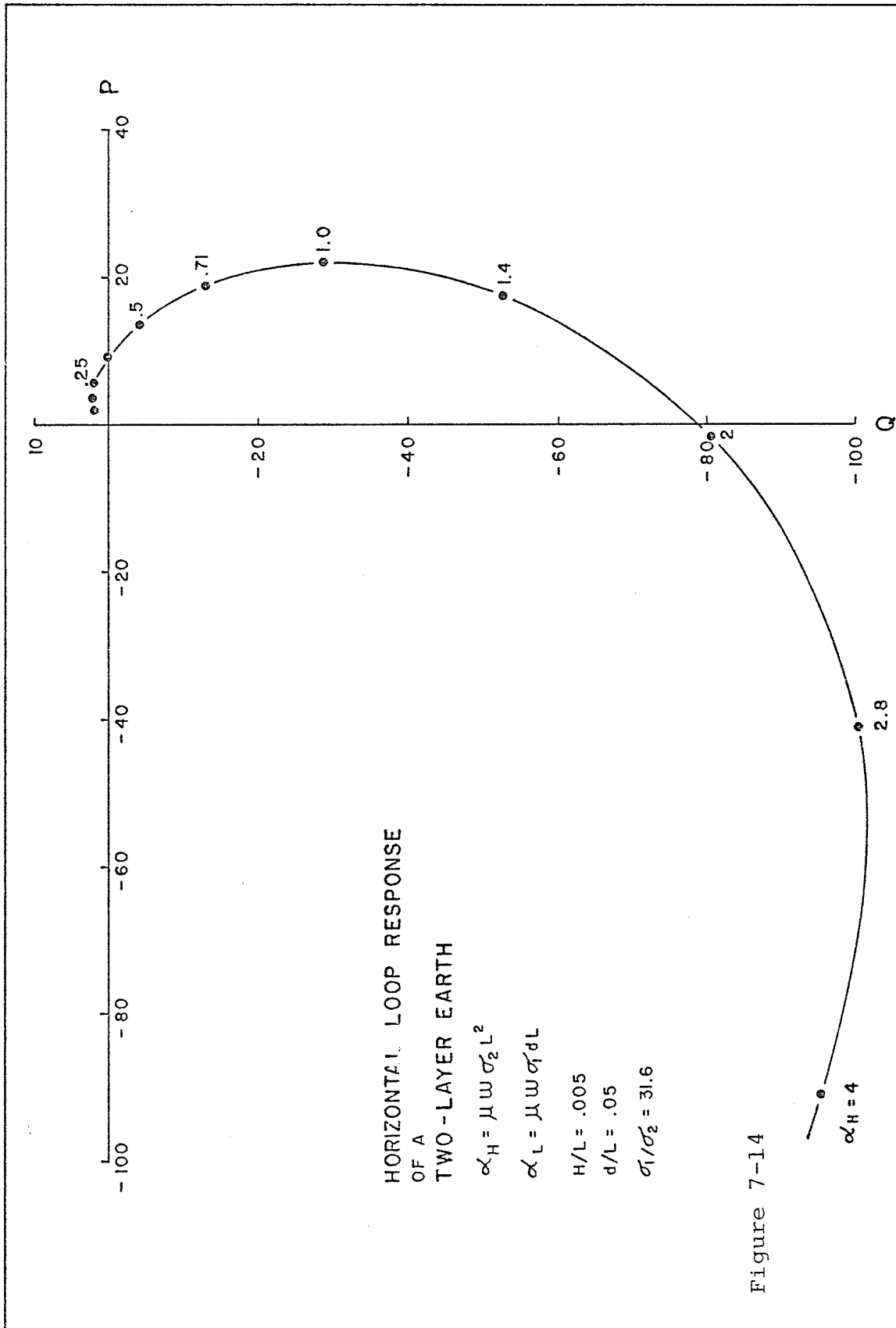


Figure 7-14

Figure 7-15a

HORIZONTAL LOOP RESPONSE  
LARGE VERTICAL CONDUCTOR

IN A

TWO-LAYER EARTH

$$\alpha_p = \mu \omega \sigma_1 L$$

$$\alpha_H = \mu \omega \sigma_2 L^2 = .125$$

$$\alpha_L = \mu \omega \sigma_{dl} = .20$$

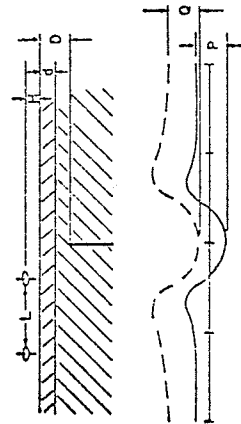
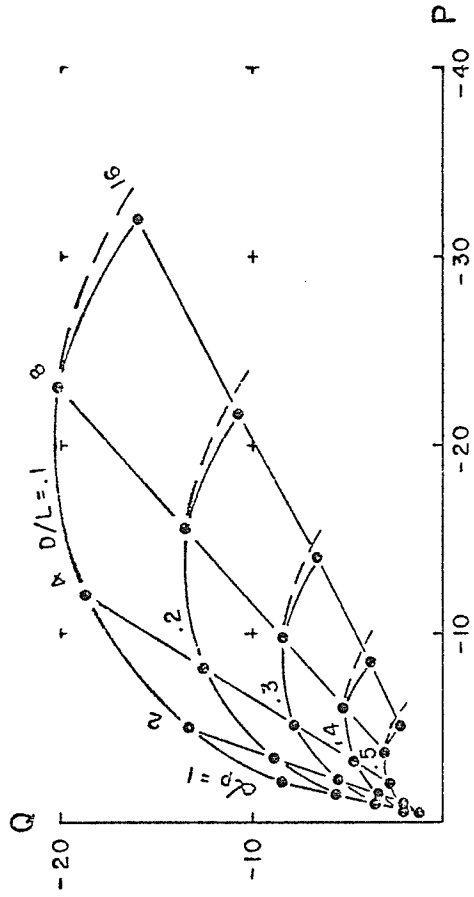


Figure 7-15b

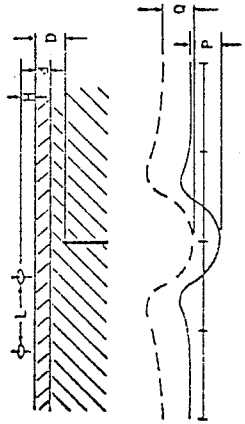
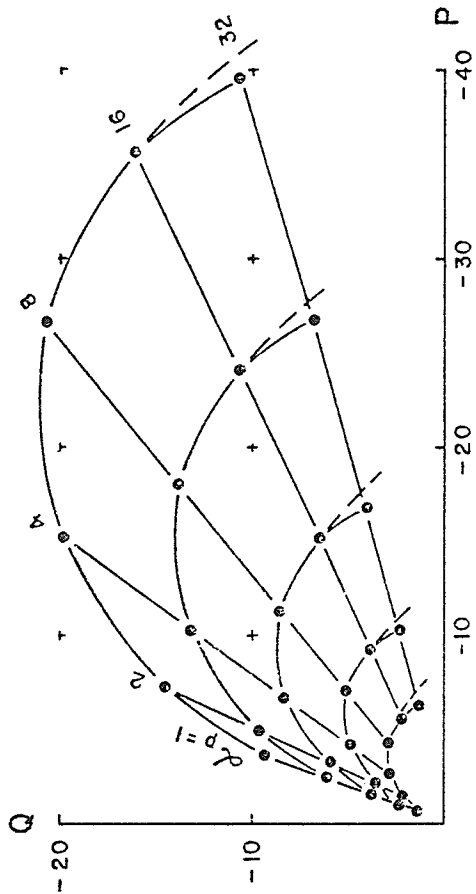
HORIZONTAL LOOP RESPONSE  
LARGE VERTICAL CONDUCTOR

IN A  
TWO-LAYER EARTH

$$\alpha_p = \mu \omega \sigma_1 l$$

$$\alpha_H = \mu \omega \sigma_2 l^2 = .25$$

$$\alpha_L = \mu \omega \sigma_2 l = .40$$



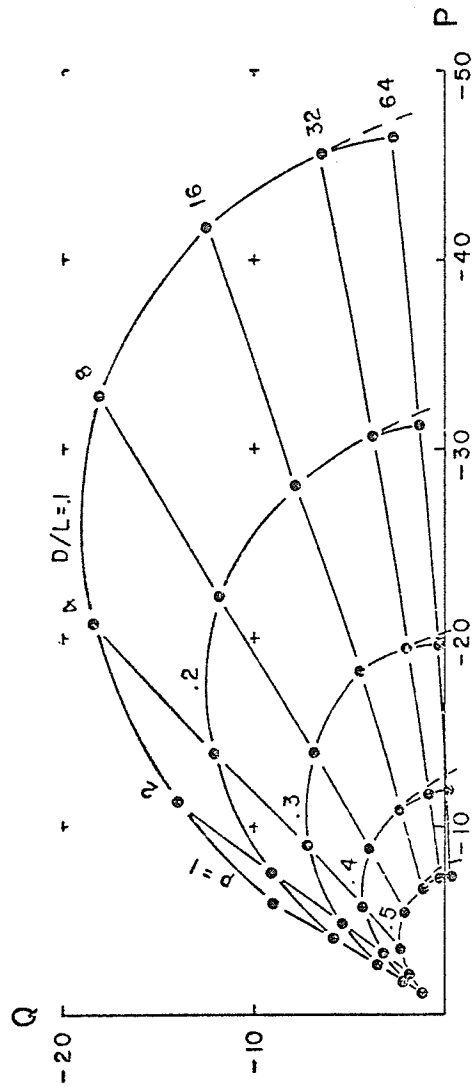
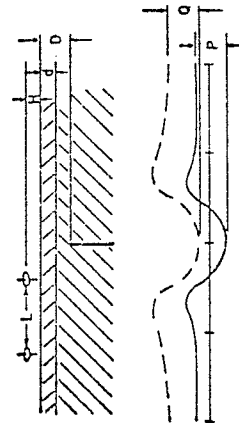


Figure 7-15c

HORIZONTAL LOOP RESPONSE  
LARGE VERTICAL CONDUCTOR

IN A  
TWO-LAYER EARTH

- $\alpha_p = \mu \omega \sigma_1 L$
- $\alpha_H = \mu \omega \sigma_2 L = .5$
- $\alpha_L = \mu \omega \sigma_2 L = .8$



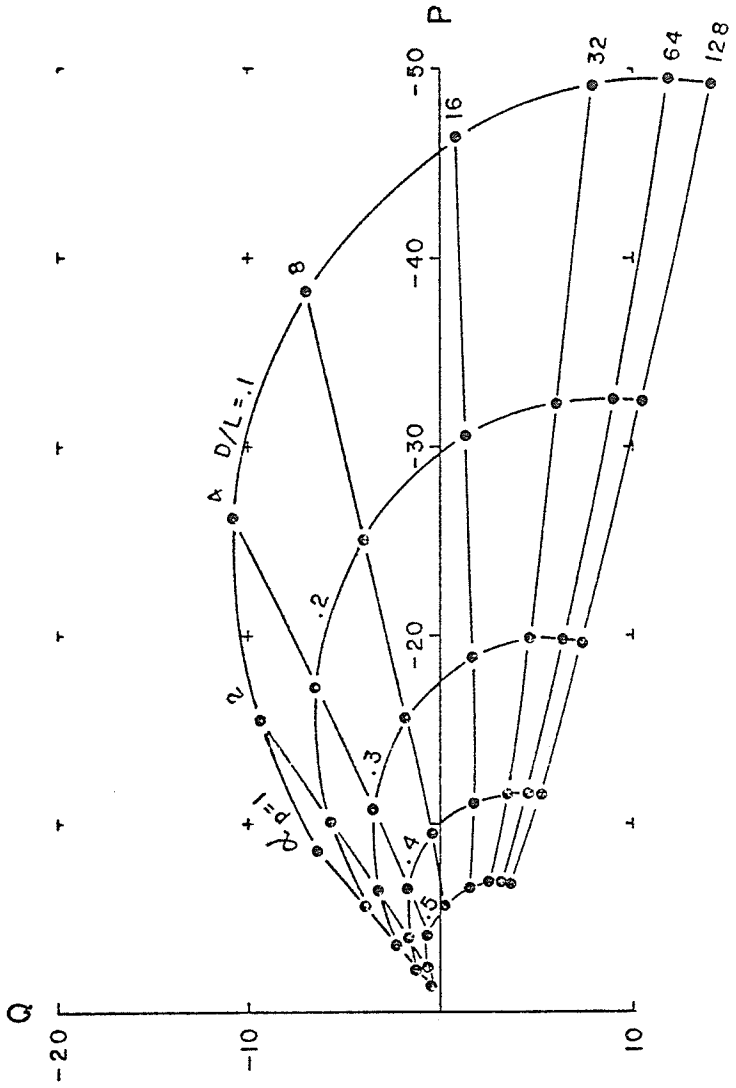


Figure 7-15d

HORIZONTAL LOOP RESPONSE  
LARGE VERTICAL CONDUCTOR

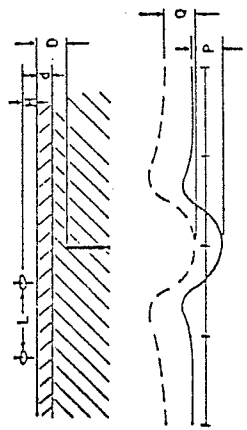
IN A

TWO-LAYER EARTH

$$\alpha_p = \mu_1 \omega \sigma_1^2 L$$

$$\alpha_H = \mu_1 \omega \sigma_1^2 \cdot 1$$

$$\alpha_L = \mu_1 \omega \sigma_1 L \cdot 1.6$$





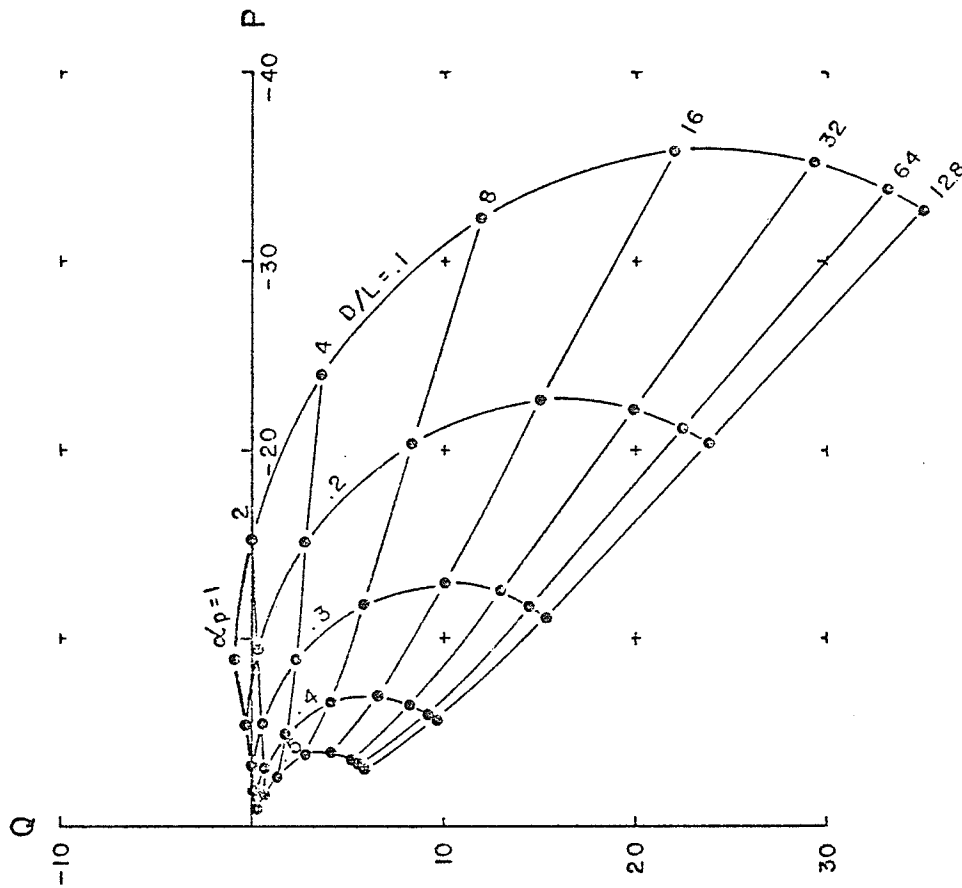


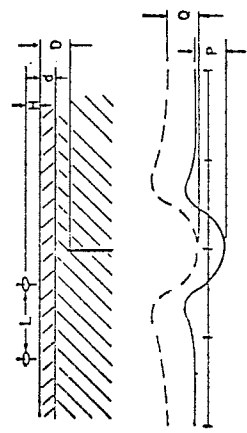
Figure 7-15e  
 HORIZONTAL LOOP RESPONSE  
 LARGE VERTICAL CONDUCTOR

IN A  
 TWO-LAYER EARTH

$$\alpha_p = \mu \omega \sigma_1 L$$

$$\alpha_H = \mu \omega \sigma_2^2 = 2$$

$$\alpha_L = \mu \omega \sigma_2 L = 3.2$$



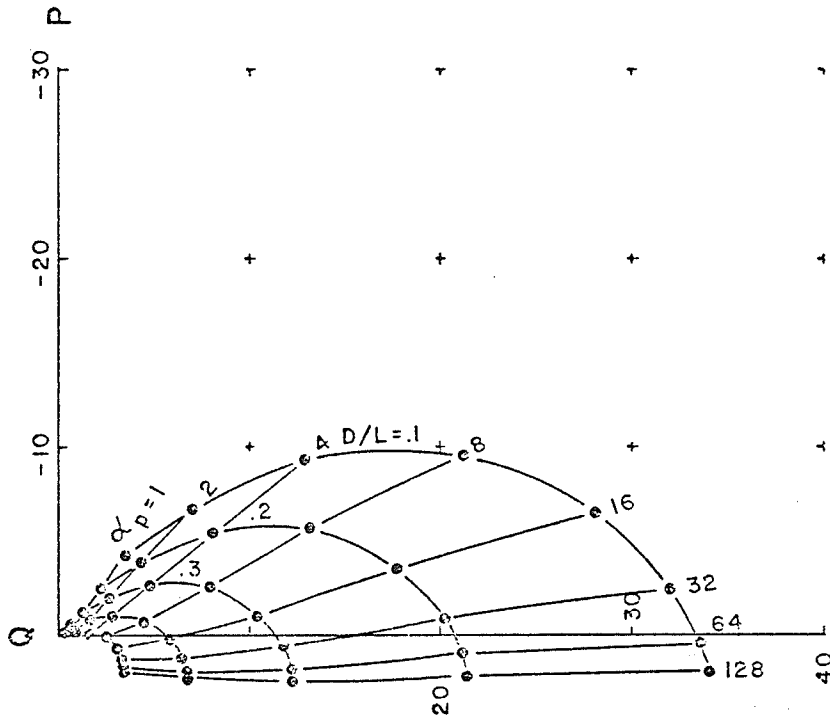


Figure 7-15f

HORIZONTAL LOOP RESPONSE  
LARGE VERTICAL CONDUCTOR

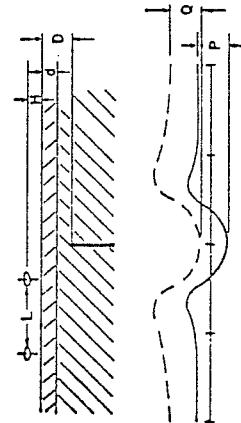
IN A

TWO-LAYER EARTH

$$\alpha_p = \mu_1 \omega \sigma_1 L$$

$$\alpha_H = \mu_1 \omega \sigma_2 L^2 = 4$$

$$\alpha_L = \mu_1 \omega \sigma_2 L = 6.3$$



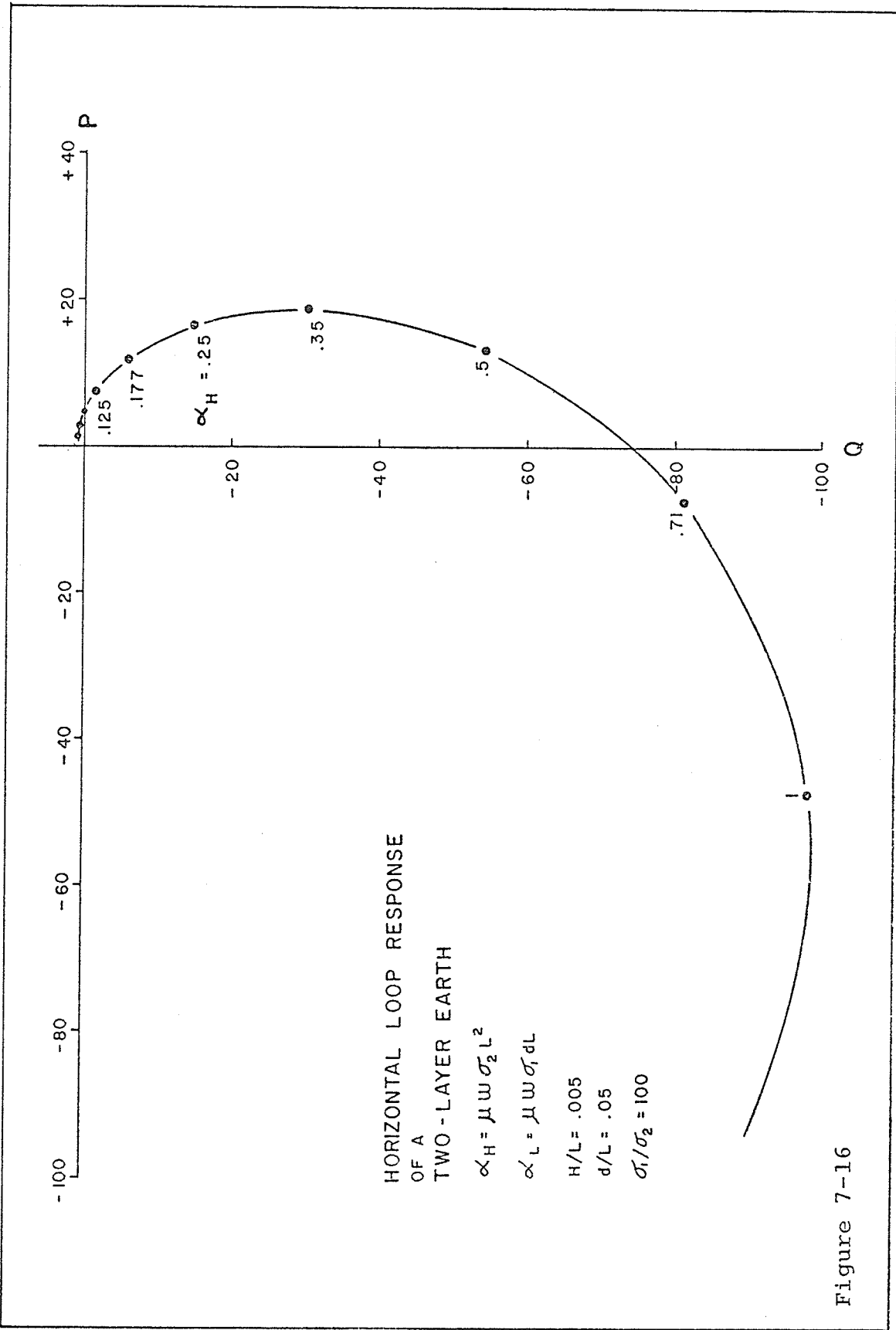


Figure 7-16

Figure 7-17a

HORIZONTAL LOOP RESPONSE  
LARGE VERTICAL CONDUCTOR

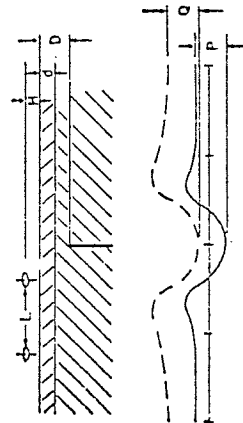
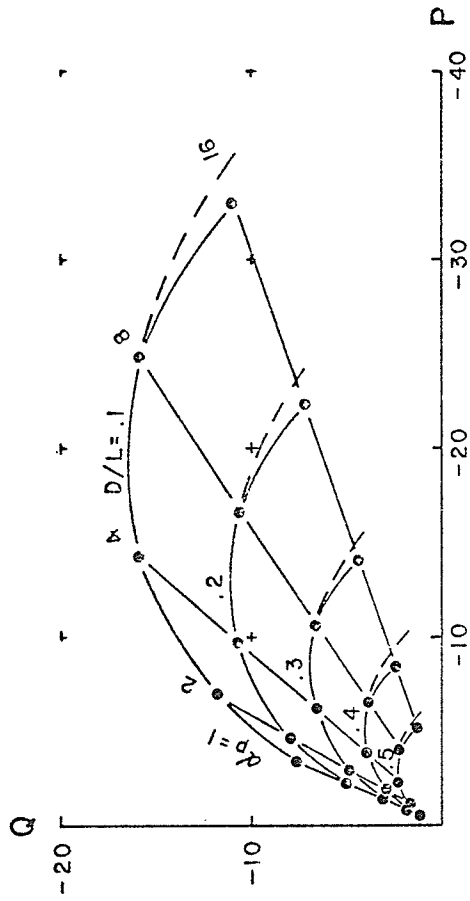
IN A

TWO-LAYER EARTH

$$\alpha_p = \mu_1 \omega \sigma_1 t L$$

$$\alpha_H = \mu_1 \omega \sigma_1^2 = .125$$

$$\alpha_L = \mu_1 \omega \sigma_2 t L = .625$$



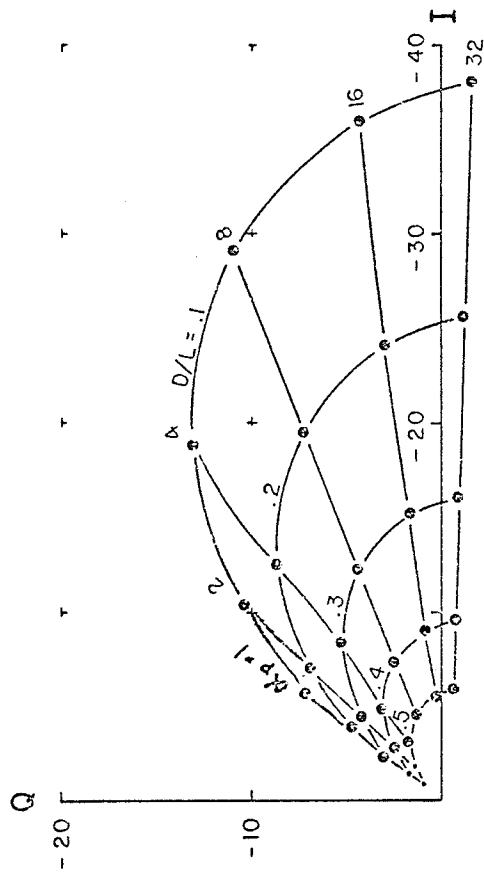
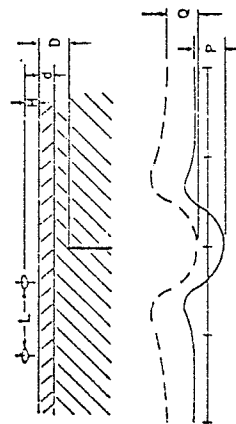


Figure 7-17b  
 HORIZONTAL LOOP RESPONSE  
 LARGE VERTICAL CONDUCTOR  
 IN A  
 TWO-LAYER EARTH

$$\alpha_p = \mu_0 \omega \sigma_1 L$$

$$\alpha_H = \mu_0 \omega \sigma_2 L^2 = .25$$

$$\alpha_L = \mu_0 \omega \sigma_2 L = 1.25$$



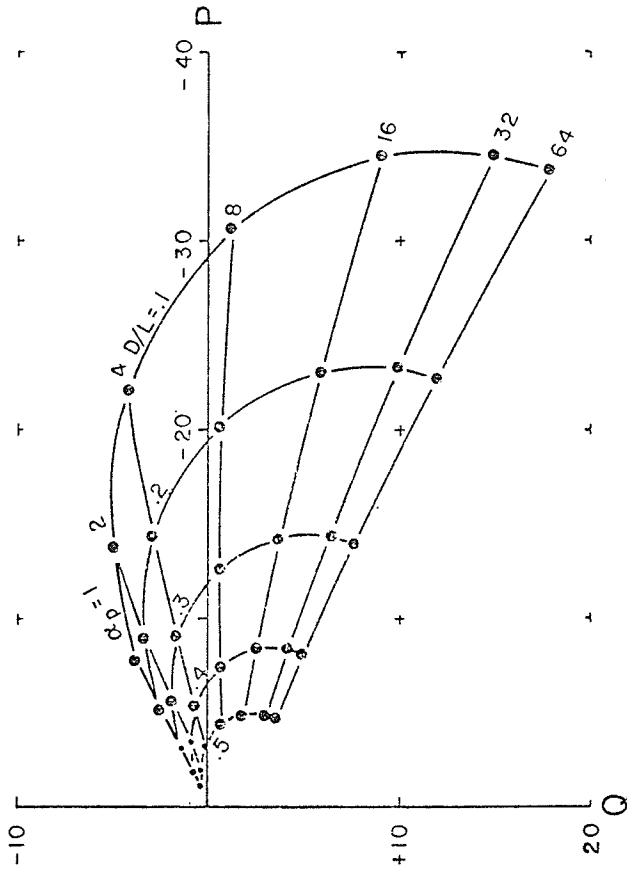


Figure 7-17c  
 HORIZONTAL LOOP RESPONSE  
 LARGE VERTICAL CONDUCTOR

IN A  
 TWO-LAYER EARTH

$$\alpha_p = \mu_1 \omega \sigma_1 L$$

$$\alpha_H = \mu_1 \omega \sigma_1 L^2 = .5$$

$$\alpha_L = \mu_1 \omega \sigma_2 L = 2.5$$

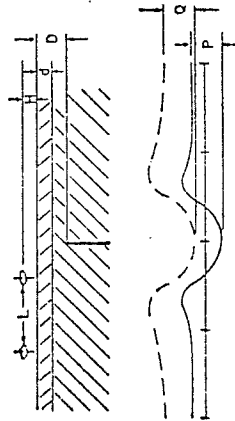


Figure 7-17d  
 HORIZONTAL LOOP RESPONSE  
 LARGE VERTICAL CONDUCTOR

IN A

TWO-LAYER EARTH

$$\alpha_p = \mu_1 \omega \sigma_1 t$$

$$\alpha_H = \mu_1 \omega \sigma_1 L^2 = 1$$

$$\alpha_L = \mu_1 \omega \sigma_1 d_L = 5$$

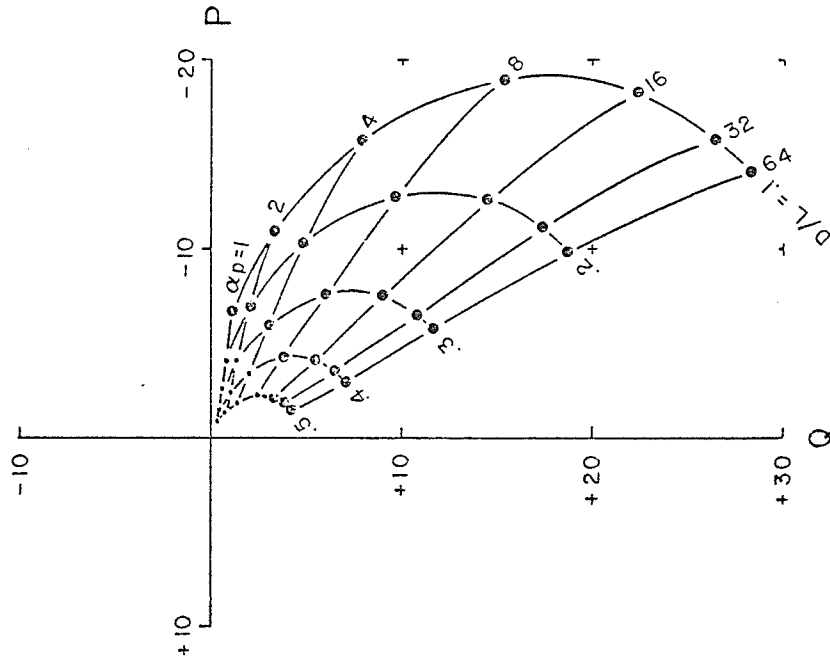
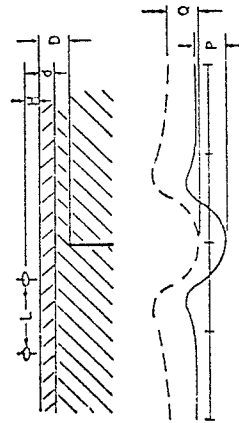


Figure 7-17e  
 HORIZONTAL LOOP RESPONSE  
 LARGE VERTICAL CONDUCTOR

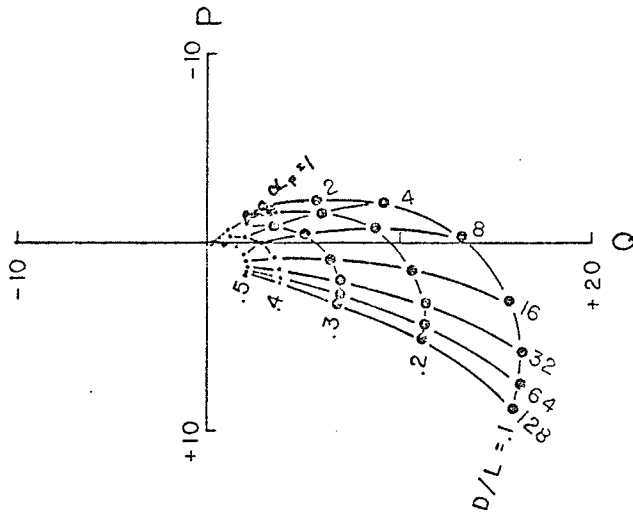
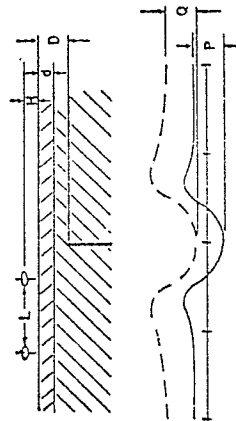
IN A

TWO-LAYER EARTH

$$\alpha_p = \mu \epsilon \omega \sigma t L$$

$$\alpha_H = \mu \epsilon \omega \sigma L^2 = 2$$

$$\alpha_L = \mu \epsilon \omega \sigma t L = 10$$





conductivity increases and reach a plateau as inductive saturation sets in. For certain extreme values of  $\alpha_P/\alpha_H$  the in-phase current was seen to decrease (after initially increasing) in a qualitatively unacceptable manner. There being no physical justification for such behaviour, this decrease in current amplitude was taken as a signal for invalid solutions. Earlier trials at even larger  $\alpha_P/\alpha_H$  values showed that this behaviour was the onset of a major breakdown in the solution.

Table 7-1a was created in an attempt to map out those values of the various parameters which lead to unacceptable solutions. Using a plate of dimensions 6 x 3 x 0.01 meters and a frequency of 1777 hertz, the horizontal loop peak anomaly values ( $L=2m$ ) were computed for various values of host and plate conductivities. The plate depth was  $0.1L$ , and the coil height above the surface was  $0.005L$ . The  $\alpha_H=0$  column of Table 7-1a gives the in-phase and quadrature response for the plate in free space and was generated using program PLATE (A. V. Dyck, 1980). Subsequent columns to the right are results for the same plate in a host of increasing conductivity. Considering column  $\alpha_H=.062$ , it is seen that the modulus,  $(P^2+Q^2)^{\frac{1}{2}}$ , of the anomaly for  $\alpha_P>8$  is less than the modulus for corresponding plates in free space. For the  $\alpha_H=.125$  column, this occurs for  $\alpha_P>16$ , and for  $\alpha_H=.25$  it is true for  $\alpha_P>32$ . This examination shows that the result is obviously in error when  $\alpha_P/\alpha_H>64$ . For higher values of  $\alpha_H$ , inductive saturation sets in before  $\alpha_P/\alpha_H$  exceeds 64. Figure 7-18 displays the moduli of the peak anomaly values given in

TABLE 7-1a

Peak Anomaly Values for the Free Space Host  
Compared with Conductive Half-Space Host

$\alpha_P \backslash \alpha_H$	0		.062		.125		.25		.5		1	
	P	Q	P	Q	P	Q	P	Q	P	Q	P	Q
1	0.5	3.9	0.8	5.0	100	5.7	1.5	6.6	2.3	7.3	3.4	7.3
2	2.1	7.2	2.6	8.5	2.8	9.4	3.5	10.6	5.0	11.7	7.0	11.9
4	6.5	11.7	7.8	12.5	7.8	13.5	8.6	15.0	10.6	16.6	13.8	16.8
8	14.5	14.3	16.2	12.9	15.8	14.4	16.6	16.6	19.1	18.6	23.8	18.9
16	22.9	13.0	22.6	8.7	22.2	11.1	23.3	13.8	26.4	16.4	31.9	16.6
32	28.7	9.3	24.9	4.4	24.9	7.2	16.2	10.1	30.0	12.9	36.3	12.8
64	31.6	5.5	25.3	1.7	25.6	4.6	27.2	7.7	31.3	10.5	38.1	10.1
128	32.7	2.9	--	--	--	--	27.6	6.3	31.8	9.1	38.8	8.6

TABLE 7-1b

Reciprocity Error Estimates for Corresponding  
Peak Anomaly Values of Table 1a

$\alpha_P \backslash \alpha_H$	0		.062		.125		.25		.5		1	
	P	Q	P	Q	P	Q	P	Q	P	Q	P	Q
1	--	--	0.4	0.2	0.1	0.03	0.03	0.09	0.04	0.2	0.06	0.5
2	--	--	1.0	0.5	0.6	0.1	0.3	0.01	0.07	0.3	0.06	1.0
4	--	--	2.0	1.0	1.0	0.2	1.0	0.04	0.3	0.7	0.05	3.0
8	--	--	3.0	0.3	2.0	0.3	2.0	1.0	0.4	2.0	0.2	5.0
16	--	--	3.0	0.1	2.0	1.0	1.0	2.0	0.09	3.0	0.7	4.0
32	--	--	3.0	1.0	2.0	1.0	0.6	3.0	0.3	4.0	1.0	3.0
64	--	--	3.0	1.0	1.0	2.0	0.4	3.0	0.5	4.0	1.0	2.0
128	--	--	--	--	--	--	0.3	3.0	0.6	4.0	1.0	2.0

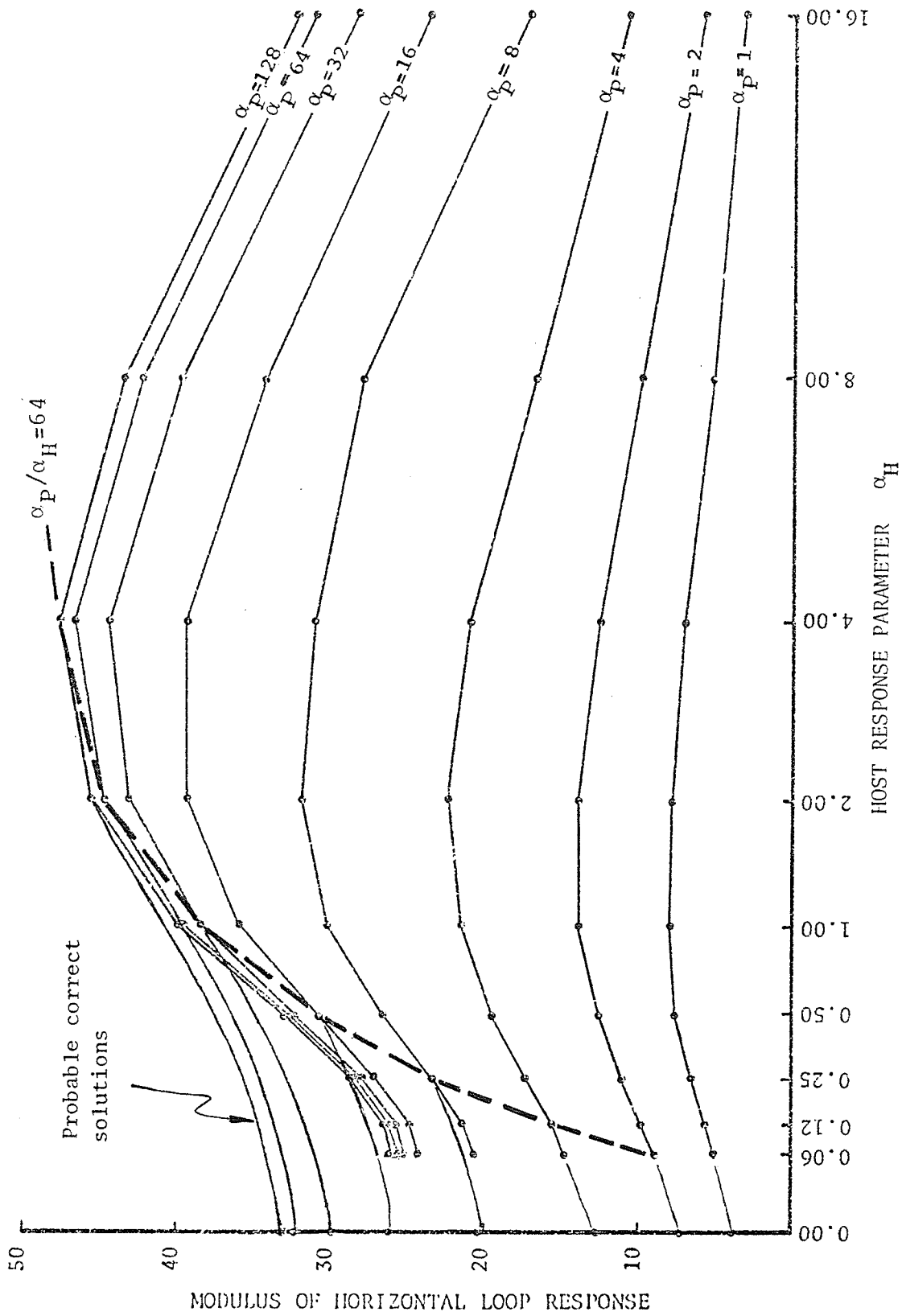


Figure 7-18 Evidence for Numerical Breakdown at High Conductivity Contrasts

Table 7-1a, and also includes moduli for the anomalies generated by plates in more conductive hosts ( $\alpha_H=2,4,8,16$ ).

Thus there is a tendency for the program to produce anomalies of inadequate strength on the one hand, while there is a physical need for anomaly enhancement on the other. Assuming that the free space anomalies generated by program PLATE are correct, then it is certain that when  $\alpha_P/\alpha_H > 64$  and  $\alpha_H < 0.5$ , the results are invalid. It cannot be said that for other values of  $\alpha_H$  and  $\alpha_P/\alpha_H$  the results are valid, but only that they do not obviously violate the physical requirements.

Knowing the asymptotic anomaly values for vanishing host conductivities from the results of program PLATE, and having some confidence in calculations for moderate values of  $\alpha_P/\alpha_H$ , an interpolation procedure could be used to guess at the response for conductive plates in resistive media. However, a more plausible approach is suggested in Section 8.2.

Table 7-1b gives the reciprocity error estimates for each result (except for column  $\alpha_P=0$ ) quoted in Table 7-1a. These error estimates do not appear to be worse for the cases  $\alpha_P/\alpha_H > 64$ .

### 7.5 Convergence of the Solution

Provided that the test functions are chosen with some regard for the physical nature of the solution, it is reasonable to expect that as the number of test functions used to approximate the true solution increases, the approximation

will improve, or at least converge to a stationary value. To test the results quoted in earlier sections, a small number of horizontal loop responses were computed for a wide range of parameters: two plate conductivities (strong and moderate), two plate depths (shallow and deep), and two background conductivities (poor and moderate). The peak anomaly values are given in Table 7-2a, and it is apparent that in most cases the computed response would not change significantly if the number of test functions were increased beyond twelve. The poorest convergence occurs for highly conductive plates, consistent with the implications of Section 7.4.

The tests summarized in Table 7-2a included two solutions ( $\alpha_p=64$ ,  $\alpha_H=0.25$ ) which were believed to be invalid, based on the results of Section 7.4. It was hoped that this convergence test would fail in a more spectacular manner, providing a signal for invalid solutions. It seems, rather, that the solution still tends to converge, but converges to an invalid result.

For each computed response in Table 7-2a, the error estimated using the reciprocity test is given in Table 7-2b. It is apparent that the errors improve with an increase in the number of test functions and that more than twelve test functions will yield little return.

That the reciprocity error estimates steadily decrease with increases in the number of test functions even when the solution is known to converge to an invalid result ( $\alpha_p=64$ ,  $\alpha_H=0.25$ ), suggests that the reciprocity test may be independent of the type of solution breakdown (see Section 7.4) evident

TABLE 7-2a

Peak Anomaly Values for Increasing Numbers of  
Test Functions in the Solution

Number of Test Functions for Each Vector Component		2		4		8		12		
Match Point Array (YxZ)		1x2		2x2		2x4		3x4		
$\alpha_H$	d/L	$\alpha_P$	P	Q	P	Q	P	Q	P	Q
0.25	0.1	4	-3.7	-7.1	-11.0	-14.2	-11.8	-20.6	-12.8	-22.8
		64	-7.5	-8.4	-21.8	-3.9	-35.6	-10.4	-40.5	-11.5
	0.4	4	-1.0	-2.1	-2.6	-3.4	-3.3	-5.5	-3.4	-5.7
		64	-1.7	-2.6	-5.6	-1.6	-10.0	-3.0	-10.4	-2.9
2.00	0.1	4	-11.9	-5.7	-20.3	-12.8	-23.7	-21.0	-25.4	-24.1
		64	-22.4	-0.4	-39.2	-2.2	-61.6	-8.4	-67.8	-10.8
	0.4	4	-3.8	-0.6	-5.3	-1.4	-7.0	-3.5	-7.2	-3.7
		64	-6.5	+1.7	-8.9	-2.3	-15.9	+2.2	-16.4	+2.1

TABLE 7-2b

Reciprocity Error Estimates in Percent for Increasing  
Numbers of Test Functions in the Solution

Number of Test Functions for Each Vector Component		2		4		8		12		
Match Point Array (YxZ)		1x2		2x2		2x4		3x4		
$\alpha_H$	d/L	$\alpha_P$	P	Q	P	Q	P	Q	P	Q
0.25	0.1	4	21	26	11	7	1	1	1	0.5
		64	28	28	11	8	1	0.3	1	2
	0.4	4	10	13	7	6	0.02	0.6	0.5	0.5
		64	14	15	8	0.1	0.2	1	0.2	3
2.00	0.1	4	17	5	4	1	0.8	0.2	0.05	0.2
		64	21	14	5	4	2	1	0.7	0.1
	0.4	4	7	3	3	1	0.4	0.1	0.4	0.1
		64	6	2	3	3	1.0	0.5	1.0	0.6

when  $\alpha_P/\alpha_H > 64$ . This implication is corroborated by the results given in Table 7-1b. It is tempting to conclude that the reciprocity error estimates are testing a necessary (but not sufficient) aspect of the geometric form of the solution current distribution and that the errors discussed in the preceding section are associated with an ill-conditioned matrix. Although the conditioning of the present matrix is not well understood, earlier attempts to solve the problem (see Section 8.1) showed that the dynamic range of the magnitudes of the matrix eigenvalues becomes extreme when high conductivity contrasts are being modelled.

#### 7.6 Finiteness of the Plate Size

In interpreting survey data, it is important to consider the strike-length and depth-extent of the conductor which caused the anomalous readings. The anomaly caused by a small conductor near the surface could be interpreted as arising from a large conductor at greater depth. The strike-length can usually be inferred from the number of adjacent traverse lines on which the conductor was detected, while effects of limited depth-extent can be seen either in the shape of the anomaly trough (normally flat-bottomed), or in the relative size of anomaly obtained with a different coil separation. Accurate estimates of the conductor depth and  $\sigma t$  cannot be obtained from half-plane Argand diagrams if the causative source is small.

It is generally accepted (Gupta, O.P., 1980) that for plates in a resistive host, noticeable strengthening of hori-

zontal loop anomalies occurs with increasing plate size until the length and width reach  $3L$  and  $2L$  respectively, provided the depth beneath the traverse elevation is not too great. If plates this size can be modelled, then the many field cases where the conductor has great length and depth extent can be interpreted through comparison with the  $3L \times 2L$  plate responses. Furthermore, irregular conductor boundaries can be ignored since they are beyond the region of significant eddy current flow.

To better understand if the  $3L \times 1.5L$  plate results given in Section 7.2 and 7.3 can be used to simulate the response of a semi-infinite half-plane, responses were computed for plates of varying size. The aspect ratio remained constant at  $S/W=2$ , and the strike-length was varied from  $L$  to  $4L$  in steps of  $L/2$ . Parameters with a small number of widely ranging values were chosen:  $\alpha_P=1$  and  $128$ ,  $\alpha_H=0.5$  and  $4$ , and  $d/L=0.1$  and  $0.5$ . The results, summarized in Table 7-3a, initially show rapid changes in the peak anomaly values with increasing plate size. Comparison of columns  $S/L=2.5$  and  $S/L=3$  show greatly diminished rates of change, suggesting that plates  $3L \times 1.5L$  are good approximations to half-plates.

Unfortunately, another effect can be detected for highly conducting plates of size greater than  $S/L=2.5$ , and can only be attributed to numerical failure in the algorithm. The modulus of the peak anomaly values are seen to decrease (in Figure 7-19) if the plate is sufficiently large. It appears that



TABLE 7-3a

Peak Anomaly Values for Plates of Differing Size

Strike Length S/L	1		1.5		2		2.5		3		3.5		4			
	$\alpha_p$	P Q	P	Q	P	Q	P	Q	P	Q	P	Q	P	Q		
0.5	1	-0.8	-5.9	-1.7	-8.8	-2.4	-10.3	-2.9	-11.0	-3.2	-11.2	-3.4	-11.1	-3.5	-10.7	
	128		-20.2	-7.9	-33.4	-12.8	-41.4	-15.1	-45.6	-15.4	-47.0	-14.6	-45.8	-13.3	-43.3	-11.8
	1		--	--	-0.37	-1.2	-0.54	-1.47	-0.66	-1.61	-0.74	-1.66	-0.8	-1.65	-0.83	-1.61
	128		--	--	-5.3	-1.7	-6.5	-2.0	-7.3	-2.0	-7.6	-1.7	-7.5	-1.5	-7.3	-1.2
4.0	1	-6.1	-7.1	-7.7	-7.8	-8.3	-7.8	-8.5	-7.7	-8.5	-7.5	-8.5	-7.1	-8.3	-6.5	
	128		-56.0	-19.0	-79.0	-6.3	-82.0	-4.1	-79.0	+9.2	-75.0	+12.0	-68.0	+12.0	-63.0	+14.0
	1		-0.92	-0.28	-1.17	-0.24	-1.26	-0.18	-1.27	-0.13	-1.26	-0.093	-1.24	-0.05	-1.21	-0.01
	128		-6.8	+1.8	-8.4	+4.7	-8.0	+6.2	-7.1	+6.7	-6.2	+6.7	-5.5	+6.4	-4.8	+6.1

TABLE 7-3b

Reciprocity Error Estimates for Peak Anomaly Values in Table 7-3a

Strike Length S/L	1		1.5		2		2.5		3		3.5		4		
	$\alpha_p$	P Q	P	Q	P	Q	P	Q	P	Q	P	Q	P	Q	
.05	1	.00	.01	.02	.10	.05	.20	.08	.30	--	--	.01	.30	.30	1.0
	128		.30	.50	.40	.60	.70	.50	1.0	--	--	1.0	4.0	2.0	5.0
	1		--	--	.00	.01	.08	.04	.20	--	--	.20	.70	.30	1.0
	128		--	--	.20	1.0	2.0	.40	2.0	--	--	2.0	3.0	2.5	3.0
4.0	1	.01	.00	.09	.00	.21	.00	.30	.00	.10	.01	.50	.01	2.0	0.0
	128		.05	.03	.45	.03	.29	.01	.50	.10	.05	.60	.60	2.0	1.0
	1		.00	.00	.02	.00	.05	.00	.11	.01	.20	.01	.30	.50	.05
	128		.25	.01	.22	.06	.00	.13	.31	.21	.60	.30	1.1	.42	2.0

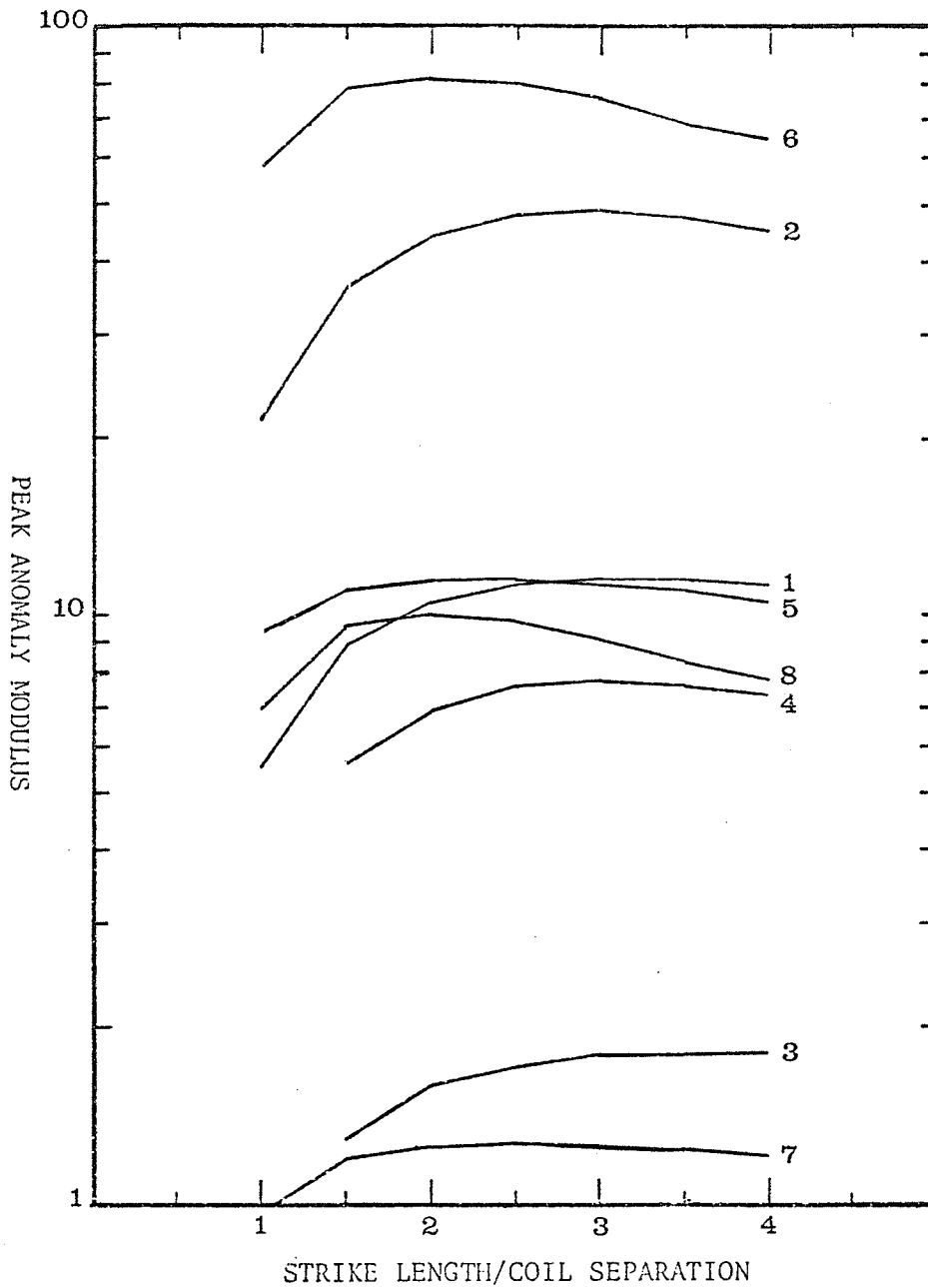


Figure 7-19 Modulus of Peak Anomaly Values for Plates of Different Size. Numeric Designation of Curves Corresponds to Designations in Table 7-3a.

decreases in anomaly modulus with increasing plate size are physically unacceptable. Reduction of the anomaly modulus reflects a reduction in the strength of the scatter current which cannot happen as one removes resistance to current flow. Although  $3L \times 1.5L$  plates are concluded to be good approximations to half-planes, the results suggest that some of the anomaly attenuation problems described in Section 7.4 could be alleviated by recomputing the responses using slightly smaller plates.

Comparing curve 1 with 5, 2 with 6, 3 with 7, and 4 with 8 in Figure 7-11 suggests that a plate in a conductive host need not be as large to appear semi-infinite as the same plate in resistive media.

Table 7-3b gives the reciprocity error estimates for the corresponding peak anomaly values of Table 7-3a. Although the errors increase with plate size they are never strong enough to signal an invalid solution.

### 7.7 Two Case Histories

To estimate the usefulness of the computer program for calculating anomalies due to conductors in a two-layer earth, an attempt was made to interpret some field results discussed by Lajoie and West (1977). The anomaly exhibits enhancement and rotation of a nature described by the phase diagrams in Sections 7.2 and 7.3.

Conductivity layering of the host medium was first estimated using phasor curves (for a layered earth) generated by

Eadie (1979). Minor revisions to this estimate were made after computing a half-dozen layered earth responses for parameters in the vicinity of those estimated from Eadie's work. It was decided that the earth model which is described with its computed response in Table 7-4, would be used to approximate the host media, whose background response estimated from the survey is also given.

Using the 222 hertz survey results and a free space phasor diagram (Nair and others, 1968) gave the results  $d=0.2L$  and  $\alpha_p=12$ . This gives  $\sigma_3 t=46$ . The calculated response over the centre of a 450 x 225 x 0.75 meter plate at a depth of 0.2L for  $L=150m$  is given in Table 7-5 along with the observed field results. The conductivity thickness was revised downward to 23 mho to yield results (Table 7-5) more consistent with observations. Using  $\sigma_2 t=23$ , entire profiles were computed for the five operating frequencies of the Apex Maxmin II Horizontal Loop System and are presented with the field observations in Figure 7-20.

While a better fit of calculated to observed results could probably be achieved with further manipulation of the parameters, it is already apparent that the numerical solution satisfies the basic physical requirements of this geological situation.

As a second case history, a survey reported by Palacky and Sena (1979) produced results which cannot be interpreted with free space phasor curves, but which seem to be consistent with results quoted in Section 7.3. Their target C, survey

TABLE 7-4

Estimated Background (L=150m) and the Computed Response for Earth Parameters  $\sigma_1=.068$ ,  $\sigma_2=.0096$  and Layer Thickness=.05L

Computed Response		Estimated Background		Frequency
P	Q	P	Q	
1.04	1.63	0	0	222
3.09	2.22	+4	+2	444
8.32	0.66	--	--	888
17.82	-10.73	20	-12	1777
19.23	-47.39	23	-47	3555

TABLE 7-5

Field Observations Compared with the Calculated Response for  $\sigma_3 t=62$  and  $\sigma t=31$

Freq. Hz	Calculated $\sigma t=62$		Calculated $\sigma t=31$		Observations	
	P	Q	P	Q	P	Q
222	-20.75	-10.48	-14.58	-13.06	-16	-13
444	-25.07	-7.01	-22.27	-10.64	-20	-10
888	-28.61	-3.70	-27.86	-6.16	--	--
1777	-32.26	+1.75	-31.72	-0.88	-33	+8
3555	-29.14	+16.69	-29.37	15.99	-23	+22

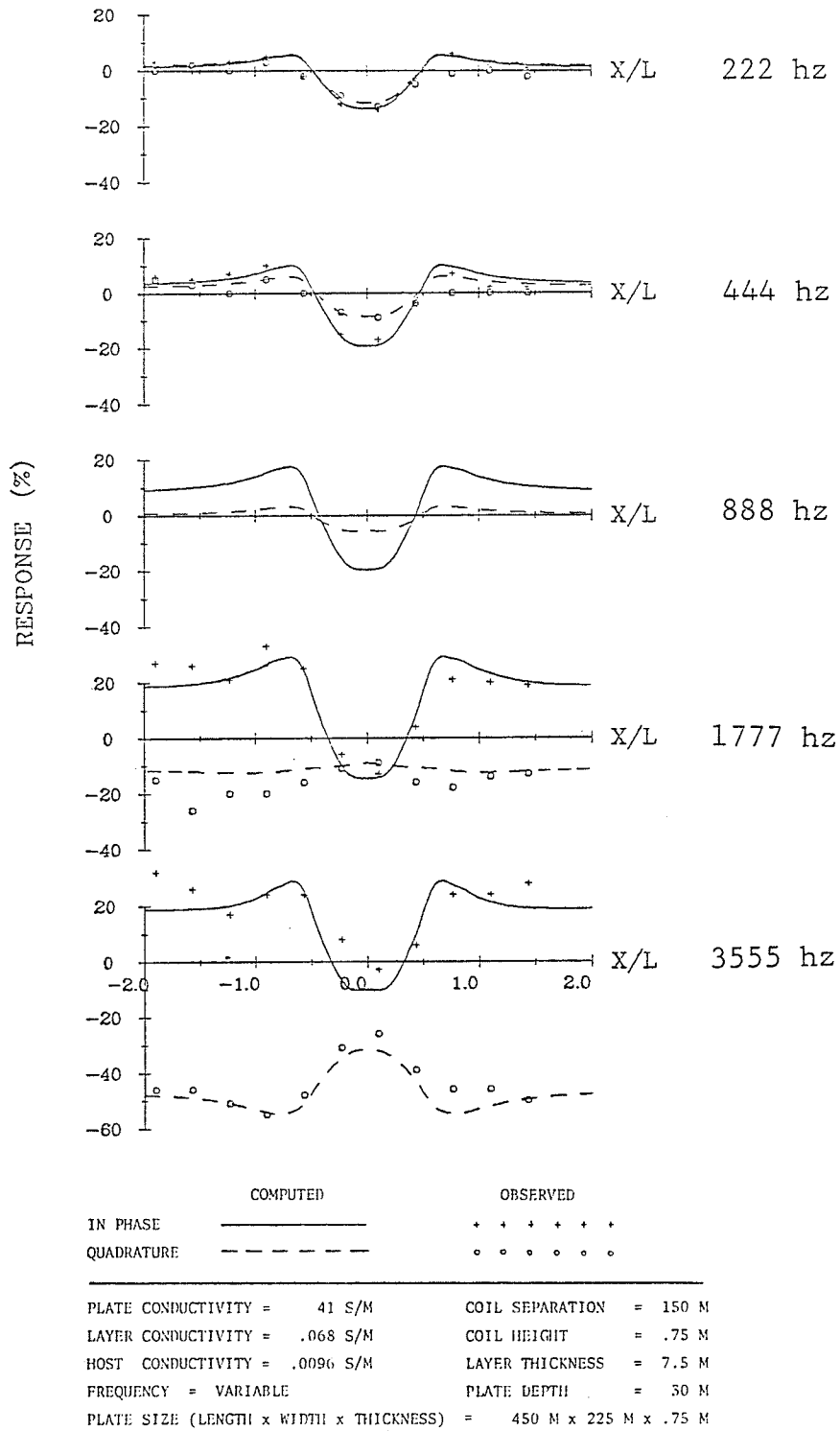


Figure 7-20 Conductive Overburden: A Case History

line B, appears to give maximum deviations from background of  $(P,Q)=(-22, -22)$  at 444 hz. At 1777 hz., the response was  $(P,Q)=(-10, -60)$ . As pointed out by Palacky and Sena (1979), the two responses do not both lie on the same constant depth arc of the free space phasor diagram of Nair et al. (1968). If the low frequency response  $(-22, -22)$  is plotted on Figure 7-7c ( $\alpha_H=.5$ ), it appears that  $\alpha_P=8$  and  $D/L=.17$ . Two octaves higher (where  $\alpha_P=32$  and  $\alpha_H=2$ ) it is seen from Figure 7-7e that the 1777 hz. response would be  $(P,Q )=(-10, -50)$ . The observed values of about  $(-10, -60)$  are considered to be well within the error involved in estimating the background values.

#### 7.8 Comparison of Results with Other Studies

In examining the laboratory results of workers such as Gupta Sarma and Maru (1971), Gaur et al. (1972), Gaur and Verma (1973), C. P. Gupta (1973), and O. P. Gupta (1980), it becomes apparent that analogue models are capable of simulating a somewhat narrow range of scattering parameters. The difficulty lies with the conductivity contrast of the materials available to simulate the earth and the embedded conductor. Metal sheets to model the ore body are generally too conductive, and water containing electrolyte to simulate the earth is (relatively) too resistive to produce significant host effects.

It happens that cases which have been simulated with analogue models are those cases which cannot, in this work, be modelled with confidence. The lowest value of  $\alpha_P/\alpha_H$  found in a literature search was 100, reported by C. P. Gupta (1973),

and exceeds considerably the upper limit of 64 set in Section 7.4.

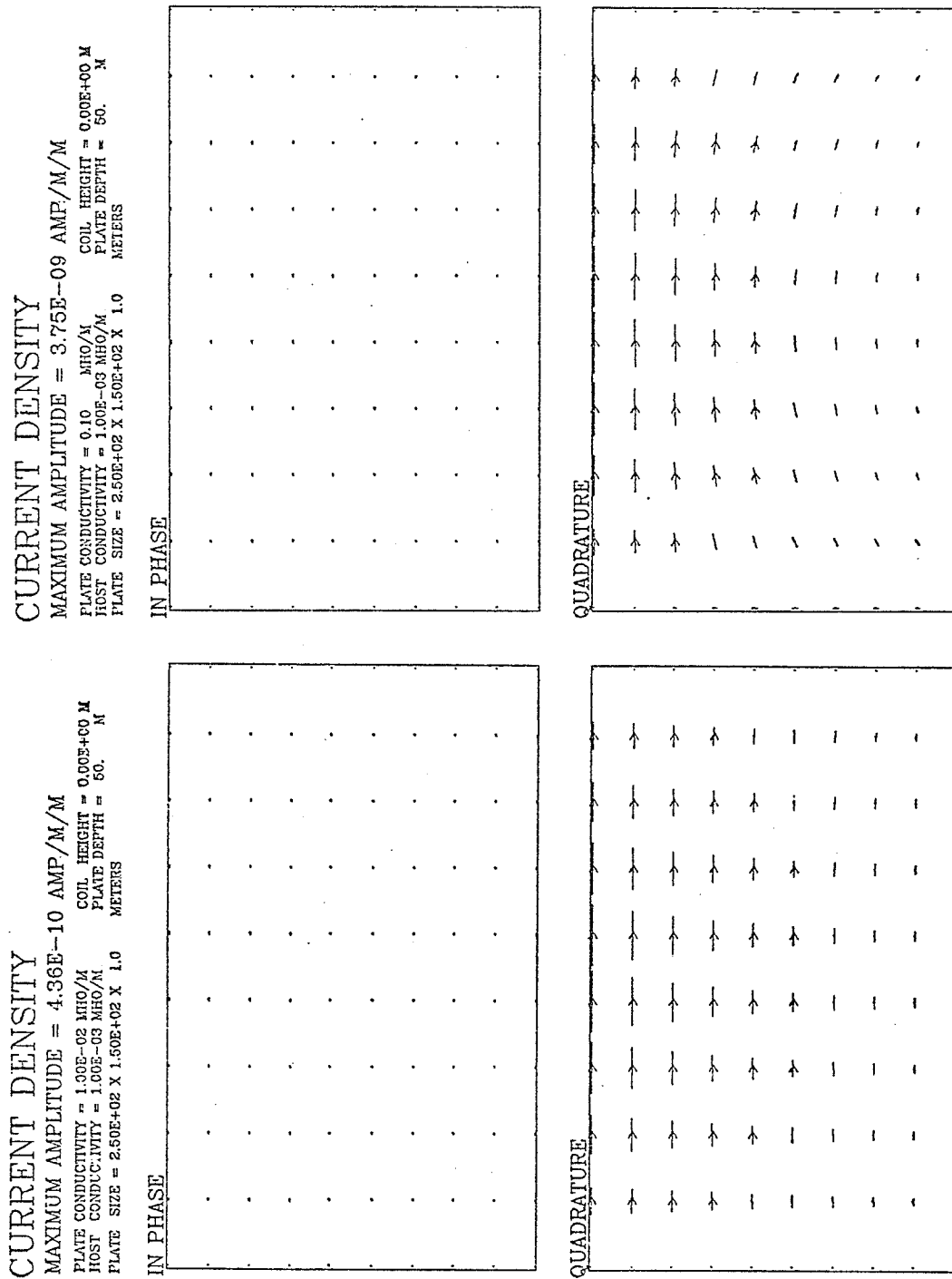
One case modelled by Gupta (1973, p.160) is that of a stainless steel plate of size 1.02m x 0.41m x .00019m, of conductivity  $14 \times 10^5$  s/m, immersed at a depth of .03 m in a medium of conductivity 11.6 s/m. A horizontal loop traverse with an operating frequency of 100 KHz. and a coil height of .07 meters yielded a peak anomaly value of (-16%, -6.6%). The computed response for a plate of size .75m x .5m x .0019m and conductivity  $14 \times 10^4$  s/m and all other parameters the same as in Gupta's model, is (-11%, -3.2%). As expected from the results of Section 7.4, the computed response is too small when  $\alpha_P/\alpha_H > 64$ . From a broader perspective, Gupta's work shows that the initial effects of increasing the host conductivity are counter-clockwise anomaly phase rotation and enhancement of the anomaly magnitude - results which are qualitatively similar to the computed results in Section 7.2.

One means for solving the experimental problem of conductivity contrasts might be to use a fine screen or wire mesh to simulate the conductor, instead of foil or metal plates. While conductivity and thickness would have no meaning independently, an effective  $\sigma t$  product could be measured inductively by doing a scale model horizontal loop traverse in free space. Results could be compared with free space argand diagrams.

Somewhat more amenable for comparison are results generated by Lajoie (1973, p.118) for the eddy currents induced in a plate in conductive infinite space by a vertical magnetic



dipole. The plate has size 250m x 150m x 1m with conductivities .1, 1, 10, 100, 1000 s/m, the host conductivity is .001 s/m and the operating frequency is 1000 Hz. The dipole is 100m from the plane of the plate and 50m above the upper edge; the induced current is displayed in Figures 7-21a to 7-21f and the general form and phase of the solution compares favourably with Lajoie's results. The amplitudes, however, are stronger than those of Lajoie (see Table 7-6); the discrepancy ranging from 16 to 26 percent. The general agreement suggests that the present program may yield valid results at high plate conductivities provided inductive saturation is reached before  $\alpha_p/\alpha_H$  exceeds 64.



b.  $\sigma_3 = .1$

a.  $\sigma_3 = .01$

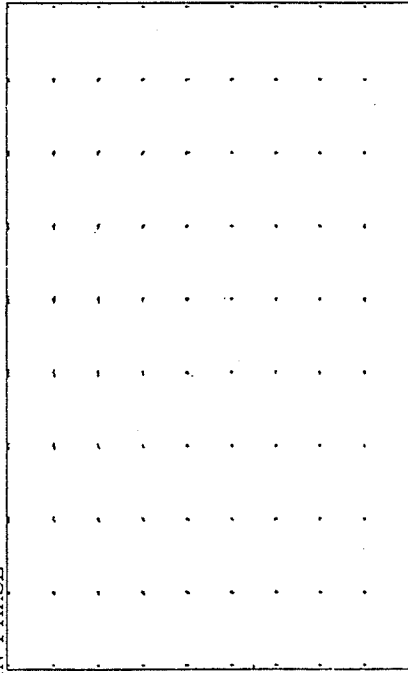
Figure 7-21 Current Densities on Plates of Varying Conductivity Irradiated by a Vertical Magnetic Dipole

### CURRENT DENSITY

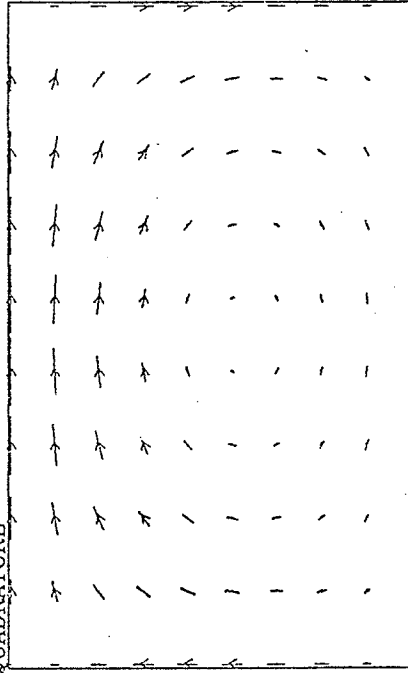
MAXIMUM AMPLITUDE = 2.44E-08 AMP/M/M

PLATE CONDUCTIVITY = 1.0 MHO/M  
HOST CONDUCTIVITY = 1.00E-03 MHO/M  
COIL HEIGHT = 0.00E+00 M  
PLATE DEPTH = 50. M  
PLATE SIZE = 2.50E+02 X 1.50E+02 X 1.0 METERS

IN PHASE



QUADRATURE



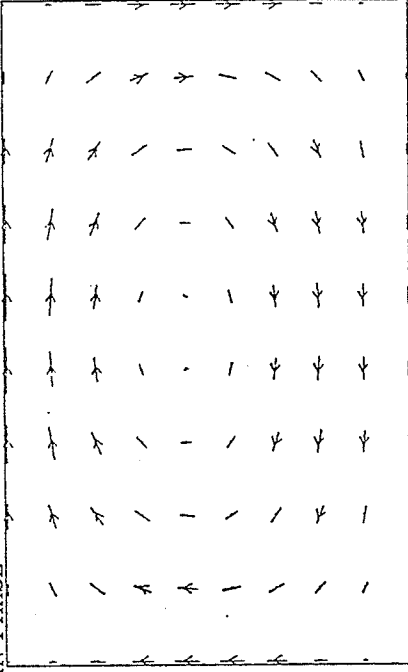
C.  $\sigma_3=1.$

### CURRENT DENSITY

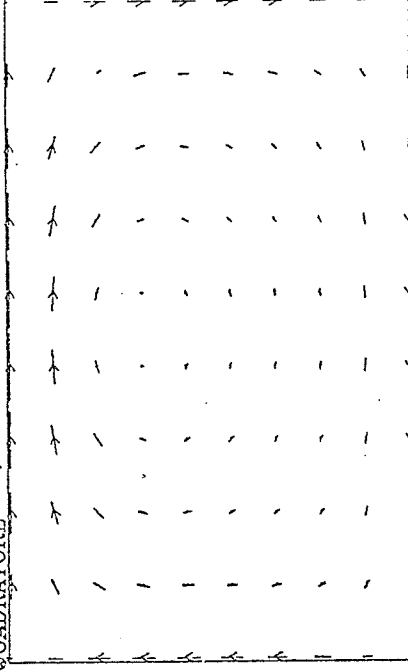
MAXIMUM AMPLITUDE = 1.07E-07 AMP/M/M

PLATE CONDUCTIVITY = 10. MHO/M  
HOST CONDUCTIVITY = 1.00E-03 MHO/M  
COIL HEIGHT = 0.00E+00 M  
PLATE DEPTH = 50. M  
PLATE SIZE = 2.50E+02 X 1.50E+02 X 1.0 METERS

IN PHASE



QUADRATURE



d.  $\sigma_3=10.$

CURRENT DENSITY

MAXIMUM AMPLITUDE = 1.90E-07 AMP/M/M

PLATE CONDUCTIVITY = 1.00E+02 MHO/M

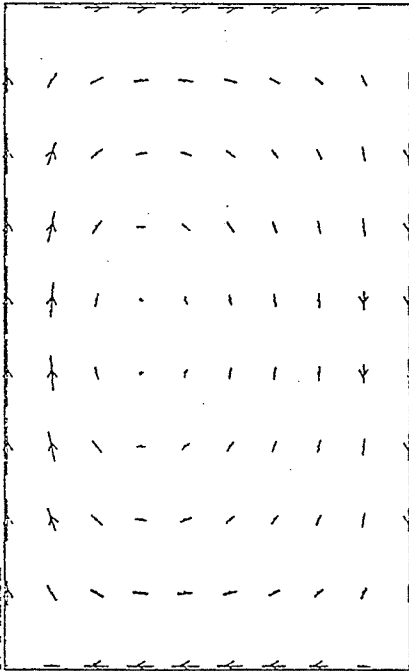
HOST CONDUCTIVITY = 1.00E-03 MHO/M

PLATE SIZE = 2.50E+02 X 1.50E+02 X 1.0 METERS

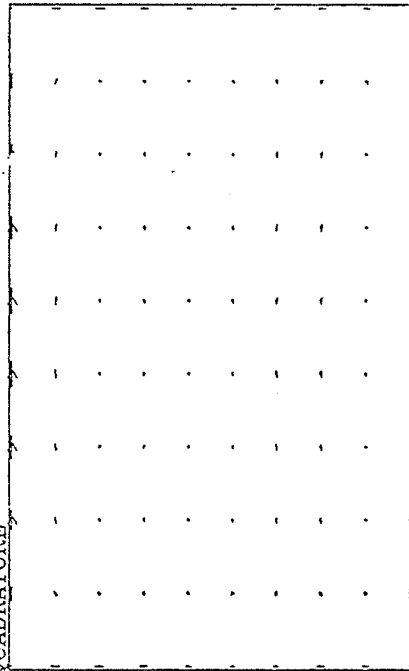
COIL HEIGHT = 0.00E+00 M

PLATE DEPTH = 50. M

IN PHASE



QUADRATURE



e.  $\sigma_3 = 100.$

CURRENT DENSITY

MAXIMUM AMPLITUDE = 2.00E-07 AMP/M/M

PLATE CONDUCTIVITY = 1.00E+03 MHO/M

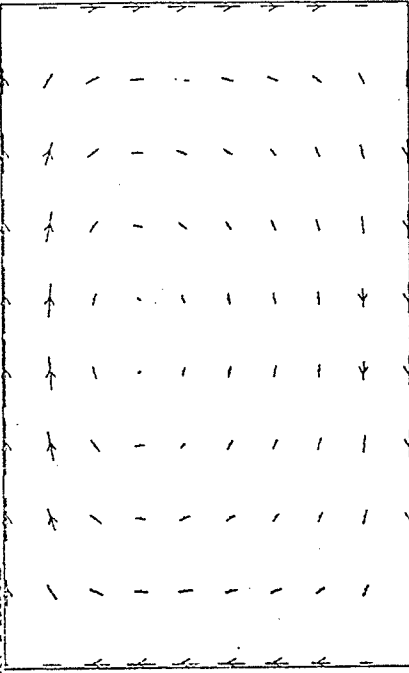
HOST CONDUCTIVITY = 1.00E-03 MHO/M

PLATE SIZE = 2.50E+02 X 1.50E+02 X 1.0 METERS

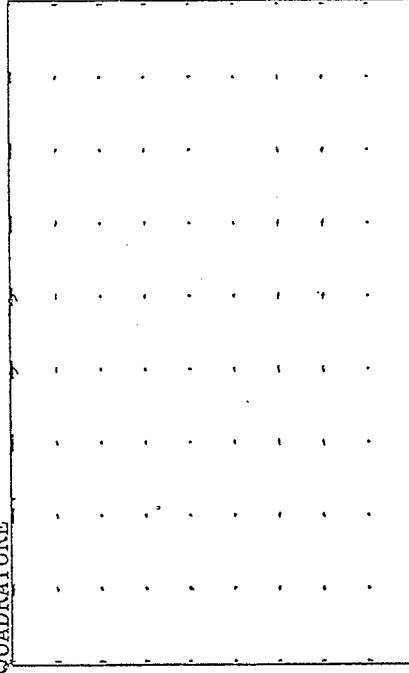
COIL HEIGHT = 0.00E+00 M

PLATE DEPTH = 50. M

IN PHASE



QUADRATURE



f.  $\sigma_3 = 1000.$

TABLE 7-6

Maximum Amplitude of the In-Phase or Quadrature  
Component of the Current Comparing Results  
with those of Lajoie (1973)

Lajoie	Hanneson	$\alpha_P$	$\alpha_P/\alpha_H$
$3.29 \times 10^{-10}$	$4.36 \times 10^{-10}$	.01	.05
$2.79 \times 10^{-9}$	$3.75 \times 10^{-9}$	.1	.5
$2.04 \times 10^{-8}$	$2.44 \times 10^{-8}$	1.	5.
$8.38 \times 10^{-8}$	$1.07 \times 10^{-7}$	10.	50.
$1.45 \times 10^{-7}$	$1.90 \times 10^{-7}$	100.	500.
$1.46 \times 10^{-7}$	$2.00 \times 10^{-7}$	1000.	5000.

## CHAPTER VIII

### CONCLUDING REMARKS

#### 8.1 Previous Attempts

While several other workers have addressed this problem using a variety of different strategies yielding a varying amount of success, this section reports only on earlier attempts by this author. These remarks give a brief chronological overview of how the project developed and are presented as a precaution to future workers.

Point collocation with localized test functions is described by Hohmann (1970, 1975) to solve the two-dimensional as well as the three-dimensional problem. The test functions are rectangular pulses arrayed over the scatterer, the heights of which are obtained through point collocation. The method yields reasonable results for low conductivity contrasts, but as the contrast increases it breaks down shortly after the development of the quadrature vortex and fails to generate an in-phase vortex. The present writer substituted triangular pulses (Harrington, 1968) for the rectangular pulses leading to a solution having linear piecewise continuous current components on the plate. When the in-phase vortex again failed

to develop at high conductivity contrasts, cubic, and then quintic spline pulses of the type described by Lajoie (1973) were employed. The solution, in spite of being continuous and having continuous first derivatives, again failed to yield the desired in-phase vortex, and the method of point collocation with localized test functions was abandoned.

The next attempt used point collocation with non-localized or global test functions of the form  $y^n z^m$  discussed briefly in Section 6.3. It was immediately apparent that the global test functions represented a significant advance when, even for a small number of match points, the in-phase vortex developed for high scatterer conductivities. Further testing revealed trouble with near-source solutions, and led to the development of the reciprocity test which yielded error estimates of several tens of percent for a vertical magnetic dipole  $S/6$  from the top edge of the plate. The distance  $S/6$  is significant because this is the nearest transmitter location necessary in modelling the horizontal loop response of a plate of strike length  $S=3L$ .

A variational least squares method using the non-localized test functions was next invoked in attempting to reduce the error as estimated with the reciprocity test. The method for setting up the matrix is described in Appendix D wherein the operator equation D1 is the formulating equation, Equation 2.6. The results were initially encouraging with greatly reduced reciprocity error estimates (less than 10 percent) at low conductivity contrasts. At higher conductivity contrasts, however,

reductions in the scatter current intensity violated the physical requirements of the solution. It was apparent that increases in the conductivity contrast were accompanied by increases in the matrix condition number (defined as the logarithm of the ratio of the largest to smallest eigenvalues in the matrix) which had a value of about 5 when the numerical failure became obvious. Attempts were made to suppress the eigencurrents associated with the smallest eigenvalues, but no advantage was gained and it was assumed that these eigencurrents contribute significantly to the solution. It seems likely that 5 represents the number of correctly computed digits in the more important elements of the matrix.

This variational method, although it failed at high conductivity contrasts, was useful in pointing out major sources of error in the method of point collocation with global test functions, and led to the inclusion of the boundary conditions discussed in Section 6.3.

## 8.2 Suggestions for Future Work

While the results discussed in Chapter VII appear to be useful when host conductivity effects are pronounced, cases where  $\alpha_P/\alpha_H$  is large still present problems. For these cases magnetic effects predominate and greater numerical effort seems necessary to affect a solution of the electric field integral equation. Of the two coupled integral equations discussed by Hohmann (1970), one reduces to Equation 2.6 when there is no permeability contrast, while the other reduces to



$$\tilde{H}(\tilde{r}) = \tilde{H}^i(\tilde{r}) + (\sigma_1 - \sigma_2) \int_V G_{\tilde{H}J}(\tilde{r}|\tilde{r}_s) \tilde{E}(\tilde{r}_s) dV_s$$

where  $G_{\tilde{H}J}$  is the Green's tensor for the magnetic field at  $\tilde{r}$  due to an electric dipole at  $\tilde{r}_s$ . Using the Ampere-Maxwell equation,  $\nabla \times \tilde{H} = (\sigma + i\epsilon\omega)\tilde{E}$ , reduces the above equation to an integral equation for the magnetic field in the scatterer which could presumably be solved using a method similar to that described in preceding chapters. Such a method has been used by Lamontagne and West (1971) and by Annan (1974) for the plate model in free space. It is easy to believe that a numerical solution of the magnetic field integral equation would fail when electrical effects predominate. Whether or not such a solution could handle sufficiently conductive hosts so as to complete the correspondence between the values of  $\alpha_H$  quoted in this work, and the non-conducting hosts considered by Lamontagne and West (1971) and Annan (1974) is uncertain but seems likely.

A second problem within reach is the numerical simulation of multiple conductors. An iterative approach to the response of two conductors, for example, might yield useful results but would be computationally expensive. The first step would be to compute the secondary current on conductor 1 ignoring conductor 2; then the secondary current on conductor 2 could be computed using as the incident field, the field from the transmitter plus the fields radiated from the scatter current in conductor 1. A second approximation to the scatter currents in conductor 1 could be computed having a first approximation for the currents in conductor 2, and so on until subsequent

approximations converge. The rate of convergence would depend on the degree of EM coupling between the two scatterers.

Aside from the obvious need to study other prospecting systems, there are other problems of considerable interest which have not yet received attention. To mention two, they are the response of a non-vertical conductor in a conductive earth, and the response of a conductor in contact with the upper layer of a two-layer earth. Problems in this section represent important generalizations to the present work and their solutions would permit the interpretation of a much broader range of field situations.

### 8.3 Summary and Conclusion

In this study of the electromagnetic response of a thin plate, it is apparent that an approximate solution to the electric field integral equation has been attained which is capable of simulating electric as well as magnetic effects. The approximation is acceptable for moderate conductivity contrasts but gradually worsens for high scatterer conductivities where magnetic effects predominate. It is certain that the computed results are unacceptable when  $\alpha_P/\alpha_H > 64$  together with  $\alpha_H < 0.5$ .

Attempts were made to simulate the response of plates which are large compared to the dimensions of the transmitter-receiver array. It is apparent that plates of size  $3L \times 1.5L$  give reasonable approximations to semi-infinite half-planes and also that the asymptotes are approached more quickly for plates in conductive hosts.

For a homogeneous half-space the effects of host conductivity on the horizontal loop response of a large vertical plate of given conductivity are four-fold. As the host conductivity increases from zero, the initial effect is a slight counter clockwise phase rotation of the anomaly due to the channelling of quadrature currents from the host into the conductor. Alternatively stated, the effect is anomaly enhancement due to the increase in scatter current density. Further increases in the host conductivity lead to clockwise phase rotations due to phase shifts in the incident field, and anomaly enhancement continues until the response is about double the response in free space. Further effects of host conductivity are anomaly attenuation and additional clockwise phase rotations. These latter effects are due to propagation losses suffered by the incident field travelling to the plate and the secondary field travelling from the plate to the receiver.

The effects of increasing frequency are qualitatively similar but increases in anomaly magnitudes are more dramatic. The choice of frequency can easily make the difference between a recognizable and an unrecognizable anomaly, but from a practical point of view, it is recognized that slight lateral inhomogeneities in the host conductivity or layer response will also have significant effects on the horizontal loop profile at high frequencies.

Conductive overburden, provided it is not in electrical contact with the conductor, can only detract from the effectiveness of EM prospecting. On horizontal loop anomalies, the

effect of conductive overburden is anomaly attenuation and clockwise phase rotation, due to losses encountered by the fields in passing through the layer.

The two case histories discussed earlier show that the numerical solution is capable of resolving some of the ambiguities in multifrequency horizontal loop prospecting, but the veracity of many of the results in Chapter VII awaits confirmation. While it has not been possible to find empirical confirmation of the results of this work in the literature, laboratory studies do show that the physical principles are being well represented. One hopes that the experimental problem of conductivity contrasts will be resolved and that an independent confirmation of the numerical solution will eventually result.

## REFERENCES

- Abramowitz, M. and I. A. Stegun, 1968. Handbook of Mathematical Functions with Formulas, Graphs and Mathematical Tables. New York: Dover Publications Inc.
- Anderson, W. L., 1979. Numerical Evaluation of Related Hankel Transforms of Orders 0 and 1 by Adaptive Digital Filtering, Geophysics, 44, No. 7, 1287-1305.
- Annan, A. P., 1974. Equivalent Source Method for Electromagnetic Scattering Analysis and its Geophysical Application, Ph.D. Thesis, Memorial University of Newfoundland.
- Betz, J. E., 1974. Test Program Report with Additional Comments on the MAXMIN II Electromagnetic System. Apex Parametrics Ltd., Toronto.
- Dyck, A.V., 1980. Operating Manual and Documentation for Interactive EM Modelling Programs PLATE and SPHERE, Research in Applied Geophysics, No.14, Department of Physics University of Toronto.
- Eadie, T., 1979. Stratified Earth Interpretation Using Standard Horizontal Loop Electromagnetic Data. Research in Applied Geophysics, No. 9, Department of Physics, University of Toronto.
- Frischknecht, F. C., 1967. Fields about an Oscillating Magnetic Dipole over a Two-layer Earth and Application to Ground and Airborne Electromagnetic Surveys. Quarterly of the Colorado School of Mines, vol.62. n.1.
- Gabillard, R., P. Degauque, and J. R. Wait, 1971. Subsurface Electromagnetic Telecommunication - A Review. IEEE Transactions on Communication Technology, COM-19, No. 6, 1217-1228.
- Gaur, V. K., O. P. Verma, and C. P. Gupta, 1971. Enhancement of Electromagnetic Anomalies by a Conducting Overburden, Geophysical Prospecting, 20, 580-604.
- Ghosh, D. P., 1971. The Application of Linear Filter Theory to the Direct Interpretation of Geoelectric Resistivity Sounding Measurements, Geophysical Prospecting, 19, 192-217.
- Grant, F. S., and G. F. West, 1965. Interpretation Theory in Applied Geophysics, McGraw-Hill, New York.
- Gupta, C. P., 1973. Models in Applied Geoelectromagnetics, Ph.D. Thesis, University of Roorkee.

- Gupta, O. P., M. S. Joshi, and J. G. Negi, 1980. Scale Model Electromagnetic Response to Inline and Broadside Systems at Skew Traverses of a Dipping Half-Plane Embedded in a Conductive Host Rock, Geophysical Prospecting, 28, 119-134.
- Gupta Sarma, D., and V. M. Maru, 1971. A Study of Some Effects of a Conducting Host Rock with a New Modelling Apparatus, Geophysics, 36, 166-183.
- Harrington, R. F., 1961. Time Harmonic Electromagnetic Fields, McGraw-Hill, New York.
- Harrington, R. F., 1968. Field Computation by Moment Methods, Macmillan and Co., New York.
- Hohmann, G. W., 1970. Electromagnetic Scattering by Two Dimensional Inhomogeneities in the Earth, Ph.D. Thesis, University of California, Berkeley.
- Hohmann, G. W., 1975. Three-Dimensional Induced Polarization and Electromagnetic Modelling, Geophysics, 40, No. 2, 309-324.
- Keller, G. V., and F. C. Frischknecht, 1970. Electrical Methods in Geophysical Prospecting, Pergamon Press, Oxford.
- Ketola, M., 1968. The Interpretation of Slingram (horizontal loop) Anomalies by Small-Scale Model Measurements, Report of Investigations No. 2, Geological Survey of Finland, Otaniemi, Finland.
- Ketola, M. and M. Puranen, 1967. Type Curves for the Interpretation of Slingram (horizontal loop) Anomalies over Tabular Bodies, Report of Investigations No. 1, Geological Survey of Finland, Otaniemi, Finland.
- Lajoie, J. J., 1973. The Electromagnetic Response of a Conductive Inhomogeneity in a Layered Earth, Ph.D. Thesis, University of Toronto.
- Lajoie, J. J., and G. F. West, 1976. The Electromagnetic Response of a Conductive Inhomogeneity in a Layered Earth, Geophysics, 41, No. 6A, 1133-1156.
- Lajoie, J. J. and G. F. West, 1977. Two Selected Field Examples of EM Anomalies in a Conductive Environment. Geophysics, 42, No. 3, 655-660.
- Lamontagne, Y. and G. F. West, 1971. EM Response of a Rectangular Thin Plate, Geophysics, 36, No. 6, 1204-1222.
- Longman, I. M., 1956. Note on a Method for Computing Infinite Integrals of Oscillatory Functions, Cambridge Philosophical Society Proceedings, V52, p 764.

- McDonald, B. H., M. Friedman, and A. Wexler, 1974. Variational Solution of Integral Equations, IEEE Transactions on Microwave Theory and Techniques, MTT-22, No. 3, 237-248.
- Moore, R. K. and W. E. Blair, 1961. Dipole Radiation in a Conducting Half-Space, Journal of Research, 65D, No. 6, 547-563.
- Nair, M. R., S. K. Biswas, and K. Mazumdar, 1968. Experimental Studies on the Electromagnetic Response of Tilted Conducting Half-Planes to a Horizontal Loop Prospecting System, Geoexploration, 6, 207-244.
- Palacky, G. J. and F. O. Sena, 1979. Conductor Identification in Tropical Terrains - Case Histories from the Itipacuru Greenstone Belt, Bahia, Brazil. Geophysics, 44, No. 12, 1941-1962.
- Siegel, M. and R. P. W. King, 1970. Electromagnetic Fields in a Dissipative Half-Space, Journal of Applied Physics, 41, No. 6, 2415-2423.
- Sinclair, G., 1948. Theory of Models of Electromagnetic Systems, Proceedings of the IRE, 36, 1364-1370.
- Strangeway, D. W., 1967. Electromagnetic Parameters for Some Sulfide Ore Bodies, Mining Geophysics, 1, Society of Exploration Geophysicists.
- Van Bladel, J., 1961. Some Remarks on Green's Dyadic for Infinite Space, IRE Transactions on Antennas and Propagation, 563-566.
- \_\_\_\_\_, 1964. Electromagnetic Fields, McGraw-Hill, New York.
- Villegas-Garcia, C. J., 1979. On the Electromagnetic Response of Non-Uniform Overburden Layers: Scale Model Experiments. Research in Applied Geophysics, Department of Physics, University of Toronto.
- Wait, J. R., 1951. Magnetic Dipole Over the Horizontally Stratified Earth, Canadian Journal of Physics, 29, 577-592.
- \_\_\_\_\_, 1953a. Radiation From a Vertical Electric Dipole Over a Stratified Ground, IRE Transactions - Antennas and Propagation, AP-1, 9-12.
- \_\_\_\_\_, 1953b. Fields of an Electric Dipole in a Semi-Infinite Conducting Medium, Journal of Geophysical Research, 58, No. 1, 21-28.

- Wait, J.R., 1959. Radiation from a Small Loop Immersed in a Semi-Infinite Conducting Medium, Canadian Journal of Physics, 37, 672-674.
- \_\_\_\_\_, 1961. The Electromagnetic Field of a Horizontal Dipole in the Presence of a Conducting Half-Space. Canadian Journal of Physics, 39, 1017-1028.
- \_\_\_\_\_, and J. A. Fuller, 1971. On Radio Propagation Through the Earth, IEEE Transactions on Antennas and Propagation, AP-19, No. 6, 796-798.
- Ward, S. H., 1967. Electromagnetic Theory for Geophysical Applications, Mining Geophysics, 2, Society of Exploration Geophysicists.
- West, G. F., 1960. Quantitative Interpretation of Electromagnetic Prospecting Measurements, Ph.D. Thesis, University of Toronto.
- West, G. F., 1979. Personal Communication.



## APPENDIX A

Electric Field at the Centre of a Spherical  
Volume of Constant Current

We wish to evaluate

$$\vec{E}(\vec{r}) = \frac{-\nabla J}{4\pi i \epsilon \omega} \int_S \psi(\vec{r}|\vec{r}_S) \hat{j} \cdot d\vec{s}_S - \frac{i\omega\mu}{4\pi} J \int_V \psi(\vec{r}|\vec{r}_S) dV_S \quad \text{Eq. A1}$$

at  $\vec{r}=0$  for a spherical region of radius  $a$  centred at  $\vec{r}=0$ .

The first term is the contribution from the scalar potential. With reference to Figure A-1, the contribution from the upper hemisphere only is

$$E_{+\frac{1}{2}}^{SC}(\vec{r}) = \frac{-\nabla J}{4\pi i \epsilon \omega} \int_S \frac{e^{-\gamma|\vec{r}-\vec{r}_S|}}{|\vec{r}-\vec{r}_S|} \hat{j} \cdot \hat{u}_S dS_S$$

By a theorem from vector analysis,

$$\int_S \vec{F} \cdot \hat{u} dS = \int_Q \frac{\vec{F} \cdot \hat{u}}{|\hat{u} \cdot \hat{j}|} dx dz$$

where  $\vec{F}$  is a vector field defined on the surface  $s$ ,  $\hat{u}$  is the unit outward normal, and  $Q$  is the projection of  $s$  on the  $x-z$  plane. Thus in cylindrical coordinates,

$$E_{+\frac{1}{2}}^{SC}(\vec{r}) = \frac{-\nabla J}{4\pi i \epsilon \omega} \int_{\theta=0}^{2\pi} \int_{\rho_S=0}^a \frac{e^{-\gamma|\vec{r}-\vec{r}_S|}}{|\vec{r}-\vec{r}_S|} \rho_S d\rho_S d\theta_S$$

where  $|\vec{r}-\vec{r}_S| = [(\rho-\rho_S)^2 + (y-y_S)^2]^{\frac{1}{2}}$

The surface is  $y_S = (a^2 - \rho_S^2)^{\frac{1}{2}}$ , therefore

$$E_{+\frac{1}{2}}^{SC}(\vec{r}) = \frac{-J\nabla}{2i\epsilon\omega} \int_{\rho_S=0}^a \frac{e^{-\gamma\{(\rho-\rho_S)^2 + [y-(a^2-\rho_S^2)^{\frac{1}{2}}]^2\}^{\frac{1}{2}}}}{\{(\rho-\rho_S)^2 + [y-(a^2-\rho_S^2)^{\frac{1}{2}}]^2\}^{\frac{1}{2}}} \rho_S d\rho_S$$

Taking the  $\nabla$  operator inside the integral, performing the differentiations, and evaluating the results at  $\rho=y=0$  yields

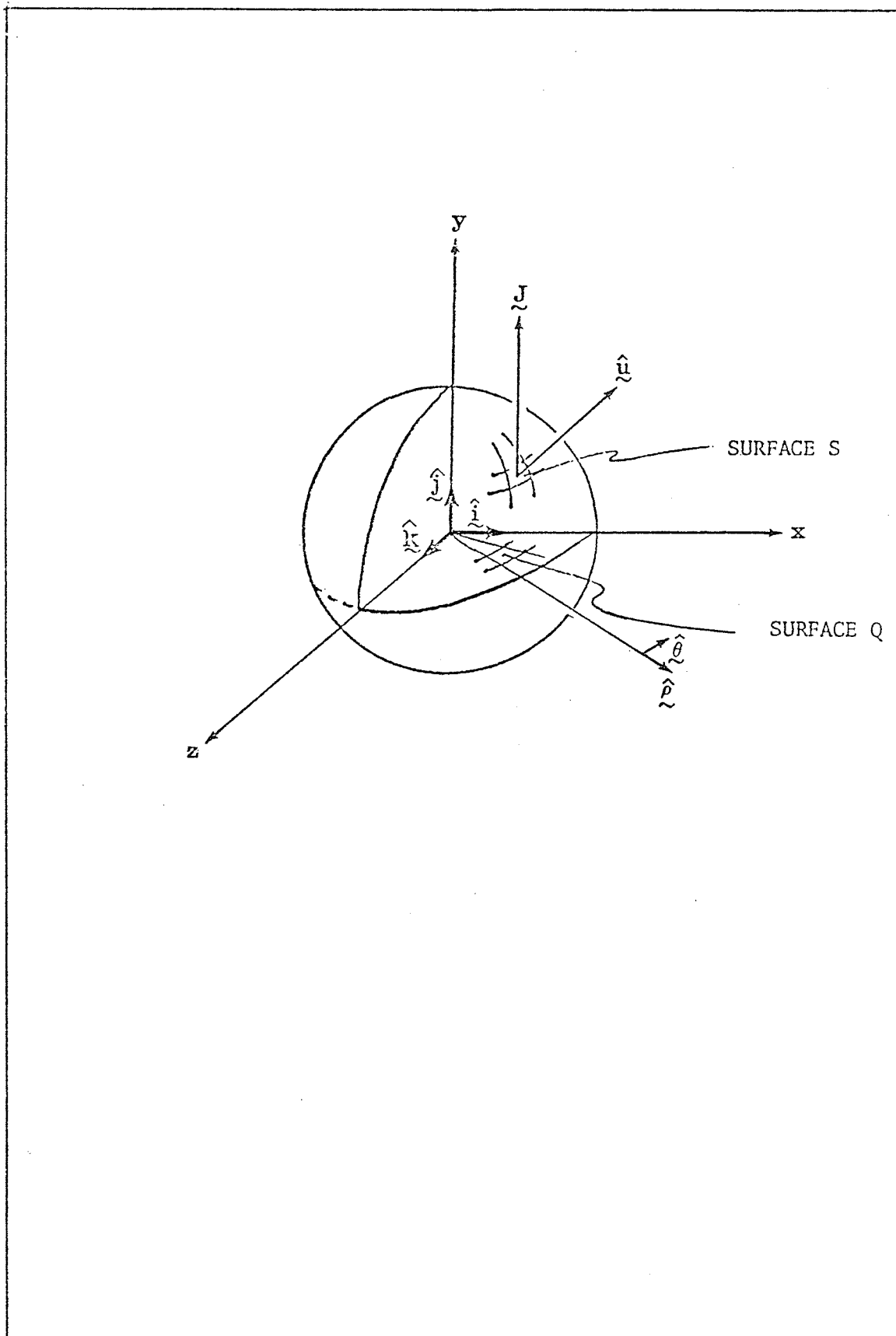


Figure A-1

$$\begin{aligned} \tilde{E}_{+\frac{1}{2}}^{SC}(\underline{o}) &= \frac{-J}{2i\epsilon\omega} \int_{\rho_s=0}^a \left\{ \left[ \frac{\gamma \rho_s e^{-\gamma a}}{a^2} + \frac{\rho_s e^{-\gamma a}}{a^3} \right] \hat{\rho}_s \right. \\ &\quad \left. + \left[ \frac{\gamma (a^2 - \rho_s^2)^{\frac{1}{2}} e^{-\gamma a}}{a^2} + \frac{(a^2 - \rho_s^2)^{\frac{1}{2}} e^{-\gamma a}}{a^3} \right] \hat{j} \right\} \rho_s d\rho_s \quad \text{Eq.A2} \end{aligned}$$

where  $\hat{\rho}_s$  is the unit radius vector in the x-z plane. For the lower half of the hemispherical surface,  $\gamma_s = -(a^2 - \rho_s^2)^{\frac{1}{2}}$ ,  $\hat{j} \cdot \hat{u}$  has the opposite sign and a similar development of Equation A2 would give

$$\begin{aligned} \tilde{E}_{-\frac{1}{2}}^{SC}(\underline{o}) &= \frac{+J}{2i\epsilon\omega} \int_{\rho_s=0}^a \left\{ \left[ \frac{\gamma \rho_s e^{-\gamma a}}{a^2} + \frac{\rho_s e^{-\gamma a}}{a^3} \right] \hat{\rho}_s \right. \\ &\quad \left. - \left[ \frac{\gamma (a^2 - \rho_s^2)^{\frac{1}{2}} e^{-\gamma a}}{a^2} + \frac{(a^2 - \rho_s^2)^{\frac{1}{2}} e^{-\gamma a}}{a^3} \right] \hat{j} \right\} \rho_s d\rho_s \quad \text{Eq.A3} \end{aligned}$$

Summing Equations A2 and A3 the full contribution from the scalar potential is

$$\tilde{E}^{SC}(\underline{o}) = \frac{-J \hat{j}}{i\epsilon\omega} \int_{\rho_s=0}^a \left[ \frac{\gamma (a^2 - \rho_s^2)^{\frac{1}{2}} e^{-\gamma a}}{a^2} + \frac{(a^2 - \rho_s^2)^{\frac{1}{2}} e^{-\gamma a}}{a^3} \right] \rho_s d\rho_s$$

A few simple steps yields

$$\tilde{E}^{SC}(\underline{o}) = -\frac{1}{3} \frac{J}{i\epsilon\omega} e^{-\gamma a} (\gamma a + 1) \hat{j} \quad \text{Eq.4A}$$

The contribution from the vector potential is the second term in Equation A1 and is easily reduced in spherical coordinates. For this term we write

$$\begin{aligned} \tilde{E}^{vec}(\underline{o}) &= \frac{-i\omega\mu}{4\pi} J \hat{j} \int_{\phi=0}^{2\pi} \int_{\theta=0}^{\pi} \int_{r_s=0}^a \frac{e^{-\gamma r_s}}{r_s} r_s^2 dr_s \sin\theta_s d\theta_s d\phi_s \\ &= \frac{-J}{i\epsilon\omega} \hat{j} \left[ \frac{2}{3} e^{-\gamma a} (\gamma a + 1) - 1 \right] \quad \text{Eq.A5} \end{aligned}$$

Summing Equations A4 and A5 gives for the total field at the

centre of the sphere

$$\tilde{E}(\tilde{0}) = \frac{J}{i\varepsilon\omega} \hat{j} \left[ \frac{2}{3} e^{-\gamma a} (\gamma a + 1) - 1 \right].$$

## APPENDIX B

Hertz Potential for a Horizontal Electric Dipole  
in a Two-Layer Earth

The dipole is oriented along the x-axis and is located in the lower layer of a two-layer earth. The origin is at the dipole, and the locations and orientations of the conductivity interfaces are as indicated in Figure 4-1, which also designates the conductivities of the three regions.

It is assumed the electric and magnetic fields can be derived from a two-component Hertz vector (which is expressed as

$$\vec{\pi} = \pi_x \hat{i} + \pi_z \hat{k}$$

through

$$\vec{E} = \nabla \nabla \cdot \vec{\pi} - \gamma^2 \vec{\pi} \quad \text{Eq. B.1}$$

and

$$\vec{H} = (\sigma + i\epsilon\omega) \nabla \times \vec{\pi} \quad \text{Eq. B2}$$

respectively. It can be shown (Ward, 1967, p. 19) that the components of the vector potential each satisfy the wave equation so that in cylindrical coordinates

$$\frac{1}{\rho} \frac{\partial}{\partial \rho} \left( \rho \frac{\partial \pi}{\partial \rho} \right) + \frac{1}{\rho^2} \frac{\partial^2 \pi}{\partial \theta^2} + \frac{\partial^2 \pi}{\partial z^2} - \gamma^2 \pi = 0$$

The general solution for this equation can be written (Ward, 1967, p. 61)

$$\pi(\rho, \theta, z) = \sum_{n=-\infty}^{\infty} e^{in\theta} \int_0^{\infty} \psi_n(\lambda) e^{\pm uz} J_n(\lambda\rho) d\lambda \quad \text{Eq. B3}$$

where  $u^2 = \lambda^2 + \gamma^2$

and the  $J_n(\lambda\rho)$  are Bessel functions of the first kind. The  $\psi_n(\lambda)$  are functions which are being sought to particularize

Equation B3 for the boundaries under scrutiny and are not to be confused with the  $\psi$  of Chapter III. The remainder of this section is devoted to the particularization of Equation B3.

If the angular variable  $\theta$  is measured from the dipole direction (+ x-axis) then symmetry rather than antisymmetry is required and we can choose the cosine part of de Moivre's expansion of  $e^{in\theta}$  and now write

$$\pi(\rho, \theta, z) = \sum_{n=-\infty}^{\infty} \cos n\theta \int_0^{\infty} \psi_n(\lambda) e^{\pm uz} J_n(\lambda\rho) d\lambda \quad \text{Eq. B4}$$

It can be inferred from Equation 3.11 that in an infinite medium ( $\sigma_0 = \sigma_1 = \sigma_2$ ), the Hertz potential must be simply

$$\pi^P = \frac{e^{-\gamma R}}{4\pi(\sigma + i\epsilon\omega)R}$$

where  $R = (\rho^2 + z^2)^{\frac{1}{2}}$ . Here  $\pi^P$  implies the primary potential to which other terms must be added to account for boundary effects. Also  $\epsilon(1 + \sigma/i\epsilon\omega)$  has been substituted for  $\epsilon$  in accordance with the requirements of Section 3.3. Ward also shows that

$$\frac{e^{-\gamma R}}{R} = \int_0^{\infty} \frac{\lambda}{\mu} e^{\pm uz} J_0(\lambda\rho) d\lambda \quad \text{Eq. B5}$$

a relation which is referred to by other workers (such as Wait and Fuller, 1971) as the Sommerfeld integral and will be of use shortly.

Equation B5 can be expanded to

$$\pi(\rho, \theta, z) = \sum_{n=-\infty}^{\infty} \cos n\theta \int_0^{\infty} [\psi_{up}(\lambda) e^{uz} + \psi_{dn}(\lambda) e^{-uz}] J_n(\lambda\rho) d\lambda \quad \text{Eq. B6}$$

and when a factor of  $e^{+i\omega t}$  is remembered to occur implicitly, the first term of the integrand is seen to represent an upward-travelling wave and the second to represent an downward travel-

ling wave. In general one constructs solutions by choosing signs for the exponentials in accordance with what is physically possible for each of the four regions. For instance, in the upper layer (air), there can be no downward-travelling wave and the solution must be of the form

$$\pi_{x_0} = \sum_{n=-\infty}^{\infty} \cos n\theta \int_0^{\infty} \psi_1(\lambda) e^{u_0 z} J_n(\lambda \rho) d\lambda \quad \text{Eq. B7}$$

where the exponential involves  $u_0 = (\lambda^2 + \gamma_0^2)^{\frac{1}{2}}$ , where  $\gamma_0$  is the propagation constant for air. Since the upper earth layer can have waves travelling upward from the source as well as downward-travelling waves partially reflected at the air-earth interface, we write for region 1 (upper earth layer)

$$\pi_{x_1} = \sum_{n=-\infty}^{\infty} \cos n\theta \int_0^{\infty} [\psi_2(\lambda) e^{u_1 z} + \psi_3(\lambda) e^{-u_1 z}] J_n(\lambda \rho) d\lambda \quad \text{Eq. B8}$$

where  $u_1 = (\lambda^2 + \gamma_1^2)^{\frac{1}{2}}$ . In the lower medium above the dipole (region two), there can be upward and downward travelling waves so that

$$\pi_{x_2} = \sum_{n=-\infty}^{\infty} \cos n\theta \int_0^{\infty} [\psi_4(\lambda) e^{u_2 z} + \psi_5(\lambda) e^{-u_2 z}] J_n(\lambda \rho) d\lambda \quad \text{Eq. B9}$$

but in the lower medium beneath the dipole (region three) there are only downward-travelling waves and the choice becomes

$$\pi_{x_3} = \sum_{n=-\infty}^{\infty} \cos n\theta \int_0^{\infty} [\psi_4(\lambda) e^{-u_2 z} + \psi_5(\lambda) e^{-u_2 z}] J_n(\lambda \rho) d\lambda.$$

The eigenfunctions  $\psi_4$  and  $\psi_5$  are chosen again since Equations B9 and the above expression for  $\pi_{x_3}$  must be identical at  $z=0$ .

It is now possible to identify the term involving  $\psi_4$  with the primary part of the Hertz vector potential and postulate that this term alone remains if the boundaries vanish. Thus in infinite space beneath the dipole the general solution

reduces further to

$$\pi_{x_3} = \sum_{n=-\infty}^{\infty} \cos n\theta \int_0^{\infty} \psi_4(\lambda) e^{-u_2 z} J_n(\lambda\rho) \lambda \quad \text{Eq. B10}$$

with a similar solution but with a positive exponent in region two. In view of the Sommerfeld integral, Equation B5, it can now be concluded that in regions two and three

$$\psi_4(\lambda) = c\lambda/u_2 \quad \text{Eq. B11}$$

and also that  $n=0$ . Since the expression for the primary potential contains only zeroth order Bessel functions, it is expected that the secondary potentials must also contain only zeroth order Bessel functions since the tangential components of the derived fields ( $\underline{E}$  and  $\underline{H}$ ) must be continuous at the boundaries. Equations B7 to B10 therefore simplify to

$$\pi_{x_0} = \int_0^{\infty} \psi_1(\lambda) e^{u_0 z} J_0(\lambda\rho) d\lambda \quad \text{Eq. B12}$$

$$\pi_{x_1} = \int_0^{\infty} [\psi_2(\lambda) e^{u_1 z} + \psi_3(\lambda) e^{-u_1 z}] J_0(\lambda\rho) d\lambda \quad \text{Eq. B13}$$

$$\pi_{x_2} = \int_0^{\infty} [\psi_4(\lambda) e^{u_2 z} + \psi_5(\lambda) e^{-u_2 z}] J_0(\lambda\rho) d\lambda \quad \text{Eq. B14}$$

$$\pi_{x_3} = \int_0^{\infty} [\psi_4(\lambda) e^{-u_2 z} + \psi_5(\lambda) e^{-u_2 z}] J_0(\lambda\rho) d\lambda \quad \text{Eq. B15}$$

To establish explicit expressions for the  $\psi_i(\lambda)$  ( $i=1,2,3,5$ ) it is necessary to impose boundary conditions which state that the tangential components of  $\underline{E}$  and  $\underline{H}$  are continuous. In terms of the Hertz potentials, the horizontal components of  $\underline{E}$  and  $\underline{H}$  are obtained through Equations B1 and B2, and for region  $n$  are:

$$\begin{aligned} E_x &= \frac{\partial}{\partial x} \left( \frac{\partial \pi_{xn}}{\partial x} + \frac{\partial \pi_{zn}}{\partial z} \right) - \gamma^2 \pi_{xn}, \quad H_x = \kappa_n \frac{\partial \pi_{zn}}{\partial y}, \\ E_y &= \frac{\partial}{\partial y} \left( \frac{\partial \pi_{xn}}{\partial x} + \frac{\partial \pi_{zn}}{\partial z} \right) \quad \text{and} \quad H_y = -\kappa_n \left( \frac{\partial \pi_{zn}}{\partial x} - \frac{\partial \pi_{xn}}{\partial z} \right) \end{aligned} \quad \text{Eqs. B16}$$



More explicitly, continuity of  $E_x$  requires at  $z=-h$

$$\frac{\partial}{\partial x} \left( \frac{\partial \pi x_2}{\partial x} + \frac{\partial \pi z_2}{\partial z} \right) - \gamma_2^2 \pi x_2 = \frac{\partial}{\partial x} \left( \frac{\partial \pi x_1}{\partial x} + \frac{\partial \pi z_1}{\partial z} \right) - \gamma_1^2 \pi x_1 \quad \text{Eq. B17}$$

while at  $z=-(h+d)$

$$\frac{\partial}{\partial x} \left( \frac{\partial \pi x_1}{\partial x} + \frac{\partial \pi z_1}{\partial z} \right) - \gamma_1^2 \pi x_1 = \frac{\partial}{\partial x} \left( \frac{\partial \pi x_0}{\partial x} + \frac{\partial \pi z_0}{\partial z} \right) - \gamma_0^2 \pi x_0 \quad \text{Eq. B18}$$

Continuity of  $E_y$  at  $z=-h$  requires

$$\frac{\partial}{\partial y} \left( \frac{\partial \pi x_2}{\partial x} + \frac{\partial \pi z_2}{\partial z} \right) = \frac{\partial}{\partial y} \left( \frac{\partial \pi x_1}{\partial x} + \frac{\partial \pi z_1}{\partial z} \right) \quad \text{Eq. B19}$$

and at  $z=-(h+d)$

$$\frac{\partial}{\partial y} \left( \frac{\partial \pi x_1}{\partial x} + \frac{\partial \pi z_1}{\partial z} \right) = \frac{\partial}{\partial y} \left( \frac{\partial \pi x_0}{\partial x} + \frac{\partial \pi z_0}{\partial z} \right) \quad \text{Eq. B20}$$

Continuity of  $H_x$  at  $z=-h$  gives

$$\kappa_2 \frac{\partial \pi z_2}{\partial y} = \kappa_1 \frac{\partial \pi z_1}{\partial y} \quad \text{Eq. B21}$$

and at  $z=-(h+d)$

$$\kappa_1 \frac{\partial \pi z_1}{\partial y} = \kappa_0 \frac{\partial \pi z_0}{\partial y} \quad \text{Eq. B22}$$

while continuity of  $H_y$  gives at  $z=-h$

$$\kappa_2 \left( \frac{\partial \pi x_2}{\partial z} - \frac{\partial \pi z_2}{\partial x} \right) = \kappa_1 \left( \frac{\partial \pi x_1}{\partial z} - \frac{\partial \pi z_1}{\partial x} \right) \quad \text{Eq. B23}$$

and at  $z=-(h+d)$

$$\kappa_1 \left( \frac{\partial \pi x_1}{\partial z} - \frac{\partial \pi z_1}{\partial x} \right) = \kappa_0 \left( \frac{\partial \pi x_0}{\partial z} - \frac{\partial \pi z_0}{\partial x} \right) \quad \text{Eq. B24}$$

It is convenient at this time to integrate Equations B19 and B20 over the  $y$ -variable and set the integration constant to zero (since the potentials and their derivatives must vanish at infinity) to obtain at  $z=-h$

$$\frac{\partial \pi x_2}{\partial x} + \frac{\partial \pi z_2}{\partial z} = \frac{\partial \pi x_1}{\partial x} + \frac{\partial \pi z_1}{\partial z} \quad \text{Eq. B25}$$

and at  $z=-(h+d)$

$$\frac{\partial \pi x_1}{\partial x} + \frac{\partial \pi z_1}{\partial z} = \frac{\partial \pi x_0}{\partial x} + \frac{\partial \pi z_0}{\partial z} \quad \text{Eq. B26}$$

Substituting Equation B25 into Equation B17 and Equation B26 into Equation B18 yields (at  $z=-h$ )

$$\gamma_2^2 \pi_{x_2} = \gamma_1^2 \pi_{x_1} \quad \text{Eq. B27}$$

and ( $z=-(h+d)$ )

$$\gamma_1^2 \pi_{x_1} = \gamma_0^2 \pi_{x_0} \quad \text{Eq. B28}$$

respectively. Integrating Equations B21 and B22 with respect to  $y$  and setting the integration constants to zero gives

$$(z=-h) \quad \kappa_2 \pi_{z_2} = \kappa_1 \pi_{z_1} \quad \text{Eq. B29}$$

$$(z=-(h+d)) \quad \kappa_1 \pi_{z_1} = \kappa_0 \pi_{z_0} \quad \text{Eq. B30}$$

Differentiating Equation B29 with respect to  $x$  allows Equation B 23 to be rewritten for  $z=-h$  as

$$\kappa_2 \frac{\partial \pi_{x_2}}{\partial z} = \kappa_1 \frac{\partial \pi_{x_1}}{\partial z} \quad \text{Eq. B31}$$

while similar treatment of Equation B30 allows Equation B24 to be written as

$$\kappa_1 \frac{\partial \pi_{x_1}}{\partial z} = \kappa_0 \frac{\partial \pi_{x_0}}{\partial z} \quad \text{Eq. B32}$$

when  $z=-(h+d)$ .

When Equations B12 to B15 are used as needed in Equations B27, B28, B30 and B31, a system of four equations results which can be solved simultaneously using Cramer's Rule for the four remaining eigenfunctions  $\psi_1$ ,  $\psi_2$ ,  $\psi_3$  and  $\psi_5$ . The system of equations in matrix form can be shown to be

$$\begin{bmatrix} 0 & \gamma_1^2 e^{-u_1 h} & \gamma_1^2 e^{u_1 h} & -\gamma_2^2 e^{u_2 h} \\ \gamma_0^2 e^{-u_0 (h+d)} & -\gamma_1^2 e^{-u_1 (h+d)} & -\gamma_1^2 e^{+u_1 (h+d)} & 0 \\ 0 & -\kappa_1 u_1 e^{-u_1 h} & \kappa_1 u_1 e^{u_1 h} & -\kappa_2 u_2 e^{u_2 h} \\ -\kappa_0 u_0 e^{-u_0 (h+d)} & \kappa_1 u_1 e^{-u_1 (h+d)} & -\kappa_1 u_1 e^{u_1 (h+d)} & 0 \end{bmatrix} \begin{bmatrix} \psi_1(\lambda) \\ \psi_2(\lambda) \\ \psi_3(\lambda) \\ \psi_5(\lambda) \end{bmatrix} = \begin{bmatrix} \frac{\gamma_2 \lambda}{u_2} e^{-u_2 h} \\ 0 \\ -\kappa_2 e^{-u_2 h} \\ 0 \end{bmatrix}$$

$$\text{Eq. B33}$$

The solution gives the expressions for  $\psi_1(\lambda)$ ,  $\psi_2(\lambda)$ ,  $\psi_3(\lambda)$  and  $\psi_5(\lambda)$  which are quoted in Section 4.2 and the y-component of the vector potential is therefore completely specified.

To obtain expressions for the z-component of the potential, it is convenient to start by considering the (symmetric) general solution to the wave equation, Equation B4, along with the boundary conditions for the tangential electric field as expressed by Equations B25 and B26. Since  $\pi_{xn}$  ( $n=0,1,2$ ) involves only zeroth order Bessel functions, and since

$$\frac{\partial}{\partial x} J_0(\lambda\rho) = \frac{-\lambda x}{\rho} J_1(\lambda\rho)$$

then the terms  $\partial\pi_{xn}/\partial x$  ( $n=0,1,2$ ) will involve only first order Bessel functions. Thus the  $\pi_{zn}$  terms must contain only first order Bessel functions because the argument of the Bessel functions ( $\lambda\rho$ ) is independent of  $z$ , and the factor  $J_n(\lambda\rho)$  is unaffected by the  $\partial/\partial z$  operation. We therefore choose  $n=1$  as the only allowable term in Equation B4 and arrive at

$$\pi_z(\rho, \theta, z) = \cos\theta \int_0^{\infty} \phi(\lambda) e^{\pm uz} J_1(\lambda\rho) d\lambda \quad \text{Eq. B34}$$

This expression can now be tailored for each of the four mathematical regions by considering upward and downward travelling waves as the physics allows. Thus in air

$$\pi_{z_0} = \cos\theta \int_0^{\infty} \phi_1(\lambda) e^{u_0 z} J_1(\lambda\rho) d\lambda \quad \text{Eq. B35}$$

in the upper layer earth

$$\pi_{z_1} = \cos\theta \int_0^{\infty} [\phi_2(\lambda) e^{u_1 z} + \phi_3(\lambda) e^{-u_1 z}] J_1(\lambda\rho) d\lambda \quad \text{Eq. B36}$$

in the lower layer above the dipole

$$\pi_{z_2} = \cos\theta \int_0^{\infty} [\phi_4(\lambda) e^{u_2 z} + \phi_5(\lambda) e^{-u_2 z}] J_1(\lambda\rho) d\lambda \quad \text{Eq. B37}$$

and beneath the dipole

$$\pi_{z_2} = \cos\theta \int_0^{\infty} [\phi_4(\lambda) e^{-u_2 z} + \phi_5(\lambda) e^{-u_2 z}] J_1(\lambda \rho) d\lambda \quad \text{Eq. B38}$$

The term involving  $\phi_4(\lambda)$  can be identified with a primary term because in both regions (above and below the dipole) it appears to travel away from the source. However, this term must vanish for an x-oriented dipole in an infinite medium. If the z-component of the potential is to vanish everywhere when  $\sigma_0 = \sigma_1 = \sigma_2$ , even at  $z=0$ , then we must have  $\phi_4(\lambda) = 0$ .

Noting that  $\cos\theta = x/\rho$  and that

$$\frac{\partial}{\partial x} \int_0^{\infty} J_0(\lambda \rho) d\lambda = -\cos\theta \int_0^{\infty} \lambda J_1(\lambda \rho) d\rho,$$

it is a straightforward exercise to substitute Equations B35 to B38 and Equations B12 to B15 into Equations B25, B26, B29 and B30 to obtain a four-by-four system of equations for the remaining unknown eigenfunctions. In matrix form the system is

$$\begin{bmatrix} 0 & -u_1 e^{-u_1 h} & u_1 e^{u_1 h} & -u_2 e^{u_2 h} \\ -u_0 e^{-u_0 (h+d)} & u_1 e^{-u_1 (h+d)} & -u_1 e^{u_1 (h+d)} & 0 \\ 0 & -\kappa_1 e^{-u_1 h} & -\kappa_1 e^{u_1 h} & \kappa_2 e^{u_2 h} \\ -\kappa_0 e^{-u_0 (h+d)} & \kappa_1 e^{-u_1 (h+d)} & \kappa_1 e^{u_1 (h+d)} & 0 \end{bmatrix} \begin{bmatrix} \phi_1(\lambda) \\ \phi_2(\lambda) \\ \phi_3(\lambda) \\ \phi_5(\lambda) \end{bmatrix} = \begin{bmatrix} A_1 \\ A_2 \\ 0 \\ 0 \end{bmatrix}$$

where

$$A_1 = \lambda c [-\psi_2(\lambda) e^{-u_1 h} - \psi_3(\lambda) e^{u_1 h} + \psi_4(\lambda) e^{-u_2 h} + \psi_5(\lambda) e^{u_2 h}]$$

$$A_2 = \lambda c [-\psi_1(\lambda) e^{-u_0 (h+d)} + \psi_2(\lambda) e^{-u_1 (h+d)} + \psi_3(\lambda) e^{-u_1 (h+d)}]$$

The solution for this set of equations is given by the expressions for the  $\phi$  functions found in Section 4.2.

## APPENDIX C

Hertz Potential for a Vertical Electric Dipole  
in a Two-Layer Earth

The media, the coordinate system, and the locations of the source and interfaces are described by Figure 4-2. For a vertical dipole, the fields can be derived from a Hertz vector potential having only a z-component through

$$\vec{E} = -\gamma_n^2 \vec{\pi}_z + \nabla \nabla \cdot \vec{\pi}_z \quad \text{Eq. C1}$$

and

$$\vec{H} = \kappa_n \nabla \times \vec{\pi}_z \quad \text{Eq. C2}$$

where  $\kappa_n = (\sigma_n + i\epsilon\omega)$  and  $n$  ( $n=0,1,2$ ) specifies the physical region.

The Hertz potential must satisfy the wave equation, the general solution of which is given by Equation B5. Symmetry requires that there be no variation with respect to  $\theta$  indicating that the zeroth term of the sum is the only allowable solution. A sufficiently general solution for the  $n^{\text{th}}$  region can therefore be written as

$$\pi_n = \int_0^\infty [\psi_{\text{up}}(\lambda) e^{u_n z} + \psi_{\text{du}}(\lambda) e^{-u_n h}] J_0(\lambda \rho) d\lambda \quad \text{Eq. C3}$$

where we expanded the exponential terms to indicate separate solutions for upward and downward travelling waves. The different physical regions require different eigenfunctions so that in air we will use

$$\pi_{z_0} = \int_0^\infty [\psi_1(\lambda) e^{u_0 z} + \psi_2(\lambda) e^{-u_0 z}] J_0(\lambda \rho) d\lambda \quad \text{Eq. C4}$$

in the upper earth layer

$$\pi_{z_1} = \int_0^\infty [\psi_3(\lambda) e^{u_1 z} + \psi_4(\lambda) e^{-u_1 z}] J_0(\lambda \rho) d\lambda. \quad \text{Eq. C5}$$

In the lower layer above the dipole

$$\pi_{z_2} = \int_0^{\infty} [\psi_5(\lambda) e^{u_2 z} + \psi_6(\lambda) e^{-u_2 z}] J_0(\lambda \rho) d\lambda \quad \text{Eq. C6}$$

while beneath the dipole

$$\pi_{z_2} = \int_0^{\infty} [\psi_5(\lambda) e^{-u_2 z} + \psi_6(\lambda) e^{u_2 z}] J_0(\lambda \rho) d\lambda \quad \text{Eq. C7}$$

Since there can be no downward travelling wave in the air we immediately set  $\psi_2(\lambda) = 0$ . Furthermore, for reasons described in Appendix B,  $\psi_5(\lambda)$  can be identified with the primary part of the vector potential and the integral transformation must lead to  $c_2 e^{-\gamma R}/R$  where  $c_2 = 1/4\pi\kappa_2$ . Thus the Sommerfeld integral, Equation 4.2 requires that

$$\psi_5(\lambda) = c\lambda/u_2. \quad \text{Eq. C8}$$

The remaining four eigenfunctions are obtained by matching the tangential components of  $\underline{E}$  and  $\underline{H}$  at the boundaries. Equations C1 and C2 can be used to show that in medium n:

$$E_x = \frac{\partial}{\partial x} \frac{\partial \pi z n}{\partial z} \quad \text{Eq. C9}$$

$$E_y = \frac{\partial}{\partial y} \frac{\partial \pi z n}{\partial z} \quad \text{Eq. C10}$$

$$H_x = \kappa_n \frac{\partial \pi z n}{\partial y} \quad \text{Eq. C11}$$

$$H_y = -\kappa_n \frac{\partial \pi z n}{\partial x}. \quad \text{Eq. C12}$$

At the air-earth interface,  $z = -(h+d)$ , we can write Equations C9 and C11 as

$$\frac{\partial \pi z_0}{\partial z} = \frac{\partial \pi z_1}{\partial z} \quad \text{Eq. C13}$$

and

$$\kappa_0 \frac{\partial \pi z_0}{\partial y} = \kappa_1 \frac{\partial \pi z_1}{\partial y} \quad \text{Eq. C14}$$

while at  $z=-h$  they become

$$\frac{\partial \pi z_1}{\partial z} = \frac{\partial \pi z_2}{\partial z} \quad \text{Eq. C15}$$

and

$$\kappa_1 \frac{\partial \pi z_1}{\partial y} = - \kappa_2 \frac{\partial \pi z_2}{\partial y} \quad \text{Eq. C16}$$

where both sides of each equation have been integrated with respect to  $x$  or  $y$ . The integration constants have been set to zero since the potentials must vanish at infinity. When Equations C4 to C7 are substituted in Equations C13 to C16, a system of four equations results which can be solved simultaneously for the remaining eigenfunctions. This set of equations is given in matrix form as

$$\begin{bmatrix} 0 & \kappa_1 e^{-u_1 h} & \kappa_1 e^{u_1 h} & \kappa_2 e^{u_2 h} \\ \kappa_0 e^{-u_0 (h+d)} & -\kappa_1 e^{-u_1 (h+d)} & -\kappa_1 e^{u_1 (h+d)} & 0 \\ 0 & u_1 e^{-u_1 h} & -u_1 e^{u_1 h} & u_2 e^{u_2 h} \\ u_0 e^{-u_0 (h+d)} & -u_1 e^{-u_1 (h+d)} & u_1 e^{u_1 (h+d)} & 0 \end{bmatrix} \begin{bmatrix} \psi_1(\lambda) \\ \psi_3(\lambda) \\ \psi_4(\lambda) \\ \psi_6(\lambda) \end{bmatrix} = \begin{bmatrix} \frac{c\kappa_2 \lambda}{u_2} e^{-u_2 h} \\ 0 \\ c\lambda e^{-u_2 h} \\ 0 \end{bmatrix} \quad \text{Eq. C17}$$

This system can be solved using Cramer's rule to yield the expressions for  $\psi_1(\lambda)$ ,  $\psi_2(\lambda)$ ,  $\psi_4(\lambda)$  and  $\psi_6(\lambda)$  as quoted in Section 4.3.

## APPENDIX D

Least Squares Matrix for a Vector  
Operator Equation

Solve the vector operator equation

$$L \underline{u}(\underline{r}) = \underline{S}(\underline{r}) \quad \text{Eq.D1}$$

where  $\underline{u}(\underline{r})$  is the true solution and is a two-dimensional vector field, and  $\underline{S}(\underline{r})$  is the source field and is also two-dimensional. Suppose each component of the true solution can be approximated by a linear combination of test functions in the manner

$$\underline{U}(\underline{r}) = \sum_{j=1}^{M/2} a_j \phi_j(\underline{r}) \hat{j} + \sum_{j=\frac{M}{2}+1}^M a_j \phi_j(\underline{r}) \hat{k} \quad \text{Eq.D2}$$

where the  $a_j$  are scalar coefficients, and the  $\phi_j(\underline{r})$  are the test functions. Substituting Equation D2 into Equation D1 gives, since  $L$  is assumed linear,

$$\sum_{j=1}^{M/2} a_j L \phi_j(\underline{r}) \hat{j} + \sum_{j=\frac{M}{2}+1}^M a_j \phi_j(\underline{r}) \hat{k} \simeq \underline{S}(\underline{r})$$

At any point  $\underline{r}$ , define the difference between the true solution and the approximate solution as

$$\underline{e}(\underline{r}) = \sum_{j=1}^{M/2} a_j L \phi_j(\underline{r}) \hat{j} + \sum_{j=\frac{M}{2}+1}^M a_j \phi_j(\underline{r}) \hat{k} - S_y(\underline{r}) \hat{j} - S_z(\underline{r}) \hat{k}$$

where  $S_y(\underline{r})$  and  $S_z(\underline{r})$  are the y and z components of  $\underline{S}(\underline{r})$ . Define the mean-square error  $\epsilon(\underline{r}; a_1, a_2, \dots, a_n)$  as the square of the Euclidean norm of  $\underline{e}(\underline{r})$  integrated over the region of the solution. Thus



$$\begin{aligned} \epsilon(\underline{r}; a_1, a_2, \dots, a_n) = & \iint w(\underline{r}) \left\{ \left[ \sum_{j=1}^{M/2} a_j L\phi_j(\underline{r}) - S_Y(\underline{r}) \right]^2 \right. \\ & \left. + \left[ \sum_{j=\frac{M}{2}+1}^M a_j L\phi_j(\underline{r}) - S_Z(\underline{r}) \right]^2 \right\} dV \end{aligned}$$

where  $w(\underline{r})$  is a weighting function. The least-squares matrix is determined by minimizing the mean-square error with respect to the  $a_j$ .

$$\begin{aligned} \frac{\partial}{\partial a_k} \epsilon(\underline{r}; a_1, a_2, \dots, a_n) = 0 = & \iint w(\underline{r}) \left\{ \left[ \sum_{j=1}^{M/2} a_j L\phi_j(\underline{r}) - S_Y(\underline{r}) \right] L\phi_k(\underline{r}) \right. \\ & \left. + \sum_{j=\frac{M}{2}+1}^M a_j L\phi_j(\underline{r}) - S_Z(\underline{r}) \right\} L\phi_k(\underline{r}) dV \end{aligned} \quad \text{Eq. D3}$$

Forming Equation D3 for  $k=1, 2, \dots, M$  generates a linear system of equations from which the  $a_j$  are determined simultaneously.